國立臺灣大學理學院地質科學系

碩士論文

Department of Geosciences
College of Science
National Taiwan University

Master Thesis

南大洋太平洋區域於晚中新世的古生產力變化

Paleo-productivity variations during the late Miocene in the Pacific sector of Southern Ocean

温婉彤
Yuen Tung Kiki Wan

指導教授：羅立 博士、林卉婷 博士
Advisor: Li Lo, Ph.D., Huei-Ting Lin, Ph.D.

中華民國 112 年 7 月

July 2023

doi:10.6342/NTU202301546

國立臺灣大學碩士學位論文
口試委員會審定書
MASTER'S THESIS ACCEPTANCE CERTIFICATE
NATIONAL TAIWAN UNIVERSITY

南大洋太平洋區域於晚中新世的古生產力變化

Paleo-productivity variations during the late Miocene in the Pacific sector of Southern Ocean

本論文係温婉彤（R10224216）在國立臺灣大學地質科學學系暨研究所完成之碩士學位論文，於民國 112 年 7 月 4 日承下列考試委員審查通過及口試及格，特此證明。

The undersigned, appointed by the Department of Geosciences, National Taiwan University on 4th July, 2023 have examined a Master's thesis entitled above presented by Wan Yuen Tung kiki (R10224216) candidate and hereby certify that it is worthy of acceptance.

口試委員 Oral examination committee：

（指導教授 Advisor）　（指導教授 Advisor）

致謝

經過兩年的時間，終於完成了碩士論文，達到了人生的最中一個很重要的里程碑。在碩班生涯的兩年中，得到了很多人的幫助，我想在這裡一一表達我的感謝。首先要感謝的，是我的指導教授羅立教授及林卉婷教授。兩位教授對我的耐心指導及學術上的提攜就像陽光和水分，讓我從一顆種子茁壯成長，最終學有所成。雖然我現在還只是一棵幼苗，但日後我會繼續以自己的努力長成大樹，不會辜負老師的栽培。再次感謝兩位教授對我的信任，讓我有機會投入這次的研究。

另外，十分感謝張詠賦教授百忙之中抽空擔任本人的口試委員。張教授的細心指正及寶貴意見，讓我了解如何使論文更為完整，在此獻上我深深的感謝。此外，感謝臺大漁科所的楊姍樺教授及其實驗室人員借出分光光譜儀，讓我可以更有效率地對生物性蛋白石進行分析，對研究有極大幫助。另外也要感謝王興麟學姐，除了在元素分析儀上的協助，還十分感激學姐對我的信任，讓我有機會分析學姐研究中的樣品及進行討論，讓我獲益良多。感謝 IODP 383 航次的學者，提供岩芯材料；以及九州大學的岡崎裕典(Yusuke Okazaki)教授提供實驗協助。

接下來要感謝實驗室的學長姐、同學及學弟。首先是陳韋竹學姐，感謝學姐在研究上對我的協助，有了學姐的幫忙，才可以成功建立元素分析儀分析碳的方法。除了是學姐外，韋竹還是我的一個好夥伴，與我分享生活上的趣事，為苦悶的實驗中帶給我歡樂；另外，要感謝實驗室中的大學姐——吳依璇學姐。學姐為我提供了很多待人處事及職涯規劃上的建議，就像黑間中的一盞明燈，讓我找到方向；感謝實驗室助理鄭郁豫學姐和楊峻誌學長，為我提供了不少的協助;也想要感謝實驗室同學蔡易辰、楊翔宇和陳洪毅，謝謝大家給予我的支持和鼓勵，大家在研究中互相扶持，並且共同進步；最後感謝學弟李鍶政，在使用元素分析儀上的協助。非常感謝實驗室的大家，與我分享生活，為我帶來快樂。很高興在這兩年中，有大家的陪伴。

doi:10.6342/NTU202301546

我最想要感謝的，是我的家人和朋友。一開始我選擇來台灣唸書時，他們雖然感到十分不捨，但仍然支持我的決定。從小到大，父母都十分尊重我的所有決定，並會理性討論問題。甚至在升讀大學時，我毅然選擇了前往台灣就讀有興趣的地質系，而不是留在香港，雖然父母對此決定感到不解，但仍然對我找到自己的方向感到高興。家人和朋友們雖然擔心我離開熟悉的地方後會遇到難關，但他們都相信我可以成功跨過。今天，我想跟他們說，我成功克服困難，達到我的目標了。我也想要感謝我的妹妹，我很抱歉在她中學六年這重要的成長時期，都沒有在她身邊，但她依然為我達成目標感到高興，也願意視我為最信任的人，向我傾訴。我很開心成為了讓妹妹自豪的姊姊，成為了讓父母驕傲的女兒，成為了讓朋友引以為榮的對象。

最後，我想要感謝我的大學的組員林子游。他在我迷惘的時候給我意見，在我信心低落時給我鼓勵，在我情緒崩潰時給我擁抱。謝謝四年半以來，一直在我的身邊支持我。從大學的時候開始，明明知道我頭腦不好，上課還是願意跟我一組，讓我抱大腿。就算我沒幫上什麼忙，在野外也走得慢，也沒有嫌棄我。在生活上，也照顧了我非常多，如果沒有他的話，大概一早就被壓力擊倒，根本無法堅持完成研究。十分感激組員帶給我快樂，希望組員也能乘風破浪，達到自己的目標！

最後的最後，我想感謝一切給予我支持及鼓勵的人，沒有你們的話，我是沒有辦法達成目標的，謝謝你們！

doi:10.6342/NTU202301546

中文摘要

海洋沉積物中的碳酸鈣及生物性蛋白石的質量累積速率（mass accumulation rate, MAR），可以反映受氣候及洋流影響而變化的鈣質和矽質生物的生產力，以及海洋的保存能力。以往的研究發現，於晚中新世期間發生了強烈的氣候及環境變化。例如，於 7.6–6.7 Ma 的晚中新世碳同位素變化 （Late Miocene Carbon Isotope Shift, LMCIS)中，全球的底棲及浮游有孔蟲碳同位素有−1‰的變化。大約在同一時期，發生了晚中新世冷卻事件（Late Miocene Cooling, LMC）。大約於 7 至 5.4 Ma，全球各地的海表面溫度都下降至接近現今的值。在晚中新世期間，陸地大小的冰帽只存在於南極洲，因此南極冰蓋強迫可能是造成於晚中新世的全球氣候劇烈變化的原因。南極環流（Antarctic Circumpolar Current, ACC)主導了南大洋的海表至深水，並對大氣環流作出響應，在全球的氣候和碳循環中有重要作用。然而，只有少數研究中探討 ACC 的太平洋區域，限制了我們對這個世界上最大的洋流系統的碳酸鹽和生物源蛋白石埋藏歷史的了解。我們的研究利用南大洋的太平洋區域中部和東部的碳酸鈣及生物性蛋白石埋藏，重建晚中新世的生產力。研究的樣本是來自綜合大洋鑽探計劃 383 航次於南大洋太平洋區域的 U1541 及 U1543 站點的岩芯。

結果顯示，在 8.3 至 6.0 Ma 期間，U1541 站點採集的碳酸鈣及生物性蛋白石量幾乎呈相反趨勢。整體而言，U1541 於 LMCIS 開始後，碳酸鈣減少，蛋白石增加。於 6.0 至 5.5 Ma 期間，兩者都處於相對低值；而 U1543 站點則由蛋白石主導，碳酸鈣的埋藏量顯著地低。比較兩個站點的數據，U1541 碳酸鈣 MAR 比 U1543 顯著地高。

我們推測南大洋的太平洋區域由生產力主導。另外，兩個地點的生產力變化趨勢，可能受到 LMC 時海表面溫度冷卻所影響，指示 ACC 的擴張，並影響湧升流的強度。ACC 的擴張最後導致了 ACC 流速的減慢，以及 6.0 百萬年之後 U1541 的低生產量。兩個站點的表水營養受到不同的湧升流強度和地理條件所影響，導致兩個站點的生產力的差異。最後，ACC 的太平洋區域的生產力與大西洋區域的趨勢相似，可能表示南大洋的生產力是由 ACC 控制。這些數據也表明結合晚中新世的陸地過程，全球高海洋生產力可能最終導致 LMCIS。

關鍵詞：晚中新世、南大洋、生產力、碳酸鈣、生物性蛋白石

doi:10.6342/NTU202301546

Abstract

Mass accumulation rate (MAR) of calcium carbonate ($CaCO_3$) and biogenic opal in marine sediment reflect the variations in calcareous and siliceous productivity, and preservation of the ocean, influenced by climate and ocean circulations. During the late Miocene, Late Miocene carbon isotope shift (LMCIS), a long-term negative 1‰ shift globally, occurred between 7.6 and 6.7 million years ago (Ma). About the same period, late Miocene cooling (LMC) happened around 7 to 5.4 Ma, which culminated with ocean temperatures dipping to near-modern values. The Antarctic ice sheet forcing might be responsible for drastic changes globally during the late Miocene, as continental-sized ice sheets only exist in Antarctica during this period of time. The Southern Ocean, where the Antarctic Circumpolar Current (ACC) dominates the surface-deep water, and responds to atmospheric circulations, plays an important role in the global climate and carbon cycle. However, only a few investigations look into the Pacific sector of the ACC, limiting our understanding of the productivity histories of this world's largest zonal current system. Our study reconstructs the biogenic productivity using the sedimentary carbonate and biogenic opal content in the central and eastern Pacific sector of Southern Ocean. Major samples are from sites U1541 and U1543 obtained during the International Ocean Discovery Program (IODP) Expedition 383.

Our results show that at site U1541 (central Pacific sector of the ACC), $CaCO_3$ and opal fluxes sustain a negative relationship between 8.3 to 6.0 Ma. Overall, the $CaCO_3$ flux decreases while the opal increases during the onset of LMCIS. Both $CaCO_3$ and opal fluxes remain low during 6.0 to 5.5 Ma. At site U1543 (east Pacific sector of the ACC), opal burial dominates, while $CaCO_3$ flux is significantly low throughout the period.

doi:10.6342/NTU202301546

Comparing the data in the two sites, site U1541 has a significantly higher $CaCO_3$ flux and relatively lower opal flux than U1543.

We speculate that the Pacific sector of Southern Ocean is productivity-dominated. Overall, the increasing opal in both sites might be the consequence of sea surface temperature cooling during the LMC, and indicate the ACC expansion, which affects the strength of upwelling. This eventually leads to the slowing of ACC and the low burial fluxes at site U1541 after 6.0 Ma. The regional productivity differences between the two sites may be due to the different nutrient availability caused by upwelling strength and spatial differences. On the other hand, the productivity changes in the Pacific sector of the ACC coincides with the Atlantic sector, which may indicate that the Southern Ocean productivity is mainly controlled by the ACC. This also indicates that LMCIS may be related to the high global primary productivity, with the influence of the terrestrial processes.

Key words: late Miocene, Southern Ocean, productivity, carbonate, biogenic opal

doi:10.6342/NTU202301546

Contents

doi:10.6342/NTU202301546

doi:10.6342/NTU202301546

Figures

doi:10.6342/NTU202301546

doi:10.6342/NTU202301546

Tables

doi:10.6342/NTU202301546

1 Introduction

1.1 Ocean productivity

Productivity refers to the quantity of organic material produced by organisms per unit of time (Hanson, 1962). It mainly refers to the production by phytoplankton, the plants suspended in the ocean. Ocean productivity includes two divisions, which are primary and secondary productivities. Primary productivity refers to the rate of organic carbon produced by primary producers (known as autotrophs), while secondary productivity refers to the growth rate of heterotrophic biomass (Sigman and Hain, 2012). The majority of ocean productivity is constituted by calcareous and siliceous production (Yao, 2022) which play different roles in biological pump (Ramaswamy and Gaye, 2006).

The processes of carbon fixation and atmospheric CO_2 export is defined as "biological pump" (Volk and Hoffert, 1985). Atmospheric CO_2 (one of the inorganic carbon, IC) is fixed and transferred into organic carbon (OC) by photosynthesis of primary producers, and exported to deeper waters when these organisms sink to the water bottom (Ramaswamy and Gaye, 2006). Once CO_2 is brought to the bottom, the partial CO_2 in surface waters is lowered and eventually reduces the atmospheric CO_2 (De La Rocha and Passow, 2014). Siliceous production is dominated by Diatoms, which are

doi:10.6342/NTU202301546

photosynthetic species (Kuczyńska et al., 2015), thus siliceous productivities are mainly primary producers and can lead to the reduction of atmospheric CO_2 (Ramaswamy and Gaye, 2006). Although calcareous plants also carry out photosynthesis, their calcification can eventually lead to an increase in atmospheric CO_2. The amount of photosynthesis and respiration do not affect the alkalinity of the seawater, thus the equilibrium between surface water and air can remain unchanged and CO_2 is not released into the atmosphere (Kalokora et al., 2020). However, calcification which calcareous organisms uptake CO_2 to build $CaCO_3$, decreases the alkalinity of the surface water, as 1 mol of $CaCO_3$ leads to a decrease in two equivalents of the total alkalinity (Chisholm and Gattuso, 1991). Water, where calcification has occurred, will equilibrate with air by releasing CO_2 to the atmosphere, thus, higher calcification by increasing calcareous production eventually leads to an increase in atmospheric CO_2 (Ware et al., 1992). Therefore, calcareous producers both uptake and release CO_2, while increasing siliceous productivity can result in lower atmospheric CO_2 (Ramaswamy and Gaye, 2006) (Fig. 1.1).

Ocean productivity plays an important role in controlling the carbon input and output of the ocean, thus, has further influences on climate change as the efficiency of biological pump affects the concentration of the greenhouse gas CO_2 (De La Rocha and Passow, 2014). Increasing atmospheric CO_2 strengthens the greenhouse effect, and leads to global

doi:10.6342/NTU202301546

warming, and vice versa (Kump et al., 2000). Therefore, ocean productivity can respond to global climate signals (Paytan, 2009).

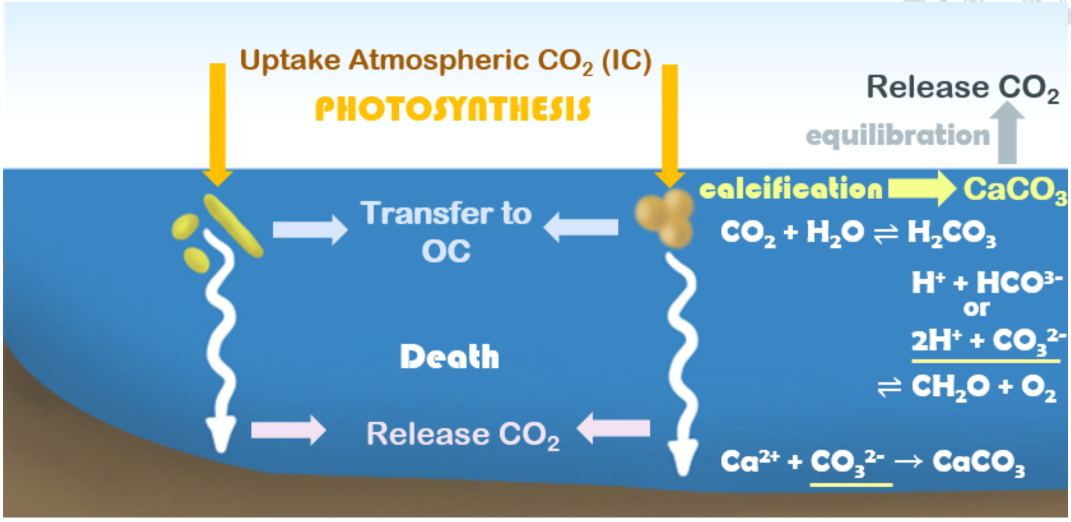

Fig 1.1 Schematic illustration of the biological pump processes.

1.2 Productivity proxies

Siliceous organisms such as diatoms, radiolarians, and sponges, utilize silica (SiO_2) for growth and forming their hard parts. After the death of these organisms, their skeletal material, biogenic opal will be deposited (Demaster, 1981). On the other hand, calcification by calcareous organisms form calcium carbonate ($CaCO_3$), thus, the hard parts of these organisms consist of $CaCO_3$ (Frankignoulle et al., 1995; Ramaswamy and Gaye, 2006). In short, calcium carbonate ($CaCO_3$) and biogenic opal in sediment are composed of the skeletal materials of calcareous and siliceous organisms, respectively (Paytan, 2009).

doi:10.6342/NTU202301546

The presence of calcareous and siliceous organisms varies in different regions of ocean, due to different nutrient availability. Most plankton require "nutrients" (nitrogen (N), phosphorus (P), iron (Fe), and silicon (Si)) for growth (Ramaswamy and Gaye, 2006). Besides, CO_2 concentration is important for primary producers, as higher CO_2 concentrations can evoke photosynthesis by the organisms (Hutchins & Fu, 2017). Some plankton (mainly calcareous) also need calcium (Ca) for building hard parts. CO_2 and Ca are not considered as limiting nutrients as they are relatively stable and abundant in seawater (Sigman and Hain, 2012). Generally, siliceous organisms are abundant in nutrient-rich environments, while calcareous organisms are adapted to nutrient-depleted surface water (Iglesias-Rodríguez, 2002). Siliceous organisms need Si for constructing their opal skeletal materials, thus Si is significantly important for siliceous productivity (Sigman and Hain, 2012). Nutrient-rich surface waters favor the growth of siliceous organisms (mainly diatoms) (Ramaswamy and Gaye, 2006), as Si can be mostly found in waters where N and P are abundant on the surface ocean (Sigman and Hain, 2012). In modern oceans, high opal burials are mainly found in the Pacific and Southern Oceans, while low in Atlantic Ocean (Cortese et al., 2004).

Previous studies suggest that wind-driven upwelling brings high CO_2 and nutrient waters from deep ocean to the surface (e.g., Martinez-Garcia et al., 2011, Kohfeld et al.,

doi:10.6342/NTU202301546

2005). Besides upwelling, cold surface water can also bring more nutrient-rich water from deep to the surface water. Warm surface water with low density leads to strong stratification which inhibits vertical mixing and nutrient exchanges with dense cold deep water (Li et al., 2020). Cold surface water weakens the vertical density gradient, and favors the mixing of waters (destratification), thus allowing nutrients to be brought to the sea surface (Sigman and Hain, 2012). In addition, terrestrial processes such as weathering and volcanic activities can also increase siliceous productivity, as they bring iron and silicate-rich dust to the ocean (Martin et al., 1989; Van cappellen et al., 2002). Conclusively, higher biogenic opal deposition is usually found in stronger upwelling areas and low sea surface temperature regions. Nutrients from land also result in an increase of opal fluxes.

Calcareous productivity is generally higher in nutrient-depleted surface water, as calcareous productivity may be outcompeted by siliceous productions (Iglesias-Rodríguez, 2002). However, calcareous plants are also abundant under surface water which is rich in CO_2 and dissolved P (mostly phosphate) (Wei et al., 2021). When Si is insufficient in water, diatoms may be unable to compete with other plankton, including calcareous organisms (Bradtmiller et al., 2007). Therefore, when strong upwelling brings high CO_2 and nutrient waters to the surface, calcareous production can also increase

doi:10.6342/NTU202301546

depending on the water chemistry in different regions (Wei et al., 2021). We can correlate the siliceous and calcareous productivity with the climate and ocean environment through the reconstruction of $CaCO_3$ and opal burial fluxes.

Besides, as OC is formed when primary producers carry out photosynthesis, it can represent the most direct proxy for primary productivity, and many studies have reconstructed primary productivity by using total organic carbon (TOC) (Schoepfer et al., 2015). Although the TOC deposition is strongly dependent on water depths, so only little OC can be preserved in the sediment (Paytan, 2009), we can determine the major producer of the plankton community through correlations with TOC. Positive correlations between TOC and $CaCO_3$/opal fluxes can indicate the majority of primary productivity, as this can show which production has higher contributions to photosynthesis (Lyle et al., 1988). This means we can understand how siliceous and calcareous productions affect the climate base on the correlation between TOC and $CaCO_3$/opal fluxes. Therefore, in this study, we determined the marine $CaCO_3$, opal, and TOC contents, in order to have further investigation into the relationship between climate and ocean productivity.

doi:10.6342/NTU202301546

2 Background

2.1 Late Miocene

During the late Miocene (~12-5 Ma), there were drastic climatic and palaeoceanographic changes in a warmer-than-modern world. Besides drying and vegetation changes (Herbert et al., 2016), a sustained global cooling trend occurred during this period of time (Holbourn et al., 2018), despite the warmer climate. Global sea surface temperature has a decreasing trend during ~7.0 to 5.4 Ma, which is defined as the Late Miocene Cooling (LMC) event (Fig 2.1b, Herbert et al., 2016). The main driving mechanism of LMC is most like the decline in atmospheric CO_2 and the increasing sea surface temperature gradient between the equator and the poles (Herbert et al., 2016, Martinot et al., 2022).

About the same period, the global benthic and planktonic $\delta^{13}C$ has a negative ~1‰ shift during ~7.6 to 6.7 Ma, known as the Late Miocene Carbon Isotope Shift (LMCIS) (Fig. 2.1a, e.g., Keigwin, 1979, Holbourn et al., 2018). The major mechanisms driving the LMCIS are still controversial, as both planktonic and benthic foraminiferal $\delta^{13}C$ decline during this period of time (Drury et al., 2018, Holbourn et al., 2018, Westerhold et al., 2020). Most studies suggest that elevated primary production is the main mechanism that leads to LMCIS (e.g. Diester-Haass et al., 2005), as ^{12}C is utilized first

doi:10.6342/NTU202301546

during photosynthesis, more negative $\delta^{13}C$ will be more brought to the bottom (Du et al., 2022). However, this cannot explain the same decreasing trend of planktonic $\delta^{13}C$. Another hypothesis is the C_4 plant expansion (Bickert et al., 2004). There is a wide-spreading transition of C_4 grassland from predominated C_3 plant during the late Miocene (e.g., Cerling et al., 1997, Quade et al., 1989). The photosynthesis by the C_4 plant has less preference for ^{12}C than the C_3 plant, thus causing less negative $\delta^{13}C$ in terrigenous organic matter (Quade et al., 1989). As more ^{13}C is utilized by the terrigenous biomass, more ^{12}C is left in the atmosphere and input into the ocean, which causes a decline in marine $\delta^{13}C$ (Du et al., 2022). However, as the C3:C4 shift is not globally synchronous, it may not be the main driving mechanism of LMCIS, a global event (Drury et al., 2018). The uplift of the Tibetan Plateau at ~8.0 Ma is also a hypothesis of driving LMCIS (Li et al., 2014). Intensive uplifting can lead to more negative $\delta^{13}C$ input into the ocean through strong weathering of buried organic matter (Wang et al., 2021). Nevertheless, this uplift event is regional, and may be difficult to drive this global event (Herbert et al., 2016).

On the other hand, the climate conditions in the late Miocene are similar to the modern in spite of the warmer climate. Proxy records show that atmospheric pCO_2 in the late Miocene was near or not much higher than the modern (Steinthorsdottir et al., 2021). In addition, both the late Miocene and modern climate are significantly influenced by the

doi:10.6342/NTU202301546

Antarctic ice sheet (Anderson et al., 2011), with relatively weak Northern Hemisphere ice sheet forcing, especially when the Antarctic ice sheet formed the main component of the cryosphere during the middle and late Miocene (Gasson et al., 2016). Therefore, the Antarctic ice sheet might be responsible for the drastic changes during the late Miocene.

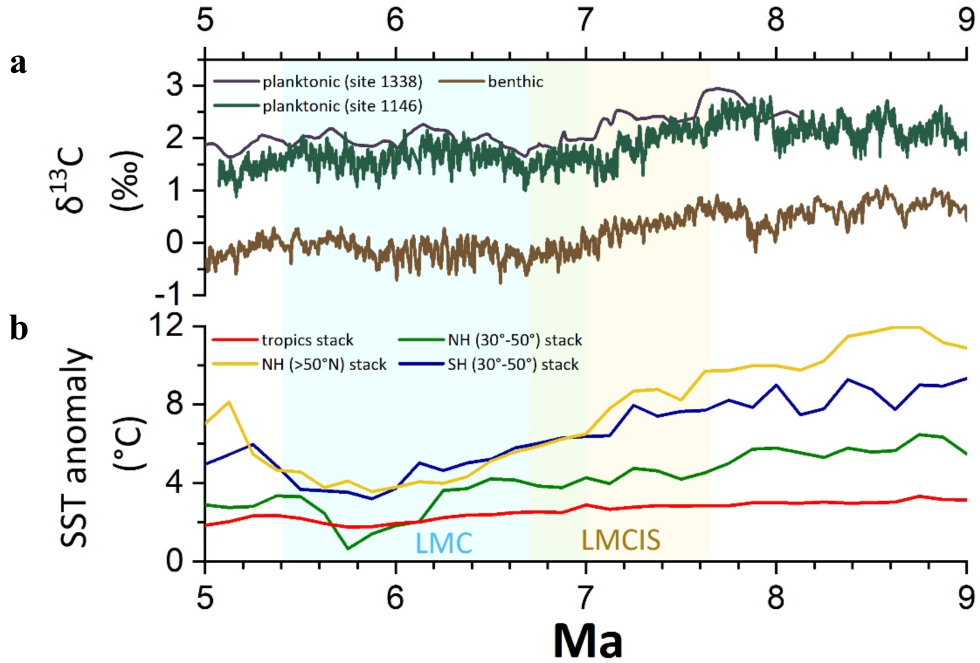

Fig. 2.1 Late Miocene climate background. **a** planktonic foraminiferal $\delta^{13}C$ record at site U1338 (Drury et al., 2018) and site 1146 (Holbourn et al., 2018); benthic foraminiferal $\delta^{13}C$ record (Westerhold et al., 2020) **b** global sea surface temperature anomaly (Herbert et al., 2016). Blue and yellow vertical bar are the LMC and LMCIS events, respectively.

doi:10.6342/NTU202301546

2.2 Southern Ocean

During the late Miocene, there is continental-sized ice sheets only in Antarctica, but not in the Northern Hemisphere (Steinthorsdottir et al., 2021). This makes Antarctica has more influence on global climate than the Arctic during this period of time. Planetary albedo is one of the climate forcing controls, which is the degree of how much sunlight is reflected back into space, thus playing an important role in global warming (Thomas Farmer and Cook, 2012). As ice cover can reflect more solar radiation, it has more effects on the global climate (Budyko, 1969). Large Antarctica ice sheet, therefore, has significant influences on climate change, which is also affected by CO_2 concentration (Singh and Polvani, 2020). Antarctica is able to maintain its enormous ice sheet due to the major circulation system of Southern Ocean, the Antarctic Circumpolar Current (ACC), which keeps warm subtropical water away from the Antarctic continent (Barker et al., 2007). Some studies also state that the Antarctic ice sheet expansion may lead to the ACC expansion during atmospheric CO_2 decline, thus there is a strong coupling between Antarctic ice and Southern Ocean (Leutert et al., 2020). The ACC is formed with the openings of the Tasmanian Seaway and the Drake Passage during the Paleogene (e.g., Barker and Thomas, 2004), resulting in the isolation of Antarctica. The ACC flows from west to east, mainly driving by the westerly wind (Hassold et al., 2009). It is the only current that connects all three major basins of the global ocean (Pacific, Atlantic, and

doi:10.6342/NTU202301546

Indian Oceans), which flows from the sea surface to the bottom (Barker and Thomas, 2004). Therefore, it plays an important role in the mixing and redistribution of water, heat, and nutrient with other oceans (Hassold et al., 2009).

Biological utilization of nutrients in the Southern Ocean regulates the preformed nutrient reservoir for a great majority of the deep ocean, therefore it plays an important role in atmospheric CO_2 concentration variation and regulating the global average efficiency of the biological pump (Sigman et al., 2010). Some studies suggest that the siliceous productivity is limited in parts of Southern Ocean because of the lack of iron dust input (de Baar et al., 1995), while some researchers state that the productivity in some parts of Southern Ocean does not respond positively to iron dust (Chase et al., 2003). Therefore, there may be other factors that affect the siliceous productivity in Southern Ocean, and may further influence the nutrient transportation to other oceans through the ACC. As Southern Ocean productivity controls nutrient transfer to other oceans (Hassold et al., 2009), it can affect the efficiency of biological pump and atmospheric CO_2 concentration in these oceans and eventually leads to global climate changes (Sigman et al., 2010). Therefore, productivity in Southern Ocean is important for us to investigate as it may have large influences on global climate changes during the late Miocene. Productivity records in Southern Ocean can help to explain how atmospheric CO_2 and

doi:10.6342/NTU202301546

nutrient have further effects on the climate, and investigate the relationship between productivity and the problematic climate event during the late Miocene.

2.3 The aim of this study

Late Miocene stands out as the most prolonged shift during the Neogene, with problematic climate events (Holbourn et al., 2018). The Antarctic ice sheet forcing may be responsible for these dramatic changes during the late Miocene, which is controlled by the major current system of Southern Ocean, the ACC (Barker et al., 2007). This indicates that reconstruction of Southern Ocean productivity is important for investigating the driving mechanisms of climate change. Our previous understandings of paleoceanography and ocean productivity are mostly from the Deep Sea Drilling Project (DSDP), Ocean Drilling Program (ODP), and Integrated Ocean Discovery Program (IODP). For example, ODP Leg 177 and IODP Leg 318 recovered Cenozoic sediments in the Atlantic and Indian sectors of the ACC, respectively (Lamy et al., 2021). However, there was much less investigation into the Pacific sector of the ACC. The preexisting programs mainly drill in the Antarctic continental margin south of the ACC, such as ODP Leg 178. Therefore, IODP Expedition 383 was designed for more advanced knowledge of the dynamics of the ACC (Lamy et al., 2021).

doi:10.6342/NTU202301546

The productivity in the Southern Ocean may affect the production rates in other oceans through regulating the nutrient distribution, and also have influences on global climate by the efficiency of the biological pump (Sigman et al., 2010). However, the factor that affects the productivity in Southern Ocean is complex (Chase et al., 2003), which may further influence the global production rates, and thus the atmospheric CO_2 (Sigman et al., 2010). Variations in CO_2 seems to be the main driving mechanism of climate change (Herbert et al., 2016), the productivity in the Southern Ocean, therefore, is important for the investigation of climate changes during the late Miocene. Our study reconstructs the biogenic productivity using the sedimentary $CaCO_3$, and biogenic opal content in the central and eastern Pacific sector of Southern Ocean, as these components constitute the majority of the ocean productivity (Yao, 2022). TOC content is also determined, which is important in indicating the roles of siliceous and calcareous organisms during the period of time in different regions (Lyle et al., 1988). Therefore, this study allows us to understand the paleoenvironment of Southern Ocean and also investigate the relationship between ocean productivity and the climate events during the late Miocene, through reconstruction of the calcareous and siliceous production.

doi:10.6342/NTU202301546

3 Material and Methods

3.1 IODP Sites U1541 & U1543

The materials used in this research are Sites U1541 and U1543 sediment archives, which are from the International Ocean Discovery Program (IODP) Dynamics of the Pacific Antarctic Circumpolar Current (DYNAPACC; Expedition 383). Both sites are located in the Pacific sector of the ACC.

3.1.1 Site U1541

Site U1541 is in the central Pacific sector of the ACC (54°12.76′S, 125°25.54′W, Fig. 3.1), at 3604 m water depth. It is located in the western flank of the southernmost east Pacific rise and is underlain by oceanic crust formed at ~8-6 Ma (Eagles, 2006).

Three holes were drilled at Site U1541, which are holes A, B, and C. The IODP exp. 383 scientists have constructed a splice from 0 to 127.3 m composite depth below seafloor (CCSF) using these three holes. As hole U1541B was drilled deeper, its cores were attached to the bottom of the splice (146.0 m CCSF). In this study, the U1541B and U1541C sediment archives from 106.0 m to 145.9 m CCSF are used. According to the age model from IODP, this section covers the past ~5.6 Myr to ~8.4 Myr.

doi:10.6342/NTU202301546

3.1.2 Site U1543

Site U1543 is in the east Pacific sector of the ACC (54°35.06′S, 76°40.59′W, Fig 3.1), at 3860 m water depth. It is located west of the Chile Trench and underlain by oceanic crust formed at ~20 Ma (Eagles, 2006). Site U1543 is also situated in the Cape Horn Current (CHC), which is a northern branch of the ACC before entering the Drake Passage (Well and Roether, 2003).

Two holes were drilled at Site U1543, which are holes A and B. The IODP exp. 383 scientists have constructed a splice from 0 to 376.3 m composite depth below seafloor (CCSF) using these two holes. In this study, the U1543A and U1543B sediment archives from 278.2 m to 354.4 m CCSF are used. According to the age model from IODP, this section covers the past ~5.2 Myr to ~7.3 Myr.

doi:10.6342/NTU202301546

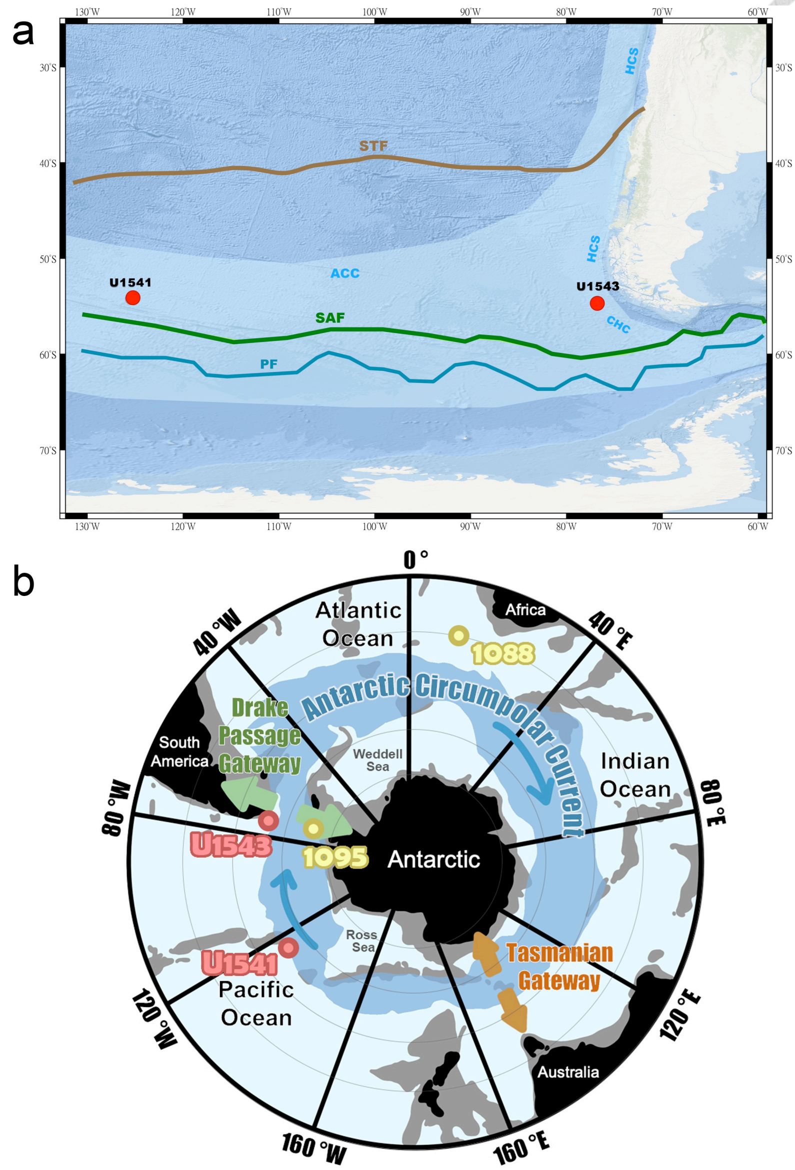

Fig. 3.1 The location of the sites in this study (red dots) and the sites are mentioned in section 5 (yellow dots) (modern location after Lamy et al., 2021; Behrens and Bostock, 2023; Hassold et al., 2009; Diester-Haass et al., 2005). **a** STF= Subtropical Front (brown line), SAF= Subantarctic Front (green line), PF= Polar Front (dark blue line); ACC= Antarctic Circumpolar Current, CHC= Cape Horn Current, HCS= Humboldt Current System (highlight in light blue). **b** The polar-centered perspective (modified from Hodel et al., 2021).

doi:10.6342/NTU202301546

3.2 Age model

The age models of Sites U1541 and U1543 were constructed by IODP exp. 383 scientists, based on biostratigraphic and paleomagnetic age markers (see Appendix Tables 1-4). The average linear sedimentation rate (LSR) at Site U1541 is 2.7 cm/kyr while at U1543 is 4.5 cm/kyr (Lamy et al., 2021). Fig. 3.2 shows the linear sedimentation rate of both sites.

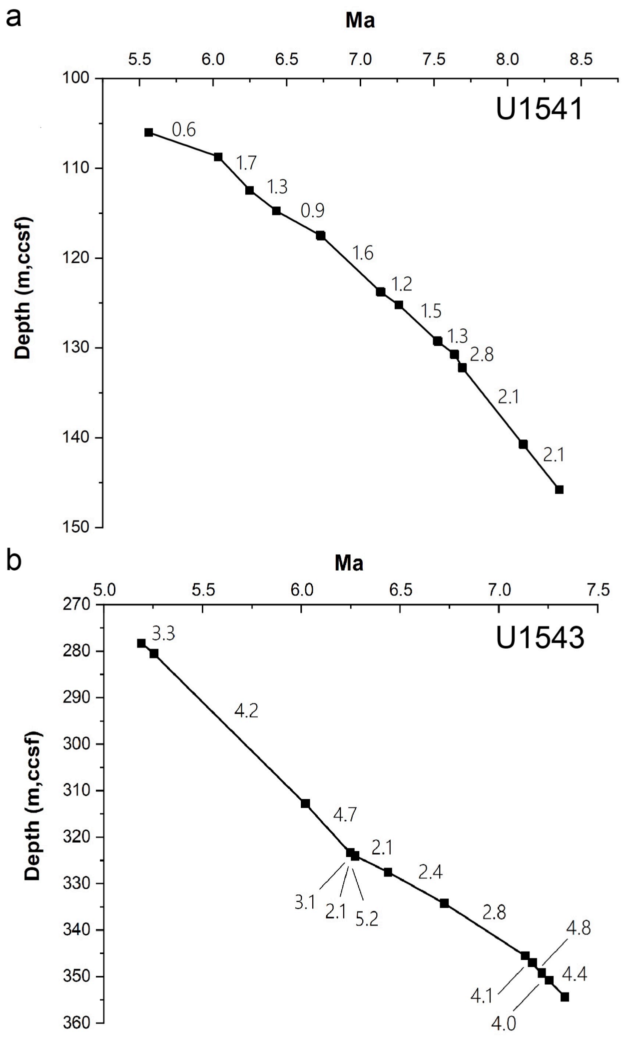

Fig. 3.2 The linear sedimentation rate (LSR) of the sites. **a** Site U1541 **b** Site U1543. ccsf= core composite depth below seafloor. The numbers are the LSR (cm kyr^{-1}).

doi:10.6342/NTU202301546

3.3 Methods

3.3.1 Calcium Carbonate and total organic carbon analysis

Elementar TOC analyzer soli TOC® cube (EA) (Fig. 3.3) is used to determine carbon content in the sediments. It offers the options of measuring labile organic carbon (LOC), residual/refractory organic carbon (ROC), and total inorganic carbon (TIC).

3.3.1.1 Preparation and analysis

About 50 mg of freeze-dried and ground sediments are weighed into each crucible and placed into the analyzer. Each set of samples includes a standard sample and 5 to 6 sediment samples. The standard sample of the first set will be commercial soil standard (Leco soil standard), while the others will be in-house standard (DGS OC #1, acidified ground mudstone from Gutingkeng Formation, southwestern Taiwan) (see Appendix Tables 5 and 6). The first and last two positions are emptied, which are for warming up and stabilizing the detector. An empty crucible will be placed before and after a set of sediment samples for calculating the system blank. The maximum sample number (position) for each analysis is 89. Each measurement takes about 30 minutes for analyzing. According to the sequence above, 60-63 sediment samples can be analyzed in each analysis for about 45 hours.

doi:10.6342/NTU202301546

3.3.1.2 Quantification

The EA quantifies carbon and nitrogen contents in the sediment by combusting the sediment with oxygen. Carbon dioxide is formed through this process. These gases are detected by the infrared detector. The EA is capable of distinguishing different forms of carbon by temperature programming as organic carbon (OC) and inorganic carbon (IC) will be ashed under different temperatures. The temperature program “DIN19539_4” is used. There are 3 stages in this program, which combusts TOC, ROC, and TIC, respectively. Their temperature and holding time are C1: 550°C 400s, C2: 600°C 120s and C3: 900°C 150s. TOC will be ashed in C1 and C2. Most of the OC will be ashed in C1, so it needs a longer holding time for reaction. The residual OC will be ashed in C2. In order to avoid IC ashing in this stage, the holding time is shorter in C2. Finally, TIC will be ashed in C3. EA can separate the carbon signal of each stage, so we can have OC, ROC, and TIC data for each sample.

3.3.1.3 Calculation

The gas detection signal will be presented in area by integral. TC content of each sample is calculated by the following equation of the calibration curve (Fig. 3.4):

$$\text{TC (mg)} = (b) \times \text{TC area} + (a)$$

*(b) is the slope, while (a) is the constant term.

doi:10.6342/NTU202301546

TC (%) is calculated using the following equation:

$$\text{TC (\%)} = \frac{\text{TC (mg)}}{\text{weight (mg)}} \times 100\%$$

The error propagation of TC (%) (error (%)) is calculated using the following equation:

$$\text{error (\%)} = \text{TC (\%)} \times \sqrt{\left(\frac{0.2}{\text{weight (mg)}}\right)^2 + \left(\frac{SD_{cali}}{\text{TC (mg)}}\right)^2}$$

*0.2 (mg) is the potential error of the balance, while SD_{cali} is the standard deviation of the calibration curve.

TOC (%) and TIC (%) are calculated using the following equation:

$$\text{TOC (\%)} = \text{TC (\%)} \times \frac{(\text{LOC area} + \text{ROC area})}{\text{TC area}}$$

$$\text{TIC (\%)} = \text{TC (\%)} \times \frac{\text{TIC area}}{\text{TC area}}$$

$CaCO_3$ (%) is calculated using the following equation:

$$CaCO_3\ (\%) = \frac{\text{TIC (\%)} \times 100.0869}{12.11}$$

*The atomic mass of Carbon is 12. 11 g/mol, while the atomic mass of $CaCO_3$ is 100.0869 g/mol.

doi:10.6342/NTU202301546

Fig. 3.3 Elementar TOC analyzer soli TOC® cube (EA).

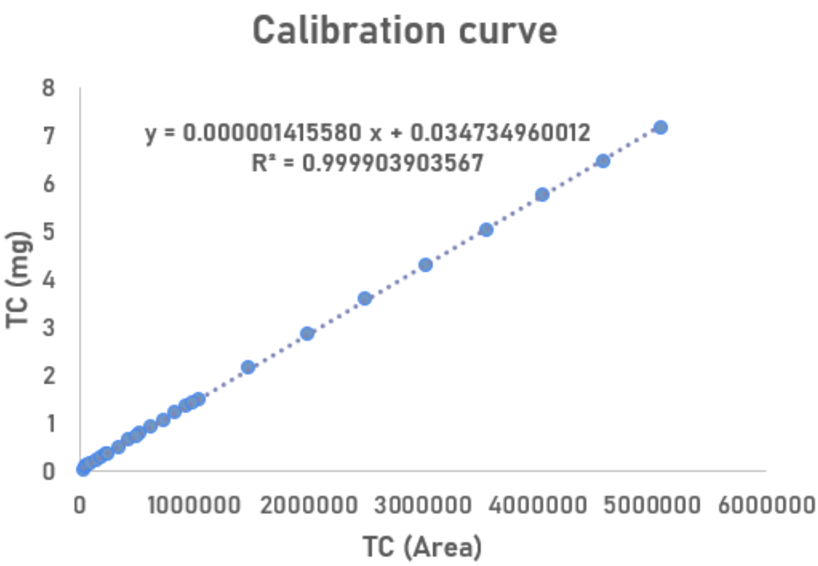

Fig. 3.4 The calibration curve calculating TC content.

doi:10.6342/NTU202301546

3.3.2 Biogenic opal determination

The biogenic silica extraction method generally follows Mortlock and Froelich (1989) with some differences. 2 M NaOH is used to extract opal from the sediments instead of using 2 M Na_2CO_3.

3.3.2.1 Preparation

50 mg of freeze-dried and ground sediments are weighed into 15 ml polypropylene centrifuge tubes. 5 mL of 10 % H_2O_2 is added into each tube, mixed well, and stood for 30 minutes. Then, add 5 mL of 1 N HCl into each tube and mix well. After 30 minutes, fill the tubes with deionized water to dilute the solutions. Centrifuge the tubes at 4300 rpm for about 5-10 minutes. Decant the supernatant and repeat diluting the samples for about 3 times until they have a pH of 5 or above. The tubes are then placed in an oven which is reheated to 50°C, and dried overnight.

3.3.2.2 Extraction

Add 10 mL of 2 M NaOH solution to the tubes. The tubes are then capped, mixed well, and sonified. Place the tubes in a constant-temperature water bath (YSC BT-150D) which is preheated to 85°C. At about 2 h and 4 h, remove the tubes and shake forcefully,

doi:10.6342/NTU202301546

then return to the water bath as soon as possible. After a total of 5 hours, centrifuge the tubes for 5 minutes at 4200 rpm. For each sample, 0.05 mL of supernatant is transferred to a polyethylene scintillation vial which is filled with 12 mL of deionized water, in order to dilute the extractant for analysis. The extraction solutions are then capped, mixed well, and stored for further analysis.

3.3.2.3 Analysis

Molybdate-yellow spectrophotometry is used to measure the Silicon content in the samples. For each sample, add 0.2 mL of the extraction solution into a cell of 96 well plate. 0.025 mL of Molybdate-sulfuric acid is added to each cell. Put the plate into Molecular Devices SpectraMax® ABS plus spectrophotometer (Fig. 3.5) to analyze the absorbance of the samples with a wavelength of 400 nm. All of the chemicals used for opal analysis are shown in Appendix Tables 8 and 9.

3.3.2.4 Calculation

Si content of each sample is calculated using the following equation of the calibration curve (Fig. 3.6):

$$Si_{diextract}\ (\mu M) = (b) \times A$$

doi:10.6342/NTU202301546

Where A is the absorbance and $Si_{diextract}$ is the Si concentration (μM) of the extraction solution.

Si (%) is calculated using the following equation:

$$Si\ (\%) = \frac{(Si_{diextract}\ (\mu M) \times F \times 0.01\ L \times 28\ g\ mol^{-1}) \times 0.001}{weight\ (mg)} \times 100\ (\%)$$

Where F is the dilution factor. The extractant was diluted for analyzing, so here I calculate the original concentration of the extractant; and 28 g mol^{-1} is the atomic mass of silicon.

Opal (%) is calculated using the following equation (Mortlock & Froelich, 1989):

$$opal\ (\%) = Si\ (\%) \times 2.4$$

Both $CaCO_3$, TOC and opal burial fluxes are defined by MAR (mass accumulation rate) in this research. MAR is calculated using the following equation:

$$MAR\ (g\ cm^{-2}\ kyr^{-1}) = \frac{(\%)}{100} \times \rho(g\ cm^{-3}) \times LSR\ (cm\ kyr^{-1})$$

Where (%) are $CaCO_3$ (%), TOC (%) or opal (%), ρ is the bulk density and LSR is the linear sedimentation rate.

doi:10.6342/NTU202301546

Fig. 3.5 Molecular Devices SpectraMax® ABS plus spectrophotometer.

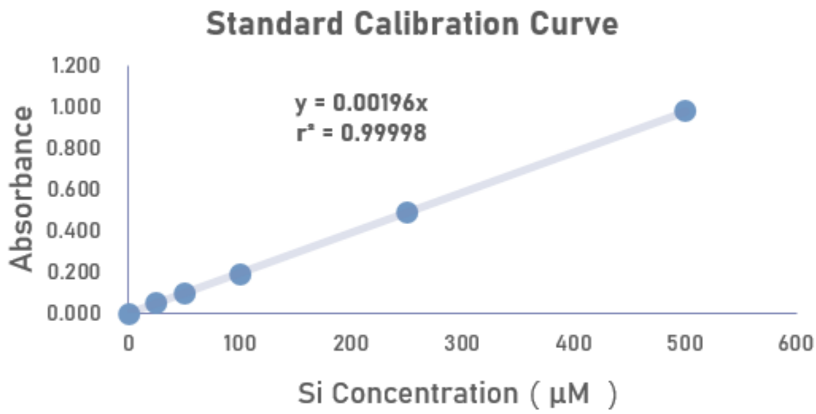

Fig. 3.6 The calibration curve calculating Si content.

doi:10.6342/NTU202301546

4 Results

In this study, we constructed the carbonate and biogenic opal burial fluxes in the Pacific sector of Southern Ocean during the late Miocene. At site U1541, 372 samples were determined, which cover 8.4 to 5.5 Ma. At site U1543, 97 samples were determined, which cover 7.5 to 5.1 Ma. All data are shown in Appendix Tables 10 and 11.

4.1 Site U1541

Fig. 4.1 shows the concentrations (weight percent) and fluxes (MAR) of $CaCO_3$, TOC, and opal at site U1541. Both $CaCO_3$ concentration and flux are high during 8.3 to 7.6 Ma. $CaCO_3$ concentration ranges from 67.85 to 95.95 %, while $CaCO_3$ flux has an increasing trend and ranges from 2.06 to 4.46 g cm^{-2} kyr^{-1}. In contrast, concentrations and fluxes of both TOC and opal are low during this period of time. TOC concentration ranges between 0.14 and 0.88 %, while TOC flux ranges between 4.81×10^{-3} and 0.03 g cm^{-2} kyr^{-1}. Opal concentration ranges between 0.04 and 6.68 %, while opal flux ranges between 1.38×10^{-3} and 0.23 g cm^{-2} kyr^{-1}.

During 7.6 to 7.1 Ma, both $CaCO_3$ concentration and flux have decreasing trends. $CaCO_3$ concentration decreases from 87.37 to 24.25 %, while $CaCO_3$ flux plunges sharply from 4.25 to 1.61 g cm^{-2} kyr^{-1} at 7.5 Ma, then drops to 0.49 g cm^{-2} kyr^{-1} at 7.1 Ma. At the

doi:10.6342/NTU202301546

same time, concentrations and fluxes of TOC and opal have increasing trends. TOC concentration and flux increase from 0.38 % and 0.01 g cm^{-2} kyr^{-1}, to 1.94 % and 0.04 g cm^{-2} kyr^{-1}, respectively. Opal concentration and flux rise from 2.68 % and 0.06 g cm^{-2} kyr^{-1}, to 28.70 % and 0.61 g cm^{-2} kyr^{-1}, respectively.

Between 7.1 and 5.5 Ma, concentrations of $CaCO_3$, TOC, and opal fluctuate and range from 13.53, 0.43 and 1.29 %, to 89.84, 2.04 and 24.97 %, respectively. On the other hand, during 7.1 to 6.0 Ma, fluxes of $CaCO_3$, TOC, and opal range from 0.31, 8.19×10^{-3} and 0.03, to 2.39, 0.05 and 0.58 g cm^{-2} kyr^{-1}, respectively. Both $CaCO_3$, TOC, and opal fluxes are low during 6.0 to 5.5 Ma. $CaCO_3$ flux ranges between 0.10 and 0.59 g cm^{-2} kyr^{-1}, TOC flux ranges between 7.18×10^{-3} and 0.01 g cm^{-2} kyr^{-1}, and opal flux ranges between 0.06 and 0.18 g cm^{-2} kyr^{-1}.

Overall, $CaCO_3$ flux has a decreasing trend over 8.3 to 5.5 Ma, while TOC and opal fluxes have increasing trends, except 6.0 to 5.5 Ma. $CaCO_3$ concentration sustains a negative relationship with TOC and opal concentrations during 8.3 to 5.5 Ma, while $CaCO_3$ flux has an inverse relationship with TOC and opal fluxes between 8.3 and 6.0 Ma (Fig. 4.3).

doi:10.6342/NTU202301546

4.2 Site U1543

Fig. 4.2 shows the concentrations (weight percent) and fluxes (MAR) of $CaCO_3$, TOC, and opal at site U1543. Both $CaCO_3$ concentration and flux remain at low levels over 7.3 to 5.2 Ma. $CaCO_3$ concentration ranges between 0.08 and 0.19 % during this period. Between 7.3 and 6.3 Ma, concentrations and fluxes of TOC and opal, and $CaCO_3$ flux, have decreasing trends. $CaCO_3$ flux ranges between 4.57×10^{-3} and 9.43×10^{-3} g cm^{-2} kyr^{-1}. TOC concentration and flux reach their peaks of 0.63 % and 0.04 g cm^{-2} kyr^{-1} at 7.2 Ma, then drop sharply to 0.13 % and 7.20×10^{-3} g cm^{-2} kyr^{-1}, respectively. From then until 6.3 Ma, both values remain low, with an average of 0.14 % and 6.41×10^{-3} g cm^{-2} kyr^{-1}. Opal concentration and flux exhibit similar patterns to TOC. Opal concentration and flux plunge from 28.92 % and 1.87 g cm^{-2} kyr^{-1}, to 8.19 % and 0.34 g cm^{-2} kyr^{-1}. Afterward, they continued at relatively low levels, averaging around 11.39 % and 0.46 g cm^{-2} kyr^{-1}, respectively.

During 6.3 to 5.2 Ma, concentrations and fluxes of TOC and opal, and $CaCO_3$ flux, are relatively higher. $CaCO_3$ flux fluctuates and ranges between 4.02×10^{-3} and 1.36×10^{-2} g cm^{-2} kyr^{-1}. While TOC concentration and flux range from 0.13 % and 5.25×10^{-3} g cm^{-2} kyr^{-1}, to 0.54 % and 0.04 g cm^{-2} kyr^{-1}, and reach their high points 0.54 % and 0.04 g cm^{-2} kyr^{-1}, respectively, at 6.0 Ma. Opal concentration and flux show general increasing

doi:10.6342/NTU202301546

trends during this period, which range from 3.37 % and 0.24 g cm^{-2} kyr^{-1}, to 23.80 % and 1.45 g cm^{-2} kyr^{-1}.

4.3 Comparison of site U1541 and U1543

Comparing the data of the two sites, $CaCO_3$ concentration and flux at U1541 (with an average of 67.58 % and 1.90 g cm^{-2} kyr^{-1}) are significantly higher than at U1543 (with an average of 0.14 % and 8.71×10^{-3} g cm^{-2} kyr^{-1}). Although TOC concentration at U1541 (with an average of 0.90 %) is higher than at U1543 (with an average of 0.21 %), TOC fluxes at the two sites are in similar ranges (from 4.81×10^{-3} to 0.05 g cm^{-2} kyr^{-1} and from 4.31×10^{-3} to 0.04 g cm^{-2} kyr^{-1}, respectively). In contrast, opal concentration and flux are higher at U1543 (with an average of 11.01% and 0.65 g cm^{-2} kyr^{-1}) than at U1541 (with an average of 7.45 % and 0.15 g cm^{-2} kyr^{-1}).

doi:10.6342/NTU202301546

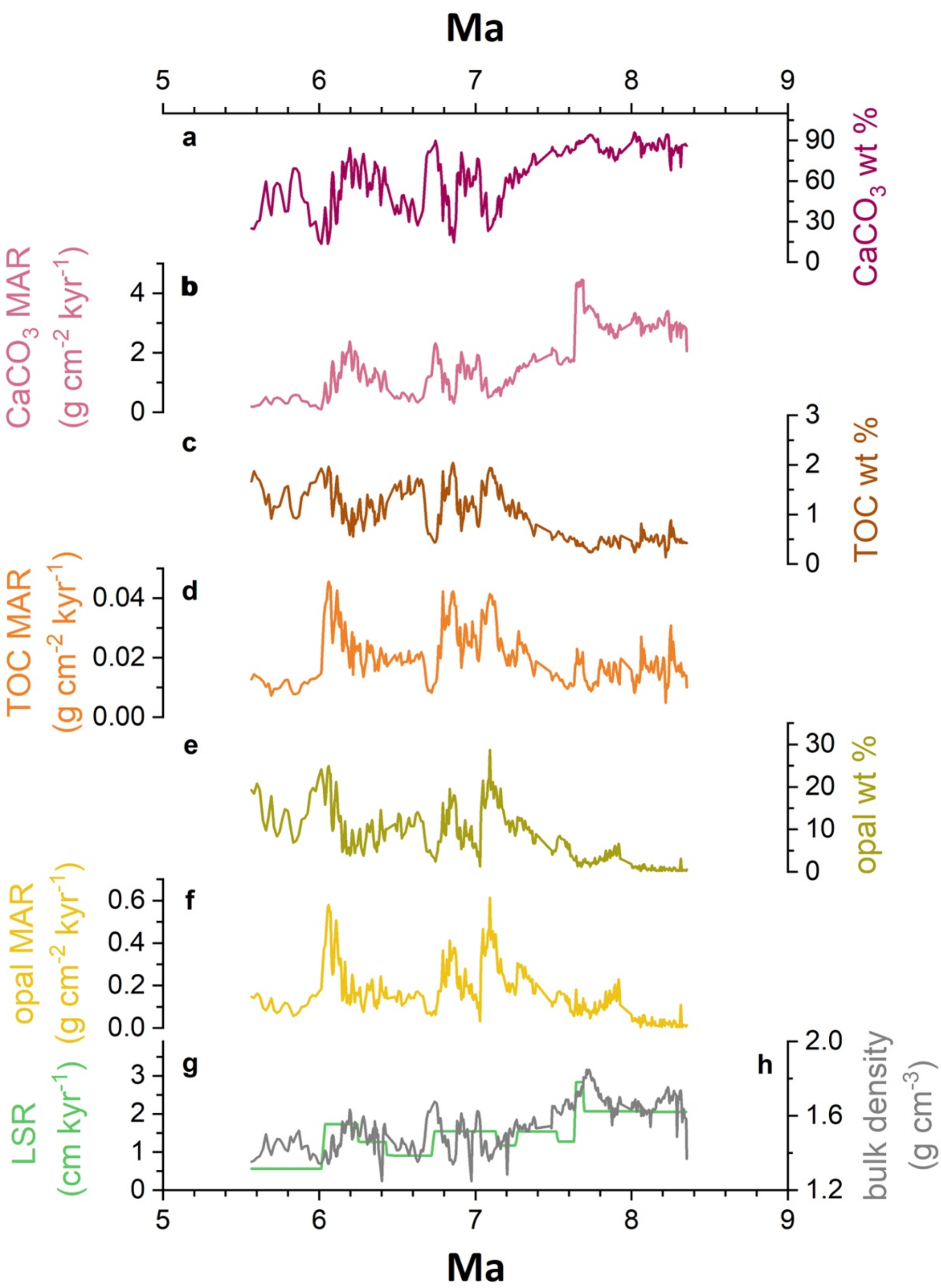

Fig. 4.1 Variations in concentrations (weight percent) and fluxes (MAR) at site U1541. **a** $CaCO_3$ concentration **b** $CaCO_3$ flux **c** TOC concentration **d** TOC flux **e** opal concentration **f** opal flux **g** LSR at U1541 **h** bulk density at U1541.

doi:10.6342/NTU202301546

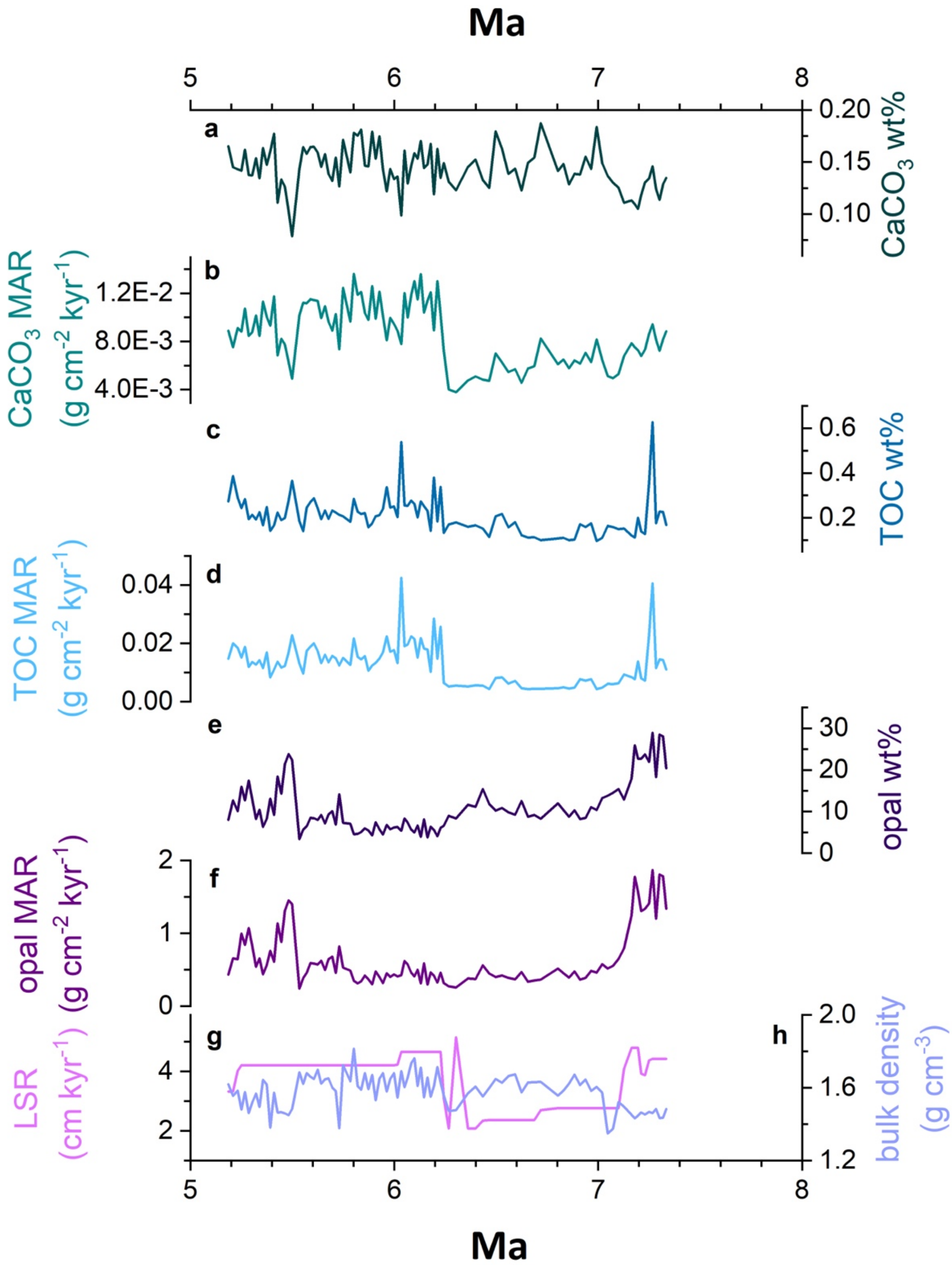

Fig. 4.2 Variations in concentrations (weight percent) and fluxes (MAR) at site U1543. **a** $CaCO_3$ concentration **b** $CaCO_3$ flux **c** TOC concentration **d** TOC flux **e** opal concentration **f** opal flux **g** LSR at U1543 **h** bulk density at U1543.

doi:10.6342/NTU202301546

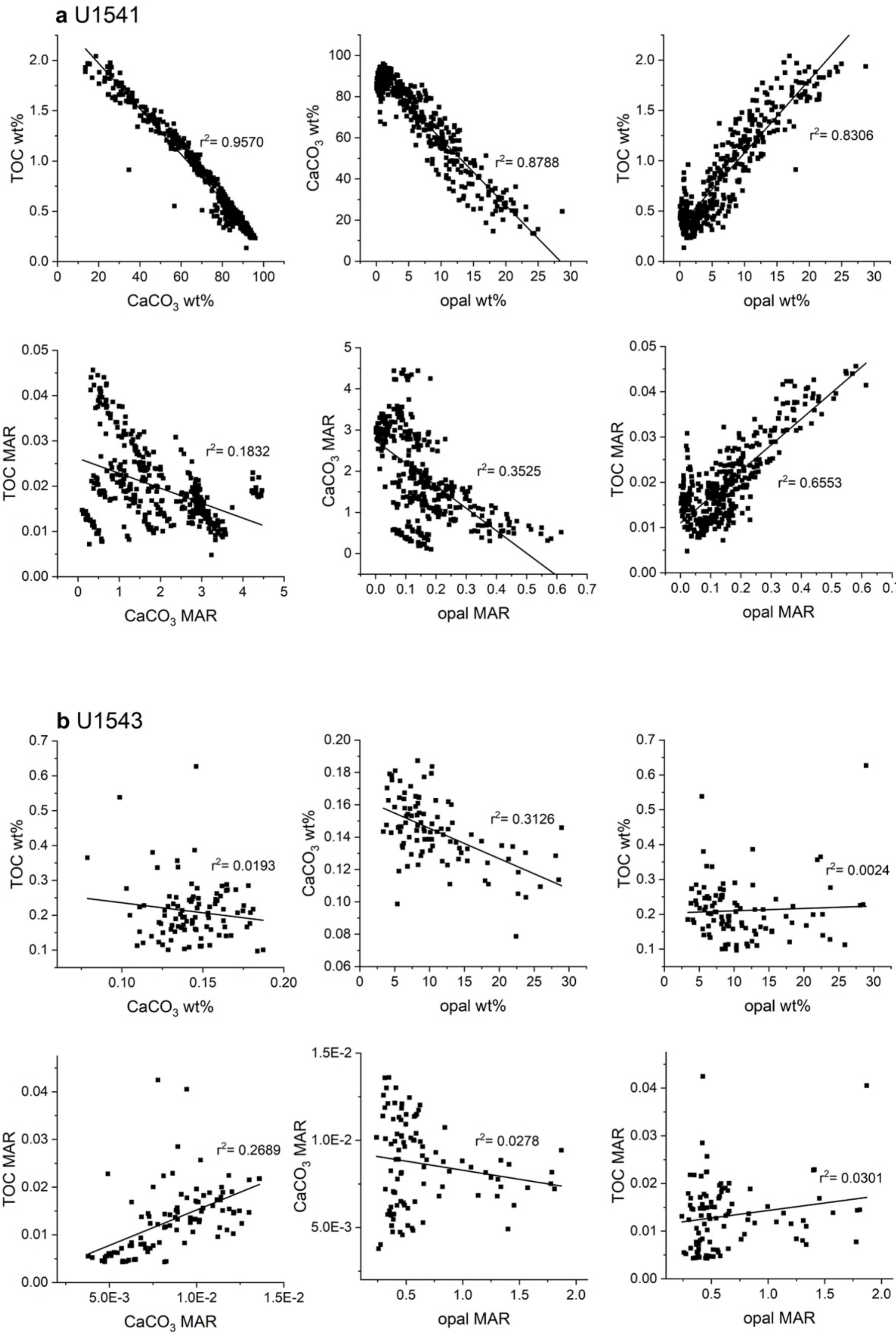

Fig 4.3 Correlation between $CaCO_3$, TOC and opal wt% and MAR. **a** site U1541 **b** site U1543.

doi:10.6342/NTU202301546

5 Discussion

5.1 Testing for the Methods

5.1.1 $CaCO_3$ and TOC Analysis

We used the temperature programming function of the EA for analyzing $CaCO_3$ and TOC contents in the sediments. The temperatures and holding times are different from the default method setting (DIN19539, C1: 400°C 230s, C2: 600°C 120s, and C3: 900°C 150s), based on our testing. We used the default method to analyze the commercial standard (Leco soil standard). The carbon signal in C1 is not finished before the temperature rises to C2, the situation also happened between C2 and C3 (Fig 5.1a). This means that the TOC content may not be completely ashed and will be defined as the TIC content. The TC (%) analyzed using this method is also lower than the reported TC (%), which is not within the reported error range (Table 5.1). After testing, we modified the method (DIN19539_4) with a higher temperature and longer holding time in C1 (550°C 400s). The amount of carbon content in C1 is completely ashed before the temperature rises to C2, and also in C2 to C3 (Fig 5.1b), which means the TOC content can have a better constraint using this method.

doi:10.6342/NTU202301546

We also tested the accuracy of the division of TOC and TIC content. DGS TC #1 and DGS OC #1 are analyzed using the temperature program DIN19539_4. They are the mudstone from Gutingkeng Formation, in southwestern Taiwan. We freeze-dried and ground the mudstone and divided them into two portions. One of them was treated by HCl and there would be no $CaCO_3$ (almost all of the TIC) left supposedly, which is the DGS OC#1. The other portion is the DGS TC #1. Although we found that there is still little TIC content in the DGS OC #1, the TOC content in DGS TC #1 and DGS OC #1 are comparable (Table 5.2 and Fig. 5.2). This indicates that the temperature programming method is comparable to the conventional acidification method for the TOC.

We further analyzed the stability of EA and the temperature program we used (DIN19539_4). All the TC (%) of Leco soil standard are within the reported error range (Fig. 5.3), with a standard deviation of 0.015 (%), which ensures the accuracy of this instrument and the method. We also found that the testing data of DGS OC #1 are very stable, which has a standard deviation of 0.010 (%), thus we use DGS OC #1 as an in-house standard in our further analysis.

doi:10.6342/NTU202301546

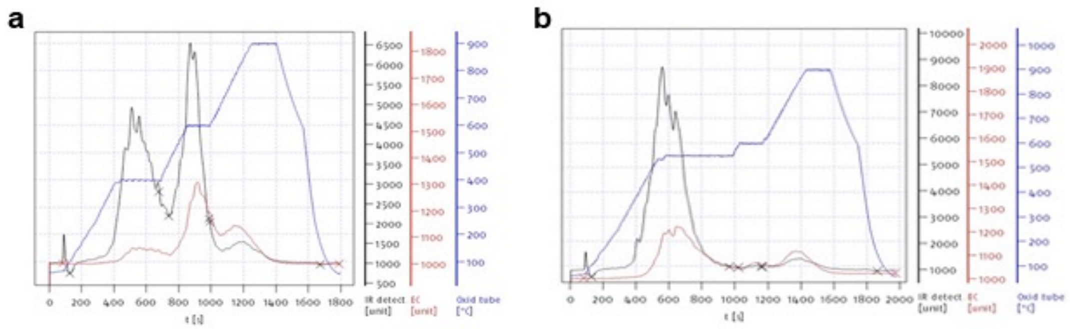

Fig. 5.1 The EA signal graph of the analysis for the Leco soil standard. **a** default method of the EA (DIN19539) **b** modified method (DIN19539_4) (this study). The x-axis represents the time (s); the y-axis shows the TC signal (black), TN signal (red) (not used in this study), and temperature (blue).

Table 5.1 The reported and testing data of Leco soil standard.

Reported value		**Default (DIN19539)**		**Modified (DIN19539_4)**	
TC (%)	**error (%)**	**TC (%)**	**SD (%)**	**TC (%)**	**SD (%)**
0.717	0.027	0.675	0.013	0.721	0.015

Table 5.2 TC (%) and/or TOC (%) of DGS TC #1 and DGS OC #1.

DGS TC #1						
TC (%)	error (%)	SD (%)	TOC (%)	SD (%)	TIC (%)	SD (%)
0.758	0.031	0.015	0.578	0.013	0.180	0.011

DGS OC #1						
TC (%)	error (%)	SD (%)	TOC (%)	SD (%)	TIC (%)	SD (%)
0.544	0.029	0.010	0.516	0.009	0.032	0.007

*error (%) is the average error propagation of TC (%), SD (%) is the standard deviation.

doi:10.6342/NTU202301546

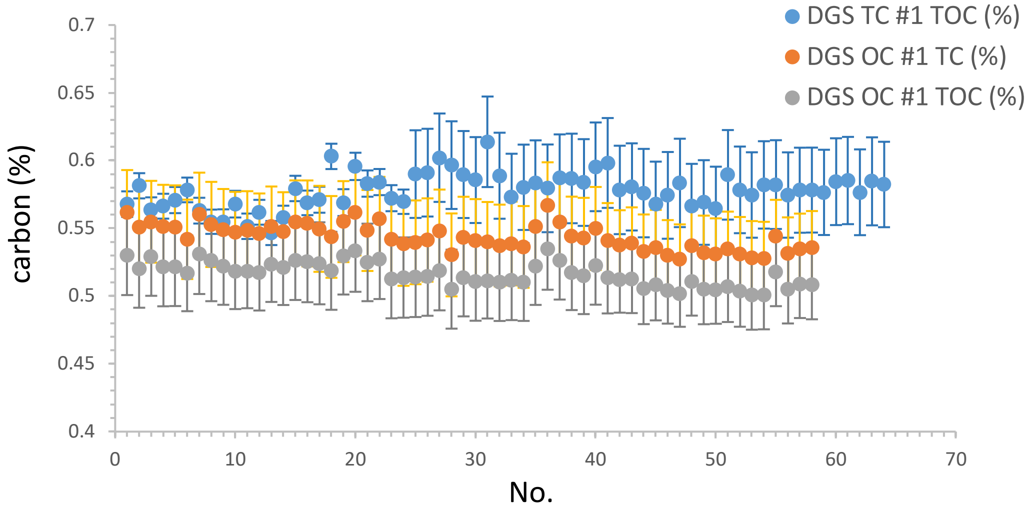

Fig. 5.2 The testing data of DGS TC #1 and DGS OC #1 (TOC content). The error bars of TC (%) are the error propagation, while TOC (%) are the proportion error. All testing data are shown in Appendix Tables 6 and 7.

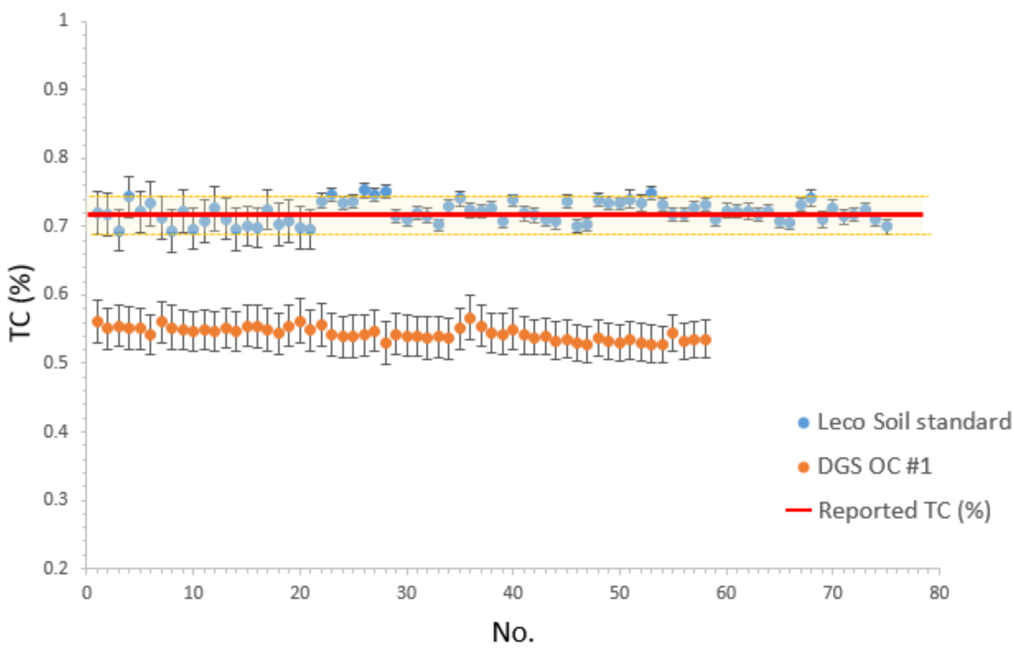

Fig. 5.3 TC (%) of Leco soil standard and DGS OC #1. The red line is the reported TC (%), while the yellow bar is the reported error range.

doi:10.6342/NTU202301546

5.1.2 Opal extraction

We generally follow Mortlock and Froelich (1989) in extracting opal from the sediments. We applied a sequential extraction, in which the samples are extracted for 1, 2.5, 4, 5, and 6.5 h. For high opal concentration samples, the opal contents can also be leached in 5 h, which agrees with the extraction time in Mortlock and Froelich (1989). However, Na_2CO_3 is not strong enough to extract most of the Si content in the high-opal samples (Fig. 5.4b, c). We also sent our testing samples to Kyushu University, Japan, in order to reconfirm the accuracy of our extraction procedure. Our results show very similar opal wt%. In addition, the microscopic image of two samples after alkaline extraction with 2 M NaOH and 2 M Na_2CO_3, shows that there are still fragments of siliceous organisms in the residue sediment after extraction using 2 M Na_2CO_3, while there are no biogenic siliceous components present in the residue using 2 M NaOH (Fig. 5.5). After testing, we decided to use 2 M NaOH instead of 2 M Na_2CO_3 for a 5 h extraction procedure.

Table 5.3 Comparison of opal wt% with Kyushu University.

	opal wt%	
	Kyushu Univ.	this study
U1541B 14H-5W 145-150m	2.5	2.1
U1543A 29H-5W 145-150m	16.4	17.6

doi:10.6342/NTU202301546

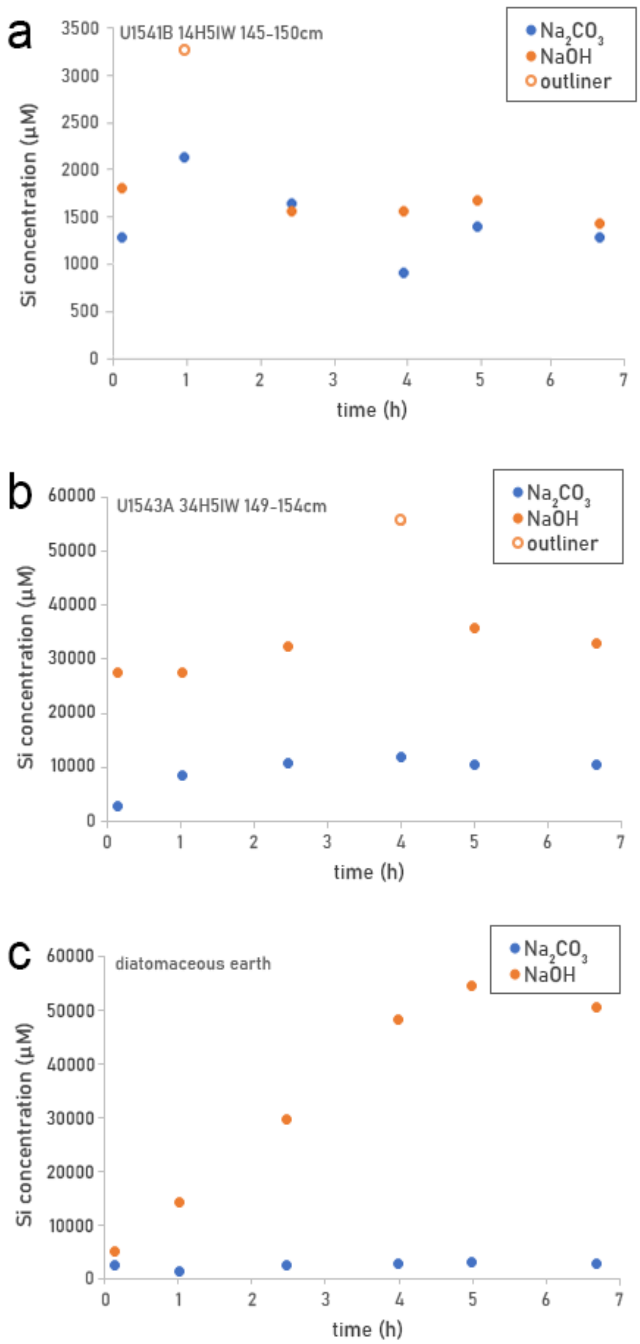

Fig. 5.4 Sequential opal extraction test.

doi:10.6342/NTU202301546

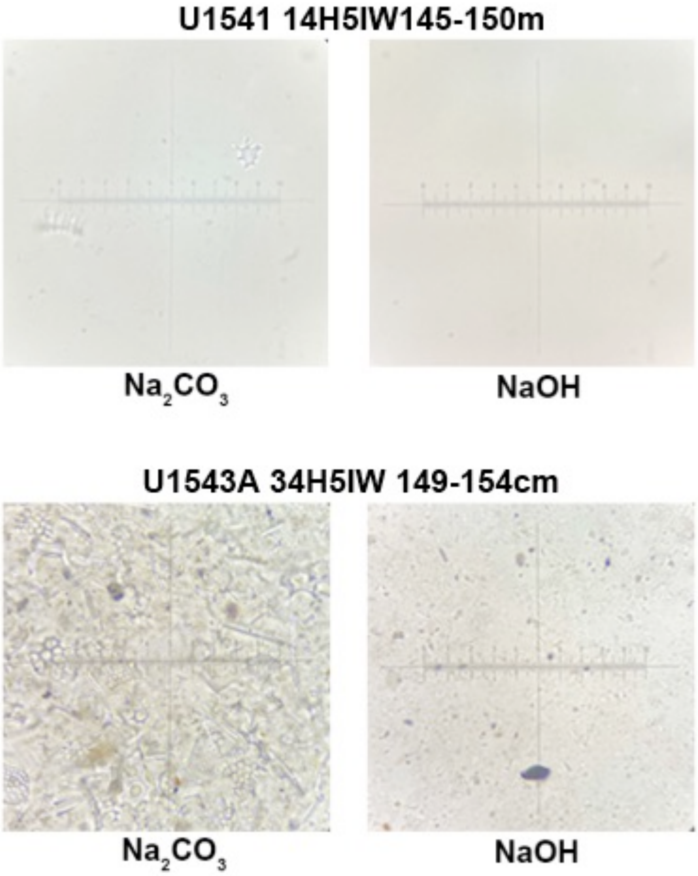

Fig. 5.5 Microscopic image of the samples after alkaline extraction with 2 M NaOH and 2 M Na_2CO_3.

5.2 MAR versus weight percent

Weight percent presents the relative abundance of components in the sediments, thus can show relative productivity changes. In our results, $CaCO_3$ and opal concentrations at site U1541 sustain a negative relationship during 8.4 to 5.6 Ma, which $CaCO_3$ (opal) concentration has a general decreasing (increasing) trend. This implies that the productivity in site U1541 has a transition to siliceous-dominated production from

doi:10.6342/NTU202301546

calcareous domination, as the fraction of opal ($CaCO_3$) concentration is rising (decreasing) throughout the period.

However, the opal and $CaCO_3$ weight percent values, influenced by the density of the components and dilution by the matrix, cannot directly represent the preservation flux. To be specific, weight percent values can change significantly with equivalent burial fluxes, due to dilution by other components (Lyle, 2003). Opal-rich sediments are more porous, so they have lower bulk density than $CaCO_3$-rich sediments (Lyle, 2019). Thus, the different compositions of sediments vary in their bulk density. For example, the $CaCO_3$, TOC, and opal fluxes (MAR values) were low during 6.0 to 5.6 Ma (Fig. 4.1), while their concentrations (weight percent values) were high, as the concentration values can only represent the fraction of the components in the sediment, but not the actual accumulation flux. Therefore, MAR (flux) can correct for the influences of dilution in the sediments (Howard and Prell, 1994) and directly represent the burial fluxes.

5.3 Burial fluxes variation control

Productivity variation controls burial fluxes in the Pacific sector of the Southern Ocean. The opal flux generally refers to the changes in productivity, as biogenic opal accumulates in sediment when siliceous (diatom) production is high (Cortese et al, 2004).

doi:10.6342/NTU202301546

Silica dissolution rates are higher in the surface ocean than in deep sea (Van Cappellen et al., 2002) for the surface ocean has much lower silicate concentrations than the deep ocean. High siliceous production can lead to the aggregation of opal-rich marine particles, shorten the transport time through the water column and reduce the surface area to interact with water (Akagi et al., 2014). Therefore, a higher siliceous production rate leads to a lower dissolution rate, and thus, opal fluxes variations usually refer to productivity rather than preservation changes by bottom water chemistry.

Two major controlling factors of $CaCO_3$ fluxes are changes in $CaCO_3$ dissolution rates or productivity. Major $CaCO_3$ dissolution occurs in the deep ocean due to low temperature, high pressure, and low pH, related to the bottom water chemistry (Edmond, 1974). If dissolution rate variation is the major factor of $CaCO_3$ flux changes, there will be high coherence between $CaCO_3$ MAR time series from different regions in an ocean basin, as it is controlled by large-scale ocean chemistry. In contrast, a lack of basin-wide systematics indicates production rate of calcareous organisms is the major factor affecting $CaCO_3$ burial, instead of ocean chemistry changes (Lyle, 2003). Therefore, by comparing $CaCO_3$ fluxes from different regions in an ocean basin, we can determine whether preservation or productivity is the primary factor controlling $CaCO_3$ flux variations.

doi:10.6342/NTU202301546

According to our results, $CaCO_3$ flux is high at site U1541 while it is significantly low at site U1543 during 8.4 to 5.2 Ma (Fig. 5.6a and b). The two sites are both located in Southern Ocean and the ACC, so they may share similar ocean chemistry. Within the similar bottom water chemistry, $CaCO_3$ fluxes at site U1541 and U1543 still show significant differences (range from 0.10 to 4.46 g cm^{-2} kyr^{-1}, and 4.02×10^{-3} to 1.36×10^{-2} g cm^{-2} kyr^{-1}, respectively. Thus, the major controlling factor of $CaCO_3$ burial fluxes is productivity instead of preservation. Therefore, we suggest that both opal and $CaCO_3$ flux variations in the Pacific sector of the ACC during the late Miocene are controlled by changes in productivity.

doi:10.6342/NTU202301546

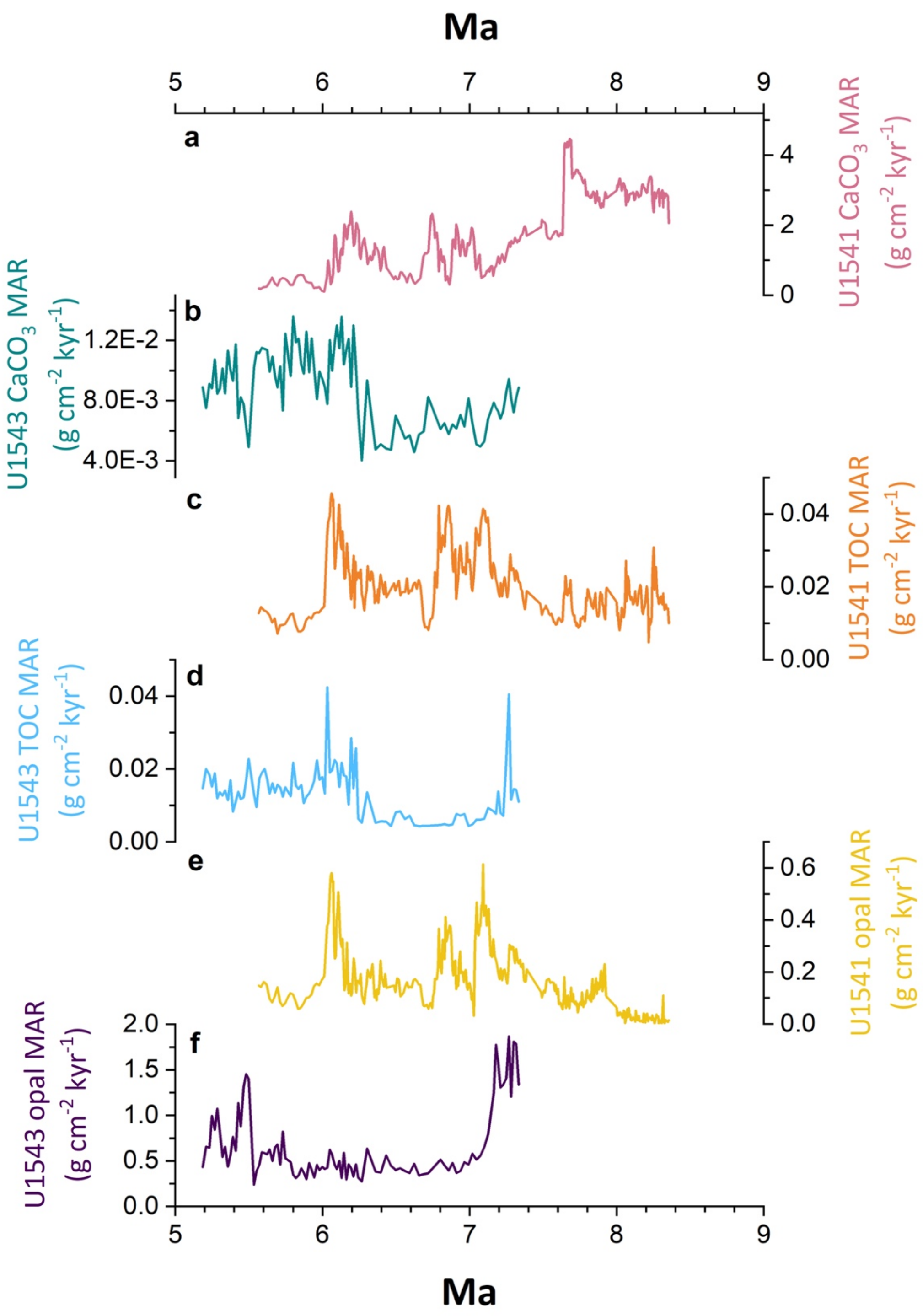

Fig. 5.6 Variations in fluxes (MAR) at site U1541 and U1543. **a** U1541 $CaCO_3$ flux **b** U1543 $CaCO_3$ flux **c** U1541 TOC flux **d** U1543 TOC flux **e** U1541 opal flux **f** U1543 opal flux.

doi:10.6342/NTU202301546

5.4 ACC expansion and the LMC

Site U1541 is located in the central Pacific sector of the Southern Ocean, which is in the open ACC. Therefore, we use site U1541 to represent general productivity in the the Southern Ocean. The high primary productivity in Southern Ocean during the late Miocene may be related to the decline of atmospheric CO_2 and eventually lead to the LMC. The $CaCO_3$ (opal) concentration and flux at site U1541 show a sharp decline (rising) trend at 7.6 Ma (Fig. 5.7). The $CaCO_3$ and opal fluxes sustain a negative relationship during 8.4 to 6.0 Ma. Since both $CaCO_3$ and opal fluxes are controlled by productivity, the opposite trends between $CaCO_3$ and opal support previous observations that decreasing calcareous productivity is usually due to increasing siliceous production (Iglesias-Rodríguez, 2002). In contrast, TOC concentrations and fluxes show similar trends with opal between 8.4 and 5.6 Ma, which implies that siliceous organisms constitute the majority of primary production that transfer IC to OC through photosynthesis at site U1541.

The Southern Ocean is more sensitive to global climate than other oceans, and some regions in the Southern Ocean have a higher warming rate than the global average during modern global warming events. For example, the mean temperature of the Bellingshausen Sea has increased by ~1 K since 1950, while the global mean temperatures have only

doi:10.6342/NTU202301546

warmed by ~0.6 K (Clarke et al., 2007). Therefore, Southern Ocean productivity has established distinctive adaptation to drastic environmental change in this area, making them particularly sensitive to the influence of climate change, as the nutrient pool in the Southern Ocean is strongly biased between warm and cool periods (Fierro-Arcos et al., 2023). Nutrient level is a major factor that controls productivity (Iglesias-Rodríguez, 2002). Si is abundant in Southern Ocean (Tréguer, 2014), therefore higher nutrient in Southern Ocean surface water can stimulate the growth of siliceous organisms which threaten the growth of calcareous organisms (Sigman and Hain, 2012). The increasing nutrients by cooling of surface water to enhance vertical mixing and upwelling lead to higher opal concentration and flux. Increasing dust import from land is unlikely a cause of higher nutrients at site 1541, as this site is located in the pelagic region which is ~3300 km away from the continents. As the opal flux and concentration were low during 8.4 to 7.6 Ma, suggesting that the water was relatively nutrient-depleted during this period at site U1541. The low nutrients imply that during (or before) 8.4 to 7.6 Ma, there was a weak upwelling due to warmer surface water. The reduction of opal productivity leads to low TOC preserved in the sediment which favored the domination of calcareous organisms (average $CaCO_3$ concentration 86.1%) due to low siliceous productivity. We further suggest that during this period, site U1541 may have been located outside of the

doi:10.6342/NTU202301546

ACC, and thus the surface water in this location was warm and not rich in nutrient (Fig. 5.9a), causing low siliceous production.

The opal increases and $CaCO_3$ crashes after 7.6 Ma coincided with the cooling trend in the southern hemisphere (30°-50°). As the Southern Ocean is more susceptible to the global climate, the Antarctic ice sheet volume has increased since the middle Miocene, and further leads to ACC expansion (Leutert et al., 2020). During the ice age, the sea-ice-free cold-water region has been widened due to the presence of Ross Gyre, which intensified upwelling by destratification (Benz et al., 2016). We suggest that the ACC expansion leads site U1541 to be situated inside the ACC experiencing cool sea surface temperature between 7.6 and 6.0 Ma (Fig. 5.9b). The cooling due to ACC expansion during this period destratified the seawater, allowing the mixing of waters and bringing nutrients to the surface water through upwelling (Sigman and Hain, 2012).

The westerly winds shifted northward and the Southern Ocean cooled off the sea surface took place in this region (Leutert et al., 2020). During the ice age, the westerly winds have been weakened due to lower atmospheric CO_2 and less thermal contrast in the atmosphere between high and low latitudes, which also leads the strongest winds to locate north of the ACC (Toggweiler & Russell, 2008). After 6.0 Ma, cooling continued (Herbert

doi:10.6342/NTU202301546

et al., 2016). The continued ACC expansion eventually reached a point where there is no further increase in ACC transport (Barker and Burrell, 1977). From 6.0 to 5.5 Ma, both $CaCO_3$ and opal fluxes remained low, in response to low LSR (Fig. 4.1). The most likely scenario to explain the data is that northward-shifted westerly winds eventually have less influence on site U1541 due to cooling, and the ACC was weakened (Fig. 5.9c). The Slowed down of the deep-sea circulation presented by Hassold et al. (2009) agreed with our observation and explanation. Therefore, we conclude that the ACC is the major control of productivity at site U1541.

In addition, we suggest that the increasing primary productivity in the Southern Ocean was related to the LMC event. The global reduction of atmospheric CO_2 during the late Miocene was possibly the main driving factor of the LMC (Herbert et al., 2016). Previous research showed that the increasing global primary productivity may have decreased the atmospheric CO_2, as more atmospheric CO_2 is utilized through photosynthesis (Ramaswamy and Gaye, 2006). The opal concentrations and fluxes at site U1541 have reached their peaks during ~7.0 Ma, which was the onset of the LMC. This suggests that the increased primary productivity (siliceous production in this study) in the Southern Ocean may be one of the driving factors of the LMC event.

doi:10.6342/NTU202301546

However, the productivity records in equatorial to mid-latitude regions in other oceans do not show intensive increasing trends during the LMC (Fig. 5.10) (Lyle et al., 2019, Drury et al., 2021, Peterson et al., 1990, Diester-Haass et al., 2005). The high productivity and cooling event might have occurred primarily in high latitude regions after 7.6 Ma (Drury et al., 2021 and this study), implying that the temperature gradient between the equator and the polar regions was intensified. The increased latitudinal temperature gradient can strengthen the trade winds due to the increased atmospheric air mass movement, which leads to stronger upwelling in equatorial to mid-latitude regions (Pillot et al., 2023). Although the primary productivity in equatorial regions during the LMC do not pronounce rising trends as high latitude regions, they are relatively higher than that before ~7.6 Ma (Lyle et al., 2019, Drury et al., 2021, Peterson et al., 1990, Diester-Haass et al., 2005), which may cause by increased nutrient reaching the surface water by stronger wind-driven upwelling. This implies that high-latitude cooling and increased latitudinal temperature gradients can lead to the LMC (Drury et al., 2021), and our results at site U1541 also agree this hypothesis. Therefore, the high productivity in Southern Ocean during the late Miocene may be related to the decline of atmospheric CO_2 and eventually lead to the LMC. Further evidence, such as sea surface temperature records in Southern Ocean, are required to examine our hypothesis on the mechanisms of the LMC.

doi:10.6342/NTU202301546

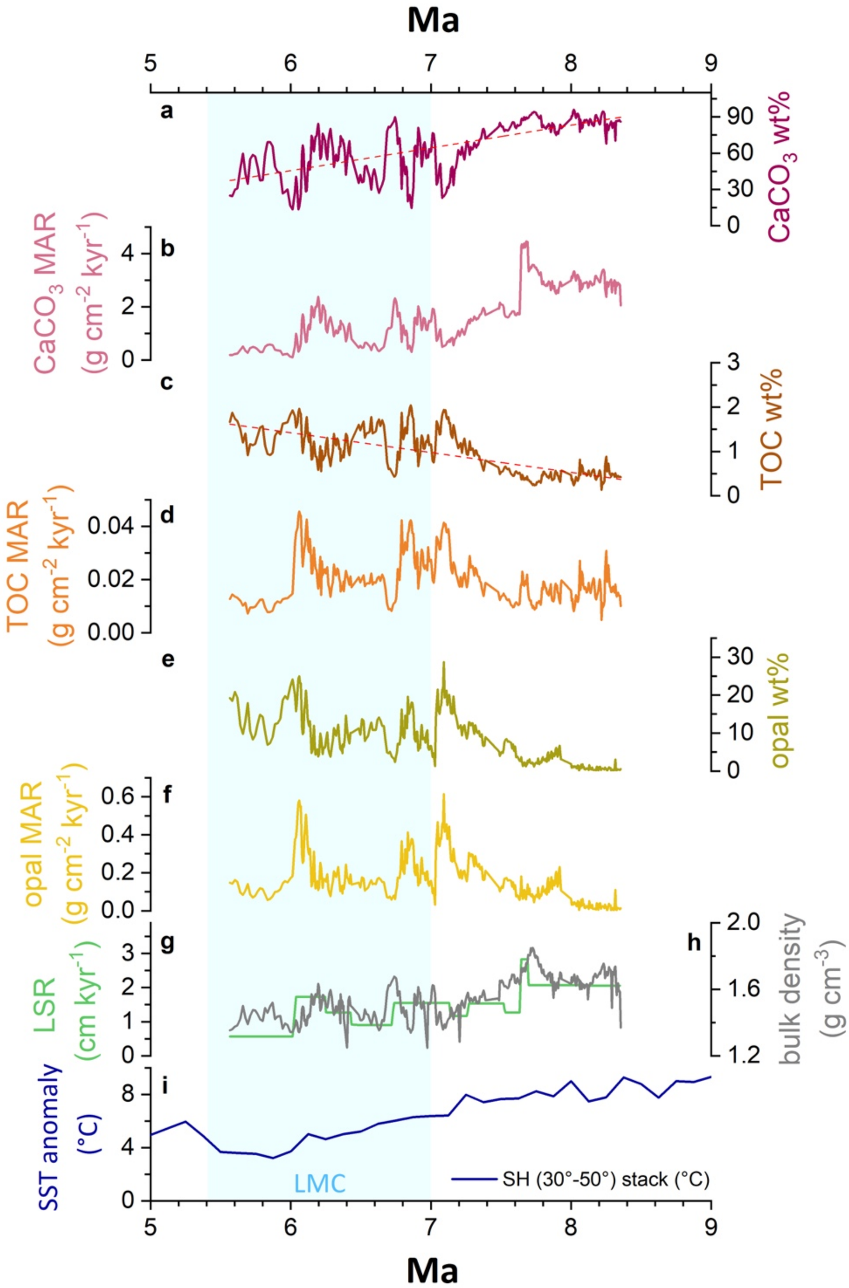

Fig. 5.7 Variations in concentrations and fluxes at site U1541. **a** $CaCO_3$ concentration **b** $CaCO_3$ flux **c** TOC concentration **d** TOC flux **e** opal concentration **f** opal flux **g** LSR **h** dry bulk density **i** Southern Hemisphere (30°-50°) SST anomaly from Herbert et al. (2016). Blue vertical bar is the LMC event.

doi:10.6342/NTU202301546

5.5 Nutrient variations at site U1543

Comparing to site U1541, site U1543 has significantly lower $CaCO_3$ and higher opal concentrations and fluxes (Fig. 5.6). According to section **1.2**, higher siliceous production is found in nutrient-rich environment which is caused by stronger upwelling, lower sea surface temperature and higher dust input (Martinez-Garcia et al., 2011, Li et al., 2020, Martin et al., 1989, Van cappellen et al., 2002). Site U1543 is located in the east Pacific sector of the ACC, which is also located on the flow path of the Cape Horn Current (CHC) (Lamy et al., 2021), a branch of the ACC and constitutes largely to the transport in the northern Drake Passage (Well and Roether, 2003). Significant amount of ACC water is transported by the CHC to the east through Drake Passage in a narrow belt (Chaigneau and Pizarro, 2005). When westerly wind enters a narrower belt and rounds the cape, it intensifies and strengthens the ACC. The wind and current strength around site U1543 is stronger comparing to site U1541 and lead to intensification of upwelling. Stronger upwelling can bring more nutrients to the surface water from the bottom (Martinez-Garcia et al., 2011), thus site U1543 has richer nutrient than site U1541.

Besides intense upwelling to support major nutrients, iron dust from land supply silicate and iron to support productivity at site U1543. Murray et al. (2012) suggested that iron deposition was highly tied to opal deposition than other biogenic components.

doi:10.6342/NTU202301546

Previous studies also show that there is positive relationship between dust flux and opal deposition in Subantarctic region (e.g., Chase et al., 2003). Many phytoplankton functions, such as electron transport chain of photosynthesis, require iron (Sigman et al., 2012). This kind of nutrient can enter the surface water through terrestrial processes which bring aeolian iron dust to the ocean (Martin et al., 1989; Van cappellen et al., 2002). Site U1543 is situated only about ~204 km west to the Chilean coast (Fig. 3.1), so the siliceous production may potentially have more influence from the iron dust than at site U1541. The sum of the percentages of $CaCO_3$, TOC and opal at site U1543 is far from 100% (Fig. 5.8i), which means there are other component(s) constitute a certain fraction of the core. The proceeding report of site U1543 shows that 68.7 % of the core consist of terrigenous and/or diatom-bearing clay/silt (Lamy et al., 2021) (Appendix table 12). Previous studies also suggest that volcanic ash can fertilize the east Pacific sector of Southern Ocean and stimulate productivity (Vergara-Jara et al., 2021). This may indicate that the sediment at site U1543 is largely affected by terrigenous component resulting from volcanic activities and weathering, and has a positive impact to the siliceous production. The TOC and opal concentrations and fluxes at site U1543 did not show good correlation (Fig. 4.3b), which may also be the result of terrigenous TOC input.

doi:10.6342/NTU202301546

In the true south of the Antarctic Polar Front (APF), dust flux and opal production do not sustain a positive relationship derived from proxy records in the Subantarctic region (Jaccard et al., 2013). Factors other than dust input must have also regulated the production and export of opal in the Southern Ocean. We attribute different strengths of upwelling in different regions resulting in different water chemistry to enhance. Therefore, we suggest that the intense wind-driven upwelling and iron dust input are the main factors of high nutrient at site U1543, which also cause higher siliceous and significantly low calcareous production at this site.

Despite the higher range of opal flux and concentration, site U1543, located in the CHC, is sensitive to climate variations (Lamy et al., 2015). Between 7.1 and 7.0 Ma, opal and TOC fluxes dramatically drop to low values (Fig. 5.8), which may cause by a sudden nutrient depletion event. One of the hypotheses is the ACC expansion may lead to weaker upwelling at site U1543. Opal fluxes are usually used to represent upwelling strength, as upwelling is important in nutrient transportation to surface water (Anderson et al., 2009). The opal crash at site U1543 during 7.1 to 7.0 Ma may be probably caused by weakened upwelling. In section **5.3**, we mentioned that the ACC expansion at ~7.6 Ma leads to destratification at site U1541. However, site U1543 is located near the Chile Margin which is situated in the CHC, an ACC branch before entering the Drake Passage (Lamy

doi:10.6342/NTU202301546

et al., 2021). According to the studies of the modern Southern Ocean, during ACC and Antarctic Sea ice expansion regards to cooling, westerly winds shifted northward and enhance the ACC transport into the Humboldt Current System, the current flows northward into the Pacific Ocean (Fig. 5.9c, Lamy et al., 2015). At the same time, the ACC water which flows into the Drake Passage through CHC is weakened. Toyos et al. (2020) suggest that during the Last Glacial Maxima (LGM), the throughflow change is 44% lower than during the Holocene at the Chilean margin, which has diminished the upwelling at this region. Therefore, we suggest that the Southern Ocean cooling and ACC expansion during the late Miocene, may lead to weaker upwelling at site U1543 and decreasing nutrients, and eventually the decline of siliceous productivity.

After about 5.5 Ma, the opal concentration and flux have increased to higher values. The retreating ACC may result in higher siliceous productivity at site U1543. When the sea temperature becomes warmer, the westerly winds and the ACC shift poleward, and the winds will align with the ACC again (Fig. 5.9d, Toggweiler and Russell, 2008). Thus, the Antarctic warming can intensify upwelling at site U1543 by pole-ward shifted westerly winds, and stimulate productivity by bringing more nutrients to the surface water (Lamy et al., 2015). This hypothesis coincides with the increasing southern hemisphere

doi:10.6342/NTU202301546

(30°-50°) sea surface temperature presented by Herbert et al., 2016 (Fig. 5.3i). Therefore, we suggest that ACC also has significant influences on the productivity in site U1543.

doi:10.6342/NTU202301546

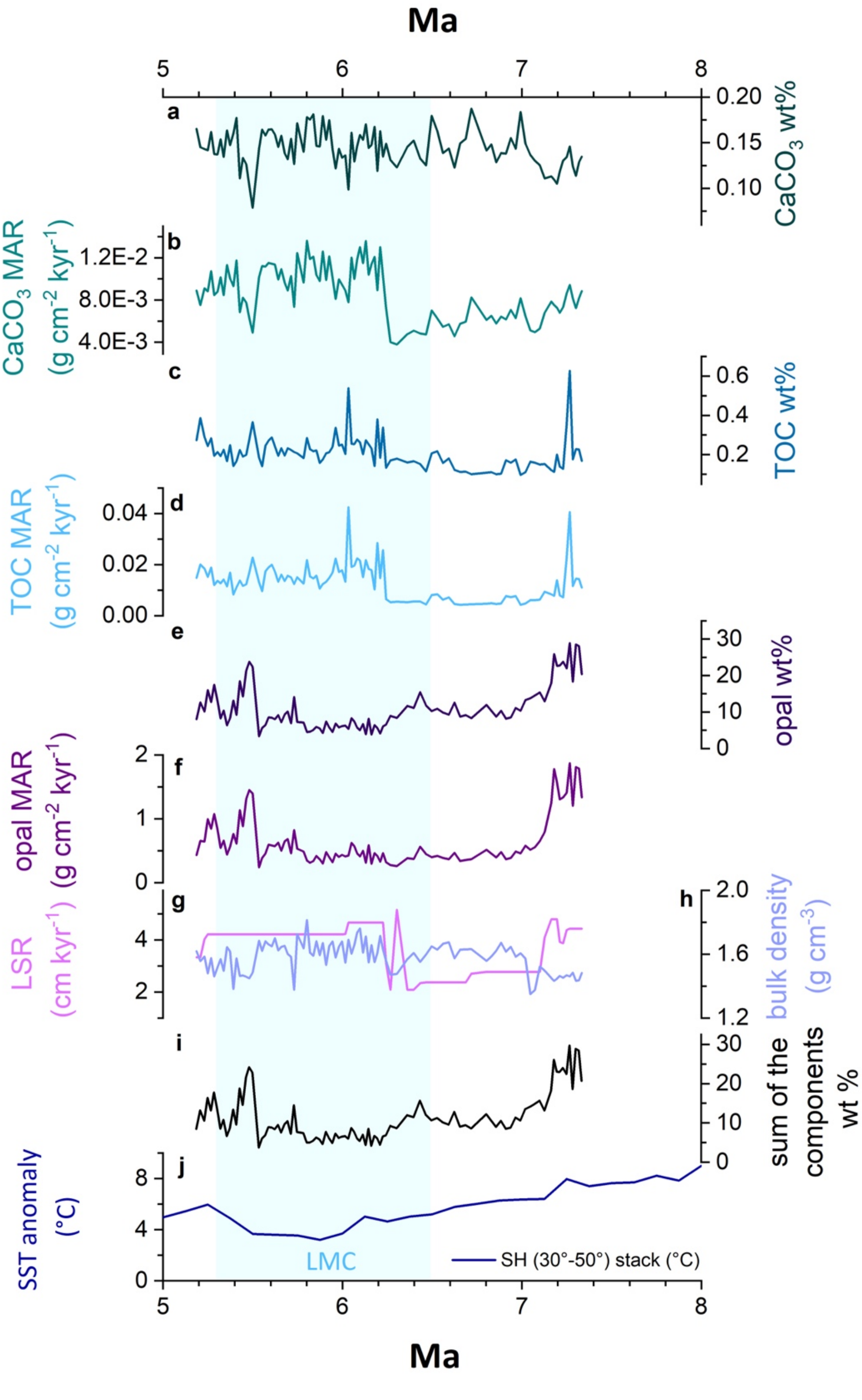

Fig. 5.8 Variations in concentrations and fluxes at site U1543. **a** $CaCO_3$ concentration **b** $CaCO_3$ flux **c** TOC concentration **d** TOC flux **e** opal concentration **f** opal flux **g** LSR **h** dry bulk density **i** sum of the components **j** Southern hemisphere (30°-50°) SST anomaly from Herbert et al. (2016). Blue vertical bar is the LMC event.

doi:10.6342/NTU202301546

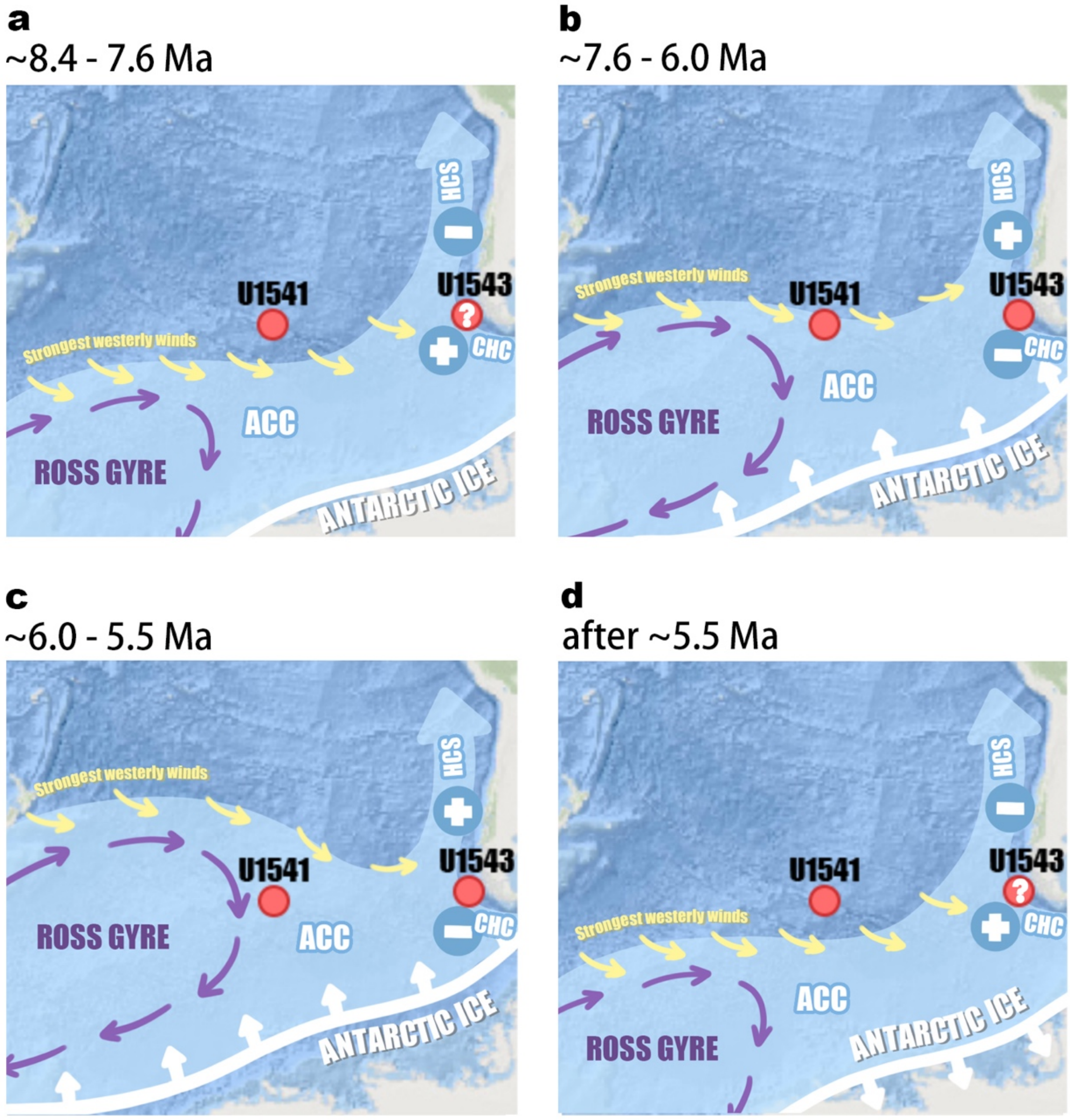

Fig. 5.9 Schematic illustration of the ACC dynamics during the late Miocene. **a** ~8.4-7.6 Ma **b** ~7.6-6.0 Ma **c** ~6.0-5.5 Ma **d** after ~5.5 Ma. ACC =Antarctic Circumpolar Current, CHC = Cape Horn Current, HCS= Humboldt Current System. The yellow arrows represent the strongest westerly winds, while the purple arrows represent the Ross gyre. The while lines and arrows represent the Antarctic ice sheet.

doi:10.6342/NTU202301546

5.6 Link between primary productivity and LMCIS

Many studies have mentioned the correlation between LMCIS and primary productivity. For example, Diester-Haass et al. (2005) suggest that there is an increasing productivity trend in the Atlantic Ocean during LMCIS. Paleoproductivity records in the equatorial Pacific from Lyle et al. (2019) also support their result. The high rates of biogenic opal and $CaCO_3$ accumulation event during this period is defined as Late Miocene Biogenic Bloom (LMBB) (e.g., Lyle et al., 2019). LMBB can lead to LMCIS, as ^{12}C is used priory when organisms carry out photosynthesis in the surface water, thus higher primary production can lead to a negative $\delta^{13}C$ shift to the ocean bottom (Du et al., 2022). We compare our data with the studies in the Pacific, Atlantic, and Indian Oceans (Lyle et al., 2019, Drury et al., 2021, Peterson et al., 1990, Diester-Haass et al., 2005). These studies generally use $CaCO_3$ flux to represent primary productivity, as the TOC and CaCO3 fluxes sustain positive relationships which can imply $CaCO_3$ in those study areas constitute the majority of primary productivity (Lyle et al., 1988). However, in our study, only opal and TOC concentrations and fluxes sustain positive relationship at both U1541 and U1543, indicating that the majority of primary production in the Pacific sector of the Southern Ocean is siliceous productivity. Therefore, in this study, we use TOC fluxes to discuss the relationship between productivity and LMCIS.

doi:10.6342/NTU202301546

Fig 5.9 shows the TOC fluxes in this study and $CaCO_3$ fluxes from other research (Lyle et al., 2019, Drury et al., 2021, Peterson et al., 1990, Diester-Haass et al., 2005), which are used to represent primary productivity. The sites in the Pacific, Atlantic, and Indian Oceans are chosen based on the compilation by Pillot et al. (2023), in which LMBB has been distinctly identified. During LMCIS, primary productivities at all sites show increasing trends, except site U1543. We do not have data at site U1543 before 7.3 Ma, thus we are not able to find out if there is an increasing trend at site U1543 during the onset of LMCIS. In addition, TOC fluxes drop sharply during 7.1 to 7.0 Ma, which is different from site U1541 and also other oceans. Despite the situation above, U1543 TOC flux still reaches its peak during LMCIS, which implies that there is also high productivity during LMCIS at site U1543. Therefore, we suggest that besides the Pacific, Atlantic, and Indian Oceans which are more investigated in previous studies, the Southern Ocean also has high primary production during the LMCIS. Based on these records, we suggest that increasing primary productions do have influences on LMCIS.

However, if the enhanced primary production is the major mechanism that leads to LMCIS, the planktonic foraminiferal $\delta^{13}C$ ($\delta^{13}C_{surface}$) would show the opposite trend to the decreasing benthic foraminiferal $\delta^{13}C$ ($\delta^{13}C_{bottom}$). As ^{12}C is used first during photosynthesis, ^{13}C will be more abundant in the surface water, thus leading to increasing

doi:10.6342/NTU202301546

$\delta^{13}C_{surface}$. When these organisms sink to the water bottom, they release and cause more negative $\delta^{13}C_{bottom}$ (Du et al., 2022). Nevertheless, during LMCIS, both $\delta^{13}C_{surface}$ and $^{13}C_{bottom}$ show negative shifting trends (Drury et al., 2018, Holbourn et al., 2018, Westerhold et al., 2020), which means although the enhanced primary productivity is related to the LMCIS, there are other mechanisms that lead to the onset of LMCIS. The C3:C4 shift and the uplift of the Tibetan Plateau itself may not be the main driving mechanism of LMCIS because of the duration and spatial distribution, which is mentioned in section **2.2**. Du et al. (2022) suggest that the combined effect of enhanced weathering by the Late Miocene Uplift of the Tibetan Plateau and C4-expansion can lead to more ^{13}C-depleted and nutrient input transferred into the ocean, which may cause a negative shift in p $\delta^{13}C_{surface}$ and stimulation of primary productivity. The sinking of dead organisms brings more ^{12}C to the bottom and leads to decreasing $\delta^{13}C_{bottom}$. This process may eventually lead to negative shifts in both $\delta^{13}C_{surface}$ and $\delta^{13}C_{bottom}$. We agree that the combination of terrestrial processes and the global ocean biogenic bloom may ultimately lead to the onset of LMCIS, however, further investigation on atmospheric circulation is needed, in order to explain the relationship between these processes and the productivity in the Southern Ocean.

doi:10.6342/NTU202301546

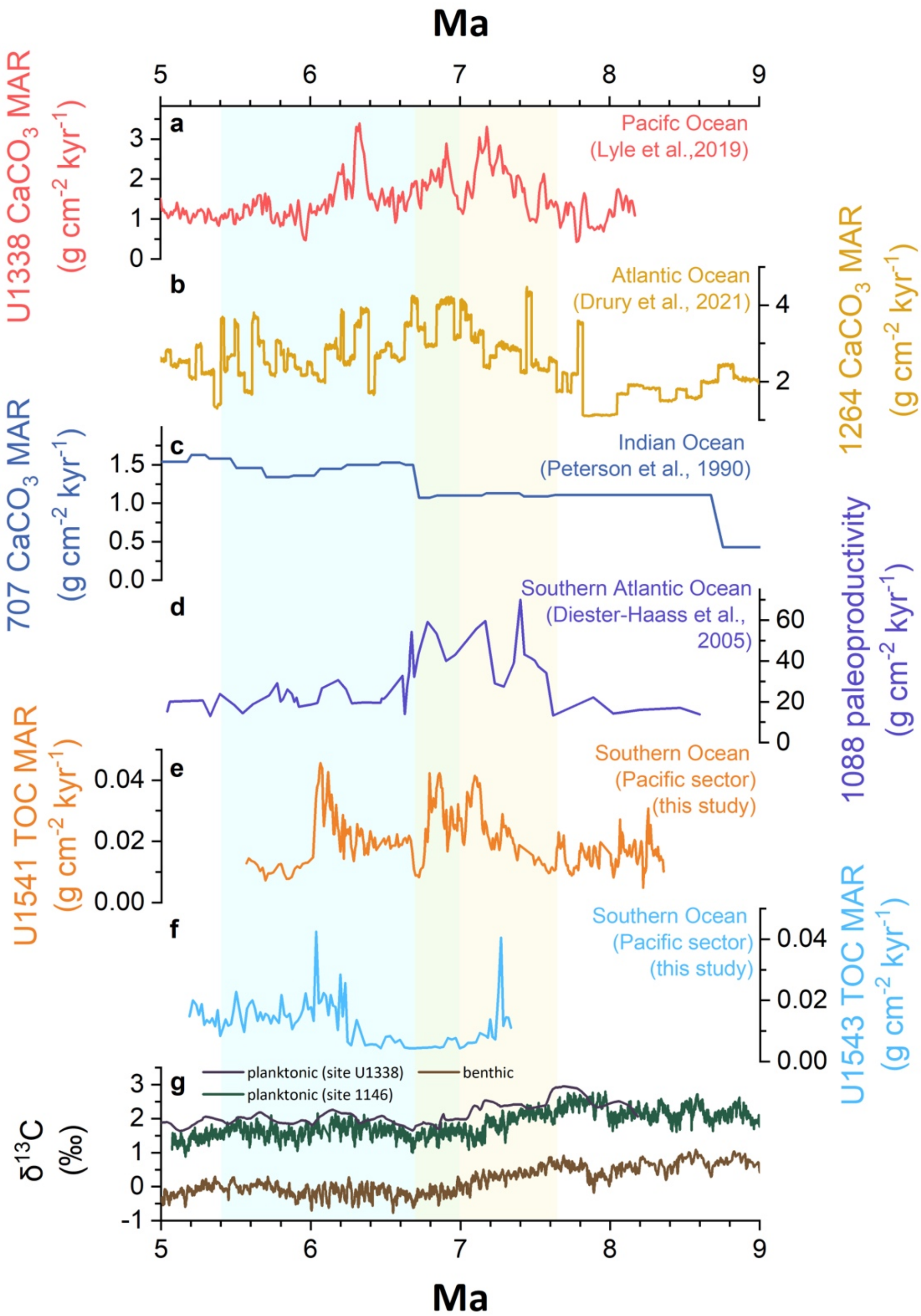

Fig. 5.10 Global primary productivity fluxes. **a** site U1338 (Pacific Ocean) $CaCO_3$ flux (Lyle et al., 2019) **b** site 1264 (Atlantic Ocean) $CaCO_3$ flux (Drury et al., 2021) **c** site 707 (Indian Ocean) $CaCO_3$ flux (Peterson et al., 1990) **d** site 1088 (Atlantic sector of Southern Ocean) Paleoproductivity flux (Diester-Haass et al., 2005) **e** site U1541 (Pacific sector of

doi:10.6342/NTU202301546

Southern Ocean) TOC flux (this study) **f** site U1543 (Pacific sector of Southern Ocean) TOC flux (this study) **g** planktonic foraminiferal $\delta^{13}C$ record at site U1338 (Drury et al., 2018) and site 1146 (Holbourn et al., 2018); benthic foraminiferal $\delta^{13}C$ record (Westerhold et al., 2020). Yellow vertical bar is the LMCIS event.

5.7 Global productivity comparison

We compared the fluxes between the Pacific, Atlantic, Indian, and Southern Oceans. Here we only use the data at site U1541, as the location of U1541 is more open in the current and has less influence from the terrigenous sediments which is mentioned in section **5.4**. According to previous studies, these proxies show similar overall patterns within the same ocean basin (e.g., Lyle et al., 2019, Diester-Haass et al., 2005). Generally, $CaCO_3$ fluxes in the Pacific and Atlantic Oceans increase during 7.6 to 6.7 Ma, then decrease gradually after 6.7 Ma, while $CaCO_3$ fluxes in the Indian Ocean rise until 5.0 Ma (Pillot et al., 2023). However, $CaCO_3$ fluxes in both the Pacific sector of Southern Ocean and the southern Atlantic Ocean drop rapidly during 7.6 to 6.7 Ma, and have a general decreasing trend throughout the late Miocene (Fig. 5.11).

Fig. 5.12 shows the TOC and opal fluxes in Pacific, Atlantic, Indian ,and different sectors of the ACC. All sites in the Southern Ocean show increasing trends during 7.6 to

doi:10.6342/NTU202301546

6.7 Ma and decrease gradually afterward. Opal flux in the Pacific Ocean also has a peak at 6.9 Ma, while TOC and opal fluxes in the Atlantic and Indian Oceans are relatively low during this period of time. Although the opal flux at U1541 (this study) reaches another peak at 6.0 Ma, the overall patterns between opal and TOC fluxes in different sectors of the ACC are similar. The variations of low accumulation period between different regions of the Southern Ocean may be caused by the different extent of ACC expansion during LMC which is mentioned in section **5.3**.

Overall, the $CaCO_3$, opal, and TOC fluxes in different sectors of the ACC show similar trends during the late Miocene. There is less correlation between the sites in and outside the ACC. This may further indicate that the productivity variations in the Southern Ocean are mainly controlled by the ACC. During LMC, productivity in the Pacific margin of the Antarctic Peninsula reaches lower values earlier, which may be caused by the northward-shifting westerly winds. Upwelling is diminished first in the more southern regions; thus, the northern regions of the ACC are influenced later. In addition, the different onset of the low production periods between the Pacific and Atlantic sectors of Southern Ocean, may imply the different extent of ACC expansion in different sectors.

doi:10.6342/NTU202301546

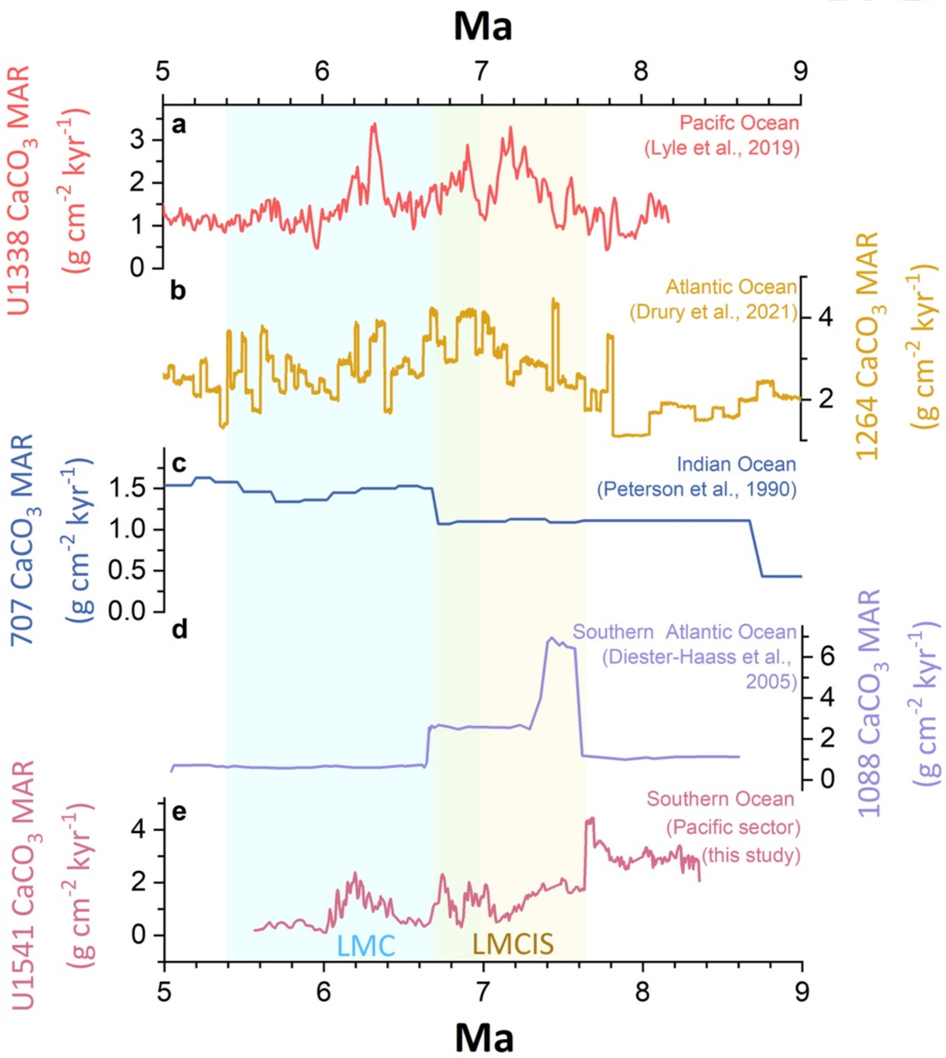

Fig. 5.11 Global $CaCO_3$ fluxes. **a** site U1338 (Pacific Ocean) $CaCO_3$ flux (Lyle et al., 2019) **b** site 1264 (Atlantic Ocean) $CaCO_3$ flux (Drury et al., 2021) **c** site 707 (Indian Ocean) $CaCO_3$ flux (Peterson et al., 1990) **d** site 1088 (Atlantic sector of Southern Ocean) $CaCO_3$ flux (Diester-Haass et al., 2005) **e** site U1541 (Pacific sector of Southern Ocean) $CaCO_3$ flux (this study). Blue and yellow vertical bar are the LMC and LMCIS events, respectively.

doi:10.6342/NTU202301546

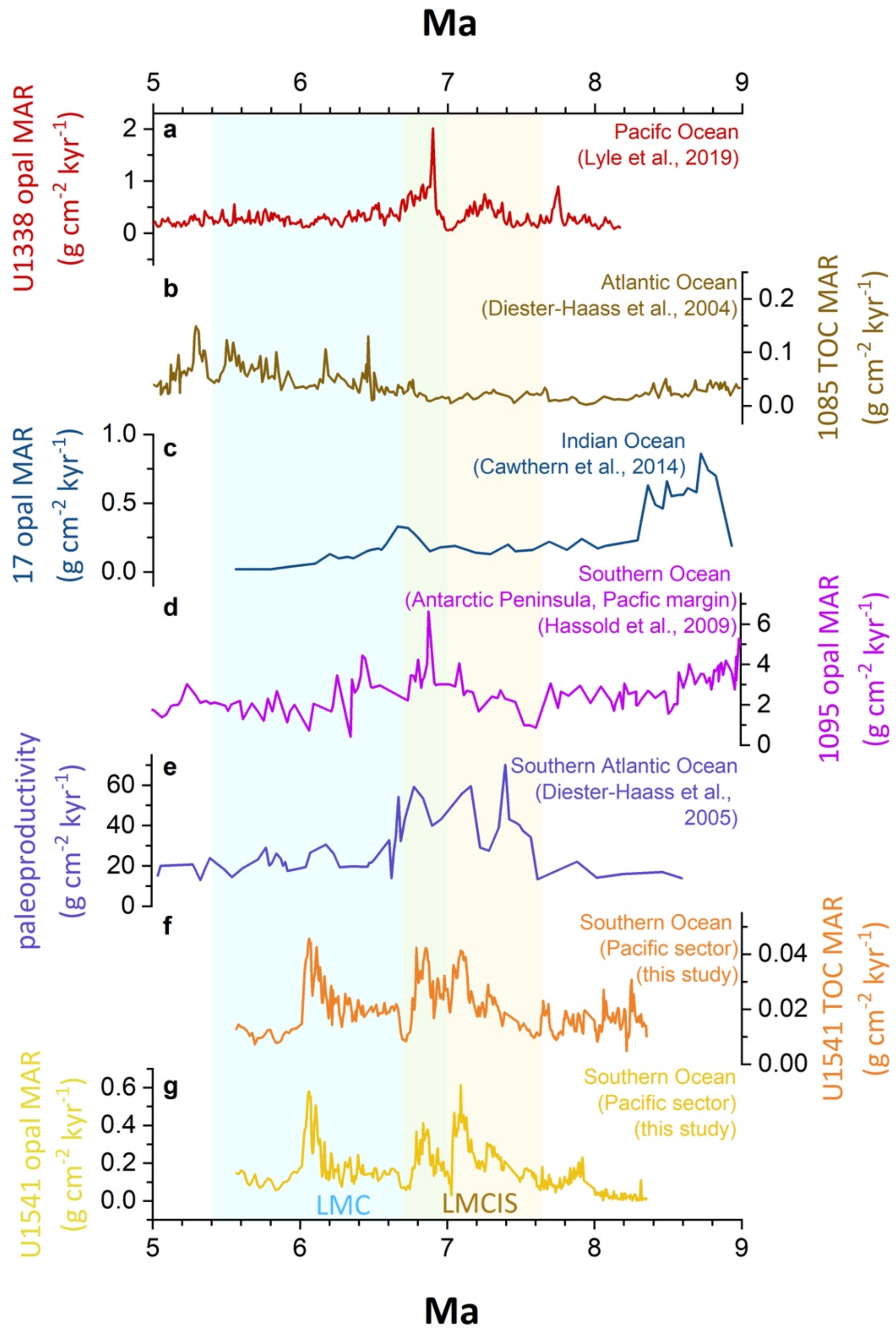

Fig. 5.12 Global TOC & opal fluxes. **a** site 1338 (Pacific Ocean) opal flux (Lyle et al., 2019) **b** site 1805 (Atlantic Ocean) TOC flux (Diester-Haass et al., 2004) **c** site 17 (Indian Ocean) opal flux (Cawthern et al., 2014) **d** site 1095 (Pacific margin of the Antarctic Peninsula) opal flux (Hassold et al., 2009) **e** site 1088 (Atlantic sector of Southern Ocean) paleoproductivity flux (Diester-Haass et al., 2005) **f** site U1541 (Pacific sector of

doi:10.6342/NTU202301546

Southern Ocean) TOC flux (this study) **g** site U1541 (Pacific sector of Southern Ocean) opal flux (this study). Blue and yellow vertical bar are the LMC and LMCIS events, respectively.

doi:10.6342/NTU202301546

6 Conclusions

We reconstruct the biogenic productivity using the sedimentary $CaCO_3$ and biogenic opal content in the central and eastern Pacific sector of Southern Ocean. Our results show that the burial fluxes in Southern Ocean are mainly controlled by productivity, instead of preservation. We also suggest that the expansion of the ACC have significant influence on the Southern Ocean productivity, and have strong correlation with the LMC event.

The different production rate at two sites may be the result of the upwelling strength and spatial differences. Site U1543 has higher siliceous production and significantly lower calcareous productivity, as this site is located in stronger upwelling area and also has higher dust input from land, thus increase the nutrient for photosynthesis by mainly siliceous organisms.

We suggest that the driving mechanism of LMCIS is related to the increasing ocean productivity. However, the uplifting and territorial C_4 expansion during the late Miocene may also lead to an increase in ocean productivity. The combination of terrestrial processes and the global ocean biogenic bloom may eventually drive the LMCIS as it can cause negative shifts in both planktonic and benthic foraminiferal $\delta^{13}C$.

doi:10.6342/NTU202301546

We compared the $CaCO_3$, TOC and opal content in different oceans during the late Miocene. There is less correlation between the sites in and outside the ACC. This may imply that the productivity variations in Southern Ocean are mainly controlled by the ACC, thus productivity proxies in different sectors of the ACC show similar patterns. In this study, we provide the Southern Ocean productivity record during the late Miocene and examine the relationship between Southern Ocean productivity, the LMC and LMCIS events, but further research is required to improve our understanding of the mechanisms during this period of time. For example, fragmentation and aeolian dust may imply the transportation processes, while Zr/Rb ratios in the ITRAX profiles can indicate the strength of the ACC.

doi:10.6342/NTU202301546

References

Akagi, T., Yasuda, S., Asahara, Y., Emoto, M., & Takahashi, K. (2014). Diatoms spread a high epsilon;Nd-signature in the North Pacific Ocean. *Geochemical Journal*. https://doi.org/10.2343/geochemj.2.0292

Anderson, J. R., Warny, S., Askin, R. A., Wellner, J. S., Bohaty, S. M., Kirshner, A. E., Livsey, D. N., Simms, A. R., Smith, T. C., Ehrmann, W., Lawver, L. A., Barbeau, D. L., Wise, S. W., Kulhenek, D. K., Weaver, F. A., & Majewski, W. (2011). Progressive Cenozoic cooling and the demise of Antarctica's last refugium. *Proceedings of the National Academy of Sciences*, *108*(28), 11356–11360. https://doi.org/10.1073/pnas.1014885108

Anderson, R. R., Ali, S., Bradtmiller, L. I., Nielsen, S. H., Fleisher, M., Anderson, B. J., & Burckle, L. H. (2009). Wind-driven upwelling in the Southern Ocean and the deglacial rise in atmospheric CO_2. *Science*, *323*(5920), 1443–1448. https://doi.org/10.1126/science.1167441

Barker, P. B., Filippelli, G. M., Florindo, F., Martin, E. E., & Scher, H. I. (2007). Onset and role of the Antarctic Circumpolar Current. *Deep-sea Research Part Ii-topical*

doi:10.6342/NTU202301546

Studies in Oceanography, *54*(21–22), 2388–2398. https://doi.org/10.1016/j.dsr2.2007.07.028

Barker, P., & Burrell, J. R. (1977). The opening of Drake Passage. *Marine Geology*, *25*(1–3), 15–34. https://doi.org/10.1016/0025-3227(77)90045-7

Barker, P., & Thomas, E. (2004). Origin, signature and palaeoclimatic influence of the Antarctic Circumpolar Current. *Earth-Science Reviews*, *66*(1–2), 143–162. https://doi.org/10.1016/j.earscirev.2003.10.003

Behrens, E., & Bostock, H. (2023). The response of the Subtropical Front to changes in the Southern Hemisphere westerly winds—Evidence from models and observations. *Journal of Geophysical Research: Oceans*, 128, e2022JC019139. https://doi.org/10.1029/2022JC019139

Benz, V., Esper, O., Gersonde, R., Lamy, F., & Tiedemann, R. (2016). Last Glacial Maximum sea surface temperature and sea-ice extent in the Pacific sector of the Southern Ocean. *Quaternary Science Reviews*, *146*, 216-237. https://doi.org/10.1016/j.quascirev.2016.06.006

doi:10.6342/NTU202301546

Bickert, T., Haug, G. H., & Tiedemann, R. (2004). Late Neogene benthic stable isotope record of Ocean Drilling Program Site 999: Implications for Caribbean paleoceanography, organic carbon burial, and the Messinian Salinity Crisis. *Paleoceanography*, *19*(1), PA1023. https://doi.org/10.1029/2002pa000799

Bradtmiller, L. I., Anderson, R. R., Fleisher, M., & Burckle, L. H. (2007). Opal burial in the equatorial Atlantic Ocean over the last 30 ka: Implications for glacial-interglacial changes in the ocean silicon cycle. *Paleoceanography*, *22*(4). https://doi.org/10.1029/2007pa001443

Budyko, M. I. (1969). The effect of solar radiation variations on the climate of the Earth. *Tellus B: Chemical and Physical Meteorology*, *21*(5), 611–619. https://doi.org/10.1111/j.2153-3490.1969.tb00466.x

Cawthern, T., Johnson, J. T., Giosan, L., Flores, J., Rose, K., & Solomon, E. A. (2014). A late Miocene–Early Pliocene biogenic silica crash in the Andaman Sea and Bay of Bengal. *Marine and Petroleum Geology*, *58*, 490–501. https://doi.org/10.1016/j.marpetgeo.2014.07.026

doi:10.6342/NTU202301546

Cerling, T. E., Harris, J., MacFadden, B. J., Leakey, M. G., Quade, J., Eisenmann, V., & Ehleringer, J. R. (1997). Global vegetation change through the Miocene/Pliocene boundary. *Nature*, *389*(6647), 153–158. https://doi.org/10.1038/38229

Chaigneau, A., & Pizarro, O. (2005). Surface circulation and fronts of the South Pacific Ocean, east of 120°W. *Geophysical Research Letters*, *32*(8). https://doi.org/10.1029/2004gl022070

Chase, Z., Anderson, R. H., Fleisher, M., & Kubik, P. W. (2003). Accumulation of biogenic and lithogenic material in the Pacific sector of the Southern Ocean during the past 40,000 years. *Deep sea Research Part II: Topical Studies in Oceanography*, *50*(3–4), 799–832. https://doi.org/10.1016/s0967-0645(02)00595-7

Chisholm, J. D., & Gattuso, J. (1991). Validation of the alkalinity anomaly technique for investigating calcification of photosynthesis in coral reef communities. *Limnology and Oceanography*, *36*(6), 1232–1239. https://doi.org/10.4319/lo.1991.36.6.1232

doi:10.6342/NTU202301546

Clarke, A., Murphy, E. J., Meredith, M. P., King, J. R., Peck, L. S., Barnes, D., & Smith, R. F. (2006). Climate change and the marine ecosystem of the western Antarctic Peninsula. *Philosophical Transactions of the Royal Society B*, *362*(1477), 149–166. https://doi.org/10.1098/rstb.2006.1958

Cortese, G., Gersonde, R., Hillenbrand, C., & Kuhn, G. (2004). Opal sedimentation shifts in the World Ocean over the last 15 Myr. *Earth and Planetary Science Letters*, *224*(3–4), 509–527. https://doi.org/10.1016/j.epsl.2004.05.035

De Baar, H. J. W., De Jong, J. T. M., Bakker, D. C. E., Löscher, B. M., Veth, C., Bathmann, U., & Smetacek, V. (1995). Importance of iron for plankton blooms and carbon dioxide drawdown in the Southern Ocean. *Nature*, *373*(6513), 412–415. https://doi.org/10.1038/373412a0

De La Rocha, C. L., & Passow, U. (2014). The Biological Pump. In *Elsevier eBooks* (pp. 93–122). Elsevier BV. https://doi.org/10.1016/b978-0-08-095975-7.00604-5

doi:10.6342/NTU202301546

DeMaster, D. J. (1981). The supply and accumulation of silica in the marine environment. *Geochimica et Cosmochimica Acta*, *45*(10), 1715–1732. https://doi.org/10.1016/0016-7037(81)90006-5

Diester-Haass, L., Billups, K., & Emeis, K. (2005). In search of the late Miocene-early Pliocene "biogenic bloom" in the Atlantic Ocean (Ocean Drilling Program Sites 982, 925, and 1088). *Paleoceanography*, *20*(4), n/a. https://doi.org/10.1029/2005pa001139

Diester-Haass, L., Meyers, P. A., & Bickert, T. (2004). Carbonate crash and biogenic bloom in the late Miocene: Evidence from ODP Sites 1085, 1086, and 1087 in the Cape Basin, southeast Atlantic Ocean. *Paleoceanography*, *19*(1), n/a. https://doi.org/10.1029/2003pa000933

Drury, A. J., Lee, G., Gray, W. A., Lyle, M. W., Westerhold, T., Shevenell, A. E., & John, C. M. (2018). Deciphering the State of the Late Miocene to Early Pliocene Equatorial Pacific. *Paleoceanography and Paleoclimatology*, *33*(3), 246–263. https://doi.org/10.1002/2017pa003245

doi:10.6342/NTU202301546

Drury, A. J., Liebrand, D., Westerhold, T., Beddow, H. M., Hodell, D. A., Rohlfs, N., Wilkens, R. H., Lyle, M. W., Bell, D., Kroon, D., Pälike, H., & Lourens, L. J. (2021). Climate, cryosphere and carbon cycle controls on Southeast Atlantic orbital-scale carbonate deposition since the Oligocene (30–0 Ma). *Climate of the Past*, *17*(5), 2091–2117. https://doi.org/10.5194/cp-17-2091-2021

Du, J., Tian, J., & Ma, W. (2022). The Late Miocene Carbon Isotope Shift driven by synergetic terrestrial processes: A box-model study. *Earth and Planetary Science Letters*, *584*, 117457. https://doi.org/10.1016/j.epsl.2022.117457

Duggen, S., Croot, P., Schacht, U., & Hoffmann, L. (2007). Subduction zone volcanic ash can fertilize the surface ocean and stimulate phytoplankton growth: Evidence from biogeochemical experiments and satellite data. *Geophysical Research Letters*, *34*(1). https://doi.org/10.1029/2006gl027522

Eagles, G. (2006). Deviations from an ideal thermal subsidence surface in the southern Pacific Ocean. *Terra Antartica Reports*, *12*, 109–118.

doi:10.6342/NTU202301546

Edmond, J. M. (1974). On the dissolution of carbonate and silicate in the deep ocean. *Deep Sea Research and Oceanographic Abstracts*, *21*(6), 455–480. https://doi.org/10.1016/0011-7471(74)90094-1

Encinas, A., Finger, K. L., Nielsen, S. N., Lavenu, A., Buatois, L. A., Peterson, D. T., & Roux, J. P. L. (2008). Rapid and major coastal subsidence during the late Miocene in south-central Chile. *Journal of South American Earth Sciences*, *25*(2), 157–175. https://doi.org/10.1016/j.jsames.2007.07.001

Fierro-Arcos, D., Corney, S., Meyer, A., Hayashida, H., Kiss, A. E., & Heil, P. (2023). Analysis of ecologically relevant sea ice and ocean variables for the Southern Ocean using a high-resolution model to inform ecosystem studies. *Progress in Oceanography*, *215*, 103049. https://doi.org/10.1016/j.pocean.2023.103049

Frankignoulle, M., Pichon, M., & Gattuso, J. (1995). Aquatic Calcification as a Source of Carbon Dioxide. In *Carbon Sequestration in the Biosphere*. https://doi.org/10.1007/978-3-642-79943-3_18

doi:10.6342/NTU202301546

Gasson, E., DeConto, R. M., Pollard, D., & Levy, R. H. (2016). Dynamic Antarctic ice sheet during the early to mid-Miocene. *Proceedings of the National Academy of Sciences of the United States of America*, *113*(13), 3459–3464. https://doi.org/10.1073/pnas.1516130113

Hanson, H. C. (1962). *Dictionary of Ecology*. Philosophical Library.

Hassold, N. J. C., Rea, D. K., Van Der Pluijm, B. A., & Parés, J. M. (2009). A physical record of the Antarctic Circumpolar Current: Late Miocene to recent slowing of abyssal circulation. *Palaeogeography, Palaeoclimatology, Palaeoecology*, *275*(1–4), 28–36. https://doi.org/10.1016/j.palaeo.2009.01.011

Herbert, T. D., Lawrence, K. T., Tzanova, A., Peterson, L. C., Caballero-Gill, R. P., & Kelly, C. B. (2016). Late Miocene global cooling and the rise of modern ecosystems. *Nature Geoscience*, *9*(11), 843–847. https://doi.org/10.1038/ngeo2813

Holbourn, A., Kuhnt, W., Clemens, S. C., Kochhann, K. G. D., Jöhnck, J., Lübbers, J., & Andersen, N. (2018). Late Miocene climate cooling and intensification of

doi:10.6342/NTU202301546

southeast Asian winter monsoon. *Nature Communications*, *9*(1). https://doi.org/10.1038/s41467-018-03950-1

Howard, W. R., & Prell, W. L. (1994). Late Quaternary $CaCO_3$ production and preservation in the Southern Ocean: Implications for oceanic and atmospheric carbon cycling. *Paleoceanography*, *9*(3), 453–482. https://doi.org/10.1029/93pa03524

Hutchins, D. A., & Fu, F. (2017). Microorganisms and ocean global change. *Nature Microbiology*, *2*(6). https://doi.org/10.1038/nmicrobiol.2017.58

Iglesias-Rodriguez, M. D., Brown, C., Doney, S. C., Kleypas, J. A., Kolber, D. D., Kolber, Z., Hayes, P. D., & Falkowski, P. G. (2002). Representing key phytoplankton functional groups in ocean carbon cycle models: Coccolithophorids. *Global Biogeochemical Cycles*, *16*(4), 47–20. https://doi.org/10.1029/2001gb001454

Jaccard, S. L., Hayes, C. J., Martínez-García, A., Hodell, D. A., Anderson, R. H., Sigman, D. M., & Haug, G. H. (2013). Two Modes of Change in Southern Ocean

doi:10.6342/NTU202301546

Productivity Over the Past Million Years. *Science*, *339*(6126), 1419–1423. https://doi.org/10.1126/science.1227545

Kalokora, O. J., Buriyo, A., Asplund, M., Gullström, M., Mtolera, M. S. P., & Björk, M. (2020). An experimental assessment of algal calcification as a potential source of atmospheric CO_2. *PLOS ONE*, *15*(4), e0231971. https://doi.org/10.1371/journal.pone.0231971

Keigwin, L. D. (1979). Late Cenozoic stable isotope stratigraphy and paleoceanography of DSDP sites from the east equatorial and central north Pacific Ocean. *Earth and Planetary Science Letters*, *45*(2), 361–382. https://doi.org/10.1016/0012-821x(79)90137-7

Kohfeld, K. E., Quéré, C. L., Harrison, S. P., & Anderson, R. H. (2005). Role of Marine Biology in Glacial-Interglacial CO_2 Cycles. *Science*, *308*(5718), 74–78. https://doi.org/10.1126/science.1105375

doi:10.6342/NTU202301546

Kuczyńska, P., Jemioła-Rzemińska, M., & Strzałka, K. (2015). Photosynthetic Pigments in Diatoms. *Marine Drugs*, *13*(9), 5847–5881. https://doi.org/10.3390/md13095847

Kump, L. R., Brantley, S. L., & Arthur, M. A. (2000). Chemical Weathering, Atmospheric CO_2, and Climate. *Annual Review of Earth and Planetary Sciences*, *28*(1), 611–667. https://doi.org/10.1146/annurev.earth.28.1.611

Lamy, F., Winckler, G., & Alvarez-Zarikian, C. A. (2021). Volume 383: Dynamics of the Pacific Antarctic Circumpolar Current (DYNAPACC). *Proceedings of the International Ocean Discovery Program*. https://doi.org/10.14379/iodp.proc.383.2021

Leutert, T. J., Auderset, A., Martínez-García, A., Modestou, S., & Meckler, A. N. (2020). Coupled Southern Ocean cooling and Antarctic ice sheet expansion during the middle Miocene. *Nature Geoscience*, *13*(9), 634–639. https://doi.org/10.1038/s41561-020-0623-0

doi:10.6342/NTU202301546

Li, G., Cheng, L., Zhu, J., Trenberth, K. E., Mann, M. E., & Abraham, J. (2020). Increasing ocean stratification over the past half-century. *Nature Climate Change*, *10*(12), 1116–1123. https://doi.org/10.1038/s41558-020-00918-2

Li, J., Fang, X., Song, C., Pan, B., Ma, Y., & Yan, M. (2014). Late Miocene–Quaternary rapid stepwise uplift of the NE Tibetan Plateau and its effects on climatic and environmental changes. *Quaternary Research*, *81*(3), 400–423. https://doi.org/10.1016/j.yqres.2014.01.002

Lyle, M. W. (2003). Neogene carbonate burial in the Pacific Ocean. *Paleoceanography*, *18*(3). https://doi.org/10.1029/2002pa000777

Lyle, M. W., Drury, A. J., Tian, J., Wilkens, R. H., & Westerhold, T. (2019). Late Miocene to Holocene high-resolution eastern equatorial Pacific carbonate records: stratigraphy linked by dissolution and paleoproductivity. *Climate of the Past*, *15*(5), 1715–1739. https://doi.org/10.5194/cp-15-1715-2019

Lyle, M. W., Murray, D. W., Finney, B. P., Dymond, J., Robbins, J. M., & Brooksforce, K. (1988). The record of Late Pleistocene biogenic sedimentation in the eastern

doi:10.6342/NTU202301546

tropical Pacific Ocean. *Paleoceanography*, *3*(1), 39–59. https://doi.org/10.1029/pa003i001p00039

Martin, J., Gordon, R. D., Fitzwater, S. E., & Broenkow, W. W. (1989). Vertex: phytoplankton/iron studies in the Gulf of Alaska. *Deep sea Research Part A*: Oceanographic Research Papers, *36*(5), 649–680. https://doi.org/10.1016/0198-0149(89)90144-1

Martínez-García, A., Rosell-Melé, A., Jaccard, S. L., Geibert, W., Sigman, D. M., & Haug, G. H. (2011). Southern Ocean dust–climate coupling over the past four million years. *Nature*, *476*(7360), 312–315. https://doi.org/10.1038/nature10310

Mortlock, R. A., & Froelich, P. N. (1989). A simple method for the rapid determination of biogenic opal in pelagic marine sediments. *Deep-sea Research*, *36*(9), 1415–1426. https://doi.org/10.1016/0198-0149(89)90092-7

Murray, R. M., Leinen, M., & Knowlton, C. B. (2012). Links between iron input and opal deposition in the Pleistocene equatorial Pacific Ocean. *Nature Geoscience*, *5*(4), 270–274. https://doi.org/10.1038/ngeo1422

doi:10.6342/NTU202301546

Paytan, A. (2009). Ocean Paleoproductivity. In *Encyclopedia of earth sciences* (pp. 644–651). Springer Nature (Netherlands). https://doi.org/10.1007/978-1-4020-4411-3_158

Peterson, L. E., & Backman, J. (1990). Late Cenozoic Carbonate Accumulation and the History of the Carbonate Compensation Depth in the Western Equatorial Indian Ocean. In *Proceedings of the Ocean Drilling Program*. https://doi.org/10.2973/odp.proc.sr.115.163.1990

Pfiffner, O. A., & Gonzalez, L. M. (2013). Mesozoic–Cenozoic Evolution of the Western Margin of South America: Case Study of the Peruvian Andes. *Geosciences*, *3*(2), 262–310. https://doi.org/10.3390/geosciences3020262

Pillot, Q., Suchéras-Marx, B., Sarr, A., Bolton, C. T., & Donnadieu, Y. (2023). A Global Reassessment of the Spatial and Temporal Expression of the Late Miocene Biogenic Bloom. *Paleoceanography and Paleoclimatology*, *38*(3). https://doi.org/10.1029/2022pa004564

doi:10.6342/NTU202301546

Plank, T., & Manning, C. E. (2019). Subducting carbon. *Nature*, *574*(7778), 343–352. https://doi.org/10.1038/s41586-019-1643-z

Quade, J., Cerling, T. E., & Bowman, J. L. (1989). Development of Asian monsoon revealed by marked ecological shift during the latest Miocene in northern Pakistan. *Nature*, *342*(6246), 163–166. https://doi.org/10.1038/342163a0

Ramaswamy, V., & Gaye, B. (2006). Regional variations in the fluxes of foraminifera carbonate, coccolithophorid carbonate and biogenic opal in the northern Indian Ocean. *Deep sea Research Part I: Oceanographic Research Papers*, *53*(2), 271–293. https://doi.org/10.1016/j.dsr.2005.11.003

Schoepfer, S. D., Shen, J., Wei, H., Tyson, R. V., Ingall, E. D., & Algeo, T. J. (2015). Total organic carbon, organic phosphorus, and biogenic barium fluxes as proxies for paleomarine productivity. *Earth-Science Reviews*, *149*, 23–52. https://doi.org/10.1016/j.earscirev.2014.08.017

Scotese, C. R. (2016). Some thoughts on Global Climate Change: The Transition from Icehouse to Hothouse. *Earth History: The Evolution of the Earth System*.

doi:10.6342/NTU202301546

Sigman, D. M., & Hain, M. P. (2012a). The biological productivity of the ocean: Section 2. *Nature Education Knowledge*, *3*(10), 20.

Sigman, D. M., & Hain, M. P. (2012b). The biological productivity of the ocean. *Nature Education Knowledge*, *3*(10), 21.

Sigman, D. M., Hain, M. P., & Haug, G. H. (2010). The polar ocean and glacial cycles in atmospheric CO_2 concentration. *Nature*, *466*(7302), 47–55. https://doi.org/10.1038/nature09149

Singh, H. A., & Polvani, L. M. (2020). Low Antarctic continental climate sensitivity due to high ice sheet orography. *npj Climate and Atmospheric Science*, *3*(1). https://doi.org/10.1038/s41612-020-00143-w

Steinthorsdottir, M., Coxall, H. K., De Boer, A. M., Huber, M., Barbolini, N., Bradshaw, C. D., Burls, N. J., Feakins, S. J., Gasson, E., Henderiks, J., Holbourn, A. E., Kiel, S., Kohn, M. J., Knorr, G., Kürschner, W. M., Lear, C. H., Liebrand, D., Lunt, D. J., Mörs, T., Pearson, P.N., Pound, M.J., Stoll, H., Strömberg, C. A. E. (2021).

doi:10.6342/NTU202301546

The Miocene: The Future of the Past. *Paleoceanography and Paleoclimatolog*, *36*(4). https://doi.org/10.1029/2020pa004037

Toggweiler, J. R., & Russell, J. L. (2008). Ocean circulation in a warming climate. *Nature*, *451*(7176), 286–288. https://doi.org/10.1038/nature06590

Toyos, M. H., Lamy, F., Lange, C. B., Lembke-Jene, L., Saavedra-Pellitero, M., Esper, O., & Arz, H. W. (2020). Antarctic Circumpolar Current Dynamics at the Pacific Entrance to the Drake Passage Over the Past 1.3 Million Years. *Paleoceanography and Paleoclimatology*, *35*(7). https://doi.org/10.1029/2019pa003773

Tréguer, P. (2014). The Southern Ocean silica cycle. *Comptes Rendus Geoscience*, *346*(11–12), 279–286. https://doi.org/10.1016/j.crte.2014.07.003

Van Cappellen, P., Dixit, S., & Van Beusekom, J. (2002). Biogenic silica dissolution in the oceans: Reconciling experimental and field-based dissolution rates. *Global Biogeochemical Cycles*, *16*(4), 23–10. https://doi.org/10.1029/2001gb001431

doi:10.6342/NTU202301546

Vergara-Jara, M. J., Hopwood, M. J., Browning, T. J., Rapp, I., Torres, R., Reid, B. J., Achterberg, E. P., & Iriarte, J. (2021). A mosaic of phytoplankton responses across Patagonia, the southeast Pacific and the southwest Atlantic to ash deposition and trace metal release from the Calbuco volcanic eruption in 2015. *Ocean Science*, *17*(2), 561–578. https://doi.org/10.5194/os-17-561-2021

Volk, T., & Hoffert, M. I. (1985). Ocean Carbon Pumps: Analysis of Relative Strengths and Efficiencies in Ocean-Driven Atmospheric CO_2 Changes. In *American Geophysical Union eBooks* (pp. 99–110). American Geophysical Union. https://doi.org/10.1029/gm032p0099

Wang, N., Wen, L., Li, M., Dai, X., Xu, Y. G., Ming, Y., & Liu, J. (2021). The origin of abnormally ^{13}C-depleted organic carbon isotope signatures in the early Cambrian Yangtze Platform. *Marine and Petroleum Geology*, *128*, 105051. https://doi.org/10.1016/j.marpetgeo.2021.105051

Ware, J. E., Smith, S. M., & Reaka-Kudla, M. L. (1992). Coral reefs: sources or sinks of atmospheric CO_2? *Coral Reefs*, *11*(3), 127–130. https://doi.org/10.1007/bf00255465

doi:10.6342/NTU202301546

Webb, P. (2021). *Introduction to Oceanography*. Roger Williams University.

Wei, Y., Zhao, Y., Gui, J., & Sun, J. (2021). Phosphorus enrichment masked the negative effects of ocean acidification on picophytoplankton and photosynthetic performance in the oligotrophic Indian Ocean. *Ecological Indicators*, *125*, 107459. https://doi.org/10.1016/j.ecolind.2021.107459

Well, R., & Roether, W. (2003). Neon distribution in South Atlantic and South Pacific waters. *Deep-sea Research Part I: Oceanographic Research Papers*, 50(6), 721-735. https://doi.org/10.1016/s0967-0637(03)00058-x

Westerhold, T., Marwan, N., Drury, A. J., Liebrand, D., Agnini, C., Anagnostou, E. N., Barnet, J. S. K., Bohaty, S. M., De Vleeschouwer, D., Florindo, F., Frederichs, T., Hodell, D. A., Holbourn, A., Kroon, D., Lauretano, V., Littler, K., Lourens, L. J., Lyle, M. W., Pälike, H., Röhl, U., Tian, J., Wilkens, R.H., Wilson, P.A., Zachos, J. C. (2020). An astronomically dated record of Earth's climate and its predictability over the last 66 million years. *Science*, *369*(6509), 1383–1387. https://doi.org/10.1126/science.aba6853

doi:10.6342/NTU202301546

Yao, Z., Liu, Y., Shi, X., Gong, X., Gorbarenko, S. A., Bosin, A., Gao, J., Bai, Y., Zhang, H., & Wang, A. (2022). Paleoproductivity variations and implications in the subarctic northwestern Pacific since MIS 7: Geochemical evidence. *Global and Planetary Change*, *209*, 103730. https://doi.org/10.1016/j.gloplacha.2021.103730

doi:10.6342/NTU202301546

Appendix

Table 1. Site U1541 biostratigraphic constraints (5.6-8.4 Ma). (Lamy et al., 2021, https://doi.org/10.14379/iodp.proc.383.105.2021)
Event type: D = diatom datum, R = radiolarian datum, N = calcareous nannofossil datum, F = planktonic foraminifer datum. FO = first occurrence, FCO = first common occurrence, LO = last occurrence, LCO = last common occurrence, LAO = last abundant occurrence. * = datums applied with lower confidence based on preservation, age, or depth uncertainty. References: AO = Anthonissen and Ogg (2012), B = Bohaty et al. (1998), B04 = Bylinskaya (2004), C = Cody et al. (2008) average range model, CG = Censarek and Gersonde (2002), CP = Chaisson and Pearson (1997), G = Gersonde (1989), HM = Harwood and Maruyama (1992), KS = Kennet and Srinivasan (1983), L = Lazarus (1992), O = Ogg (2012), S07 = Scott et al. (2007), S = Sjunneskog et al. (2012), T = Tauxe et al. (2012), W = Winter et al., 2012, W94 = Wei (1994), W11 = Wade et al. (2011), ZG = Zielinski and Gersonde (2002), 181 = ODP Leg 181 Initial Reports (2000), 374 = IODP Exp. 374 diatom and radiolarian biostratigraphic frameworks (David Harwood and Giuseppe Cortese, pers. comm.)

Type	Bioevent	Age (Ma)	Top core, section, interval (cm)	Top depth CSF-A (m)	Bottom core, section, interval (cm)	Bottom depth CSF-A (m)	Reference
			383-U1541B-		**383-U1541B-**		
F	*FO Globoconella puncticulata*	4.37-5.72	10H-CC, 0-6	91.41-91.47	11H-CC, 29-35	102.03-102.09	W94
F	*LO Hirsutella juanai*	5.2-5.72	10H-CC, 0-6	91.41-91.47	11H-CC, 29-35	102.03-102.09	CP, W11
F	*LO Hirsutella margaritae*	3.85	10H-CC, 0-6	91.41-91.47	11H-CC, 29-35	102.03-102.09	AO
F	*FO Truncorotalia crassaformis*	4.5	10H-CC, 0-6	91.41-91.47	11H-CC, 29-35	102.03-102.09	AO

doi:10.6342/NTU202301546

Type	Bioevent	Age (Ma)	Top core, section, interval (cm)	Top depth CSF-A (m)	Bottom core, section, interval (cm)	Bottom depth CSF-A (m)	Reference
D	*LO Actinocyclus ingens var. ovalis*	4.75-6.81	10H-CC, 0-6	91.41-91.47	11H-1, 80	93.4	C
R	*LO Amphymenium challengerae*	6.22	11H-CC, 29-35	102.03-102.09	12H-CC, 10-16	111.54-111.60	L, 374
F	*LO Globoconella conomiozea*	5.72-6.14	11H-CC, 29-35	102.03-102.09	12H-CC, 10-16	111.54-111.60	W94
D	*LO Hemidiscus triangularis*	5.13-5.4	11H-CC, 29-35	102.03-102.09	12H-1, 50	102.6	CG, 374
D	*LO Thalassiosira convexa var. aspinosa*	5.19-6.64	11H-CC, 29-35	102.03-102.09	12H-1, 50	102.6	C, CG
D	*LO Denticulopsis hustedtii*	5.6-6.3	12H-6, 50	110.12	12H-CC, 10-16	111.54-111.60	HM
R	*FO Amphymenium challengerae*	6.84	12H-CC, 10-16	111.54-111.60	13H-CC, 25-31	120.55-120.61	L,374
F	*LO Globorotalia miotumida*	6.14-8.58	12H-CC, 10-16	111.54-111.60	13H-CC, 25-31	120.55-120.61	W94,KS
D	*LO Actinocyclus ellipticus*	5.14-7.78	13H-1, 50	112.1	13H-3, 50	115.12	C
R	*FO Acrosphaera? labrata*	7.84	13H-CC, 25-31	120.55-120.61	14H-CC, 0-6	129.85-129.91	L,374
D	*FO Hemidiscus triangularis*	6.14-7.3	14H-1, 50	121.6	14H-3, 50	124.55	C, CG
D	*FO Fragilariopsis reinholdii*	7.96-8.5	14H-5, 50	127.51	14H-CC, 0-6	129.85-129.91	CG, 374
D	*FO Fragilariopsis cylindrica**	7.7	14H-CC, 0-6	129.85-129.91	15H-1, 50	131.1	374

doi:10.6342/NTU202301546

Type	Bioevent	Age (Ma)	Top core, section, interval (cm)	Top depth CSF-A (m)	Bottom core, section, interval (cm)	Bottom depth CSF-A (m)	Reference
D	*FO Fragilariopsis fossilis**	8.37-8.7	15H-1, 50	131.1	15H-CC, 0-7	137.98-138.04	C, 374
			383-U1541C-		**383-U1541C-**		
D	*LO Actinocyclus ingens var. ovalis*	4.75-6.81	10H-6, 110-111	87.43-87.44	11H-1, 20-21	89.80-89.81	C
D	*LO Fragilariopsis clementia*	4.51-4.6	11H-1, 20-21	89.80-89.81	11H-3, 20-21	92.80-92.81	C, 374
			Constrained in Hole U1541B only				AO
D	*LO Thalassiosira convexa var. aspinosa*	5.19-6.64	11H-5, 20-21	95.78-95.79	12H-1, 70-71	99.80-99.81	C, CG
D	*FO Fragilariopsis clementia**	6.35-7.7	11H-5, 20-21	95.78-95.79	12H-1, 70-71	99.80-99.81	C
D	*FO Fragilariopsis cylindrica**	7.7	13H-1, 50-51	109.10-109.11	13H-2, 90-91	111.00-111.01	374

doi:10.6342/NTU202301546

Table 2. Site U1543 biostratigraphic constraints (5.2-7.3 Ma). (Lamy et al., 2021, https://doi.org/10.14379/iodp.proc.383.107.2021)

Event type: D = diatom datum, R = radiolarian datum, N = calcareous nannofossil datum, F = planktonic foraminifer datum. FO = first occurrence, FCO = first common occurrence, LO = last occurrence, LCO = last common occurrence, LAO = last abundant occurrence. * = datums applied with lower confidence based on preservation, age, or depth uncertainty. References: AO = Anthonissen and Ogg (2012), B = Bohaty et al. (1998), B04 = Bylinskaya (2004), C = Cody et al. (2008) average range model, CG = Censarek and Gersonde (2002), CP = Chaisson and Pearson (1997), G = Gersonde (1989), HM = Harwood and Maruyama (1992), KS = Kennet and Srinivasan (1983), L = Lazarus (1992), O = Ogg (2012), S07 = Scott et al. (2007), S = Sjunneskog et al. (2012), T = Tauxe et al. (2012), W = Winter et al., 2012, W94 = Wei (1994), W11 = Wade et al. (2011), ZG = Zielinski and Gersonde (2002), 181 = ODP Leg 181 Initial Reports (2000), 374 = IODP Exp. 374 diatom and radiolarian biostratigraphic frameworks (David Harwood and Giuseppe Cortese, pers. comm.), 383 = regional datum age revised for IODP Exp. 383.

Type	Bioevent	Age (Ma)	Top core, section, interval (cm)	Top depth CSF-A (m)	Bottom core, section, interval (cm)	Bottom depth CSF-A (m)	Reference
			383-U1543A-		**383-U1543A-**		
D	*LO Thalassiosira convexa var. aspinosa**	5.19-6.64	26H-CC, 17-23	245.02-245.08	27H-CC, 17-23	254.62-254.68	C, CG
R	*LCO Lychnocanium grande*	5	27H-CC, 17-23	254.62-254.68	28H-CC, 13-19	264.00-264.06	L, 374
D	*FO Thalassiosira inura**	4.71-4.77	28H-CC, 13-19	264.00-264.06	29H-CC, 28-34	273.23-273.29	C
D	*LO Actinocyclus ingens var. ovalis*	4.75-6.81	28H-CC, 13-19	264.00-264.06	29H-CC, 28-34	273.23-273.29	C
D	*LO Hemidiscus triangularis*	5.13-5.4	29H-CC, 28-34	273.23-273.29	30H-CC, 19-25	283.04-283.10	CG, 374
R	*LO Amphymenium challengerae*	6.22	30H-CC, 19-25	283.04-283.10	31H-CC, 21-27	292.56-292.62	L, 374

doi:10.6342/NTU202301546

Type	Bioevent	Age (Ma)	Top core, section, interval (cm)	Top depth CSF-A (m)	Bottom core, section, interval (cm)	Bottom depth CSF-A (m)	Reference
R	*FO Amphymenium challengerae*	6.84	31H-CC, 21-27	292.56-292.62	32H-CC, 20-26	302.04-302.10	L, 374
R	*FO Acrosphaera? labrata*	7.84	34H-CC, 20-26	321.10-321.16	35H-CC, 21-27	330.57-330.63	L, 374
D	*FO Hemidiscus triangularis*	6.14-7.3	34H-CC, 20-26	321.10-321.16	35H-CC, 21-27	330.57-330.63	C, CG
D	*presence Fragilariopsis aurica**	< 8.3-8.4	36H-CC, 20-26	339.48-339.54	Maximum age at base of hole	-	C, 374

doi:10.6342/NTU202301546

Table 3. Site U1541 geomagnetic polarity chronology (5.6-8.4 Ma). (Lamy et al., 2021, https://doi.org/10.14379/iodp.proc.383.105.2021)
GTS2012 = geomagnetic timescale of Gradstein et al. (2012). t = top.

			Top				Bottom			
Polarity chron interpretation	**Subchron**	**Age (GTS 2012) (Ma)**	**Core, section**	**Depth CSF-A (m)**	**Depth (+/-m)**	**Depth CCSF-A (m)**	**Core, section**	**Depth CSF-A (m)**	**Depth (+/-m)**	**Depth CCSF-A (m)**
			383-U1541B-				**383-U1541C-**			
C3r	Gilbert	5.235	11H-4	99.35	0.75	104.16	11H-4			
C3An.1n		6.033					12H-4	104.35	0.75	108.68
C3An.1r		6.252	12H-3	105.85	0.75	112.12	12H-3	108.5	0.75	112.83
C3An.2n		6.436	12H-5	108.85	0.75	115.12	12H-5	109.35	0.75	114.5
C3Ar		6.733					13H-3	112.35	0.75	117.5
C3Bn		7.14	13H-4	116.85	0.75	123.8	13H-4			
C3Br.1r		7.212								
C3Br.1n		7.251	13H-5	118.35	0.75	125.3	13H-5			
C3Br.2r		7.285	13H-5	118.35	0.75	125.3	13H-5			
C3Br.2n		7.454								
C3Br.3r		7.489								
C4n.1n		7.528	14H-1	121.85	0.75	129.3	14H-1			
C4n.1r		7.642	14H-2	123.3	0.75	130.75	14H-2			
C4n.2n		7.695	14H-3	124.8	0.75	132.25	14H-3			
C4r.1r		8.108	15H-2	132.85	0.75	140.8	15H-2			
C4r.1n		8.254	15H-4	135.85	0.75	143.8	15H-4			

doi:10.6342/NTU202301546

Table 4. Site U1543 geomagnetic polarity chronology (5.2-7.3 Ma). (Lamy et al., 2021, https://doi.org/10.14379/iodp.proc.383.107.2021) GTS2012 = geomagnetic timescale of Gradstein et al. (2012). t = top.

Polarity chron boundary interpretation	Chron	Age (GTS 2012) (Ma)	Core, section	Top depth CSF-A (m)	Bottom depth CSF-A (m)	Core, section	Top depth CSF-A (m)	Bottom depth CSF-A (m)
			383-U1543A-			383-U1543B-		
C3n.4n	Thvera	4.997	27H-1	244.6	246.05	29H-4	243.25	244.66
C3r	Gilbert	5.235	28H-1	254.1	255.55	30H-4	252.76	254.19
C3An.1n		6.033	30H-7/31H-1	282.17	284.12	33H-4	282	283
C3An.1r		6.252	31H-6	290.15	291.66			
C3An.2n		6.436	32H-2	293.61	295.12			
C3Ar		6.733	32H-6/33H-1	299.65	303.14			
C3Bn		7.14	33H-6/34H-1	310.72	312.6			
C3Br.1r		7.212	34H-2 to 34H-3	312.6	315.62			
C3Br.1n		7.251	34H-3 to 34H-4	314.11	317.13			
C3Br.2r		7.285	34H-4 to 34H-5	315.62	318.63			

doi:10.6342/NTU202301546

Table 5. Standards for $CaCO_3$ and TOC analysis. Both standards are tested by the same method which is used to analyze the samples. The testing data are shown in Appendix Table 6. *Acidified grinded mudstone from Gutingkeng Formation.

	Standards	Part No.	Lot No.	Manufacturer	Reported/ expected TC (%)
Commercial	Leco soil standard	502-962	1000	LECO	0.717 (±0.027)
In-house	DGS TOC #1*	/	/	/	0.535 (±0.020)

Table 6. Testing EA data of Standards for $CaCO_3$ and TOC analysis.

Leco Soil standard					
Tested TC (%) average		0.721	Reported TC (%)		0.717
Standard deviation		0.015	+/-		0.027
No.	**Testing date**	**TC (%)**	**error (%)**	**TOC (%)**	**TIC (%)**
1	2021/10/14	0.721	0.031	0.710	0.011
2	2021/10/14	0.718	0.031	0.710	0.009
3	2021/10/14	0.695	0.030	0.688	0.007
4	2021/11/08	0.743	0.031	0.733	0.010
5	2021/11/08	0.721	0.031	0.710	0.011
6	2021/11/08	0.734	0.032	0.722	0.012
7	2021/11/08	0.714	0.031	0.704	0.010
8	2021/11/08	0.694	0.031	0.685	0.010
9	2021/11/08	0.723	0.031	0.714	0.009
10	2021/11/08	0.697	0.030	0.689	0.007

DGS OC #1					
Tested TC (%) average		0.544		average (%)	
Standard deviation		0.010		0.516	0.032
No.	**Testing date**	**TC (%)**	**error (%)**	**TOC (%)**	**TIC (%)**
1	2021/10/12	0.562	0.031	0.530	0.032
2	2021/10/12	0.551	0.031	0.520	0.031
3	2021/10/12	0.555	0.030	0.529	0.026
4	2021/10/18	0.551	0.031	0.521	0.030
5	2021/10/18	0.551	0.031	0.522	0.029
6	2021/10/18	0.542	0.029	0.517	0.025
7	2021/10/25	0.560	0.031	0.531	0.029
8	2021/10/25	0.553	0.031	0.526	0.027
9	2021/10/25	0.549	0.030	0.522	0.027
10	2021/10/25	0.547	0.030	0.518	0.029

doi:10.6342/NTU202301546

Leco Soil standard					
	Tested TC (%) average	0.721	Reported TC (%)		0.717
	Standard deviation	0.015		+/-	0.027
No.	**Testing date**	**TC (%)**	**error (%)**	**TOC (%)**	**TIC (%)**
11	2021/11/08	0.709	0.031	0.702	0.007
12	2021/11/08	0.726	0.031	0.717	0.010
13	2021/11/08	0.711	0.030	0.699	0.013
14	2021/11/08	0.697	0.031	0.689	0.007
15	2021/11/08	0.700	0.030	0.691	0.009
16	2021/11/08	0.698	0.029	0.692	0.006
17	2021/11/08	0.724	0.029	0.712	0.012
18	2021/11/08	0.704	0.032	0.696	0.008
19	2021/11/08	0.709	0.031	0.695	0.014
20	2021/11/08	0.697	0.031	0.691	0.006
21	2021/11/08	0.696	0.029	0.686	0.010
22	2021/12/24	0.738	0.010	0.728	0.042
23	2021/12/24	0.747	0.010	0.737	0.042
24	2021/12/24	0.734	0.010	0.725	0.043
25	2021/12/24	0.738	0.010	0.728	0.042
26	2021/12/24	0.753	0.011	0.742	0.042
27	2021/12/24	0.746	0.010	0.736	0.042

DGS OC #1					
	Tested TC (%) average	0.544		average (%)	
	Standard deviation	0.010		0.516	0.032
No.	**Testing date**	**TC (%)**	**error (%)**	**TOC (%)**	**TIC (%)**
11	2021/10/25	0.549	0.029	0.518	0.030
12	2021/10/25	0.546	0.029	0.517	0.029
13	2021/10/25	0.552	0.029	0.523	0.028
14	2021/10/25	0.547	0.029	0.521	0.026
15	2021/10/25	0.555	0.031	0.526	0.029
16	2021/10/25	0.554	0.032	0.526	0.028
17	2021/10/25	0.550	0.032	0.524	0.025
18	2021/10/25	0.544	0.030	0.519	0.025
19	2021/10/25	0.555	0.030	0.530	0.025
20	2021/10/25	0.562	0.032	0.533	0.028
21	2021/10/25	0.548	0.030	0.525	0.024
22	2021/11/09	0.557	0.031	0.527	0.030
23	2021/11/09	0.542	0.031	0.513	0.029
24	2021/11/09	0.539	0.031	0.514	0.025
25	2021/11/09	0.540	0.031	0.514	0.026
26	2021/11/09	0.541	0.031	0.515	0.027
27	2021/11/09	0.548	0.031	0.519	0.029

doi:10.6342/NTU202301546

Leco Soil standard					
	Tested TC (%) average	0.721		Reported TC (%)	0.717
	Standard deviation	0.015		+/-	0.027
No.	**Testing date**	**TC (%)**	**error (%)**	**TOC (%)**	**TIC (%)**
28	2021/12/24	0.752	0.009	0.743	0.043
29	2021/12/24	0.716	0.009	0.707	0.042
30	2021/12/24	0.710	0.009	0.701	0.042
31	2021/12/24	0.720	0.010	0.710	0.043
32	2021/12/24	0.716	0.010	0.706	0.042
33	2021/12/24	0.702	0.009	0.694	0.043
34	2021/12/24	0.730	0.010	0.720	0.042
35	2021/12/24	0.741	0.011	0.730	0.043
36	2021/12/24	0.724	0.011	0.712	0.043
37	2021/12/24	0.722	0.010	0.712	0.043
38	2021/12/24	0.728	0.009	0.719	0.043
39	2021/12/24	0.709	0.011	0.698	0.042
40	2021/12/24	0.738	0.009	0.729	0.043
41	2021/12/24	0.719	0.010	0.709	0.042
42	2022/01/07	0.717	0.010	0.706	0.042
43	2022/01/07	0.710	0.010	0.700	0.043
44	2022/01/07	0.707	0.010	0.697	0.041

DGS OC #1					
	Tested TC (%) average	0.544		average (%)	
	Standard deviation	0.010		0.516	0.032
No.	**Testing date**	**TC (%)**	**error (%)**	**TOC (%)**	**TIC (%)**
28	2021/11/09	0.530	0.031	0.505	0.025
29	2021/11/09	0.543	0.030	0.514	0.030
30	2021/11/09	0.541	0.031	0.511	0.030
31	2021/11/09	0.540	0.029	0.511	0.029
32	2021/11/09	0.537	0.030	0.510	0.027
33	2021/11/09	0.539	0.031	0.512	0.027
34	2021/11/17	0.536	0.030	0.510	0.026
35	2021/11/17	0.551	0.030	0.522	0.029
36	2021/11/17	0.567	0.032	0.535	0.032
37	2021/11/17	0.555	0.030	0.526	0.028
38	2021/11/17	0.544	0.029	0.517	0.027
39	2021/11/17	0.543	0.030	0.515	0.028
40	2021/11/17	0.550	0.031	0.523	0.027
41	2021/12/24	0.541	0.028	0.513	0.043
42	2021/12/24	0.538	0.026	0.512	0.042
43	2021/12/24	0.539	0.026	0.513	0.042
44	2021/12/24	0.533	0.027	0.505	0.043

doi:10.6342/NTU202301546

Leco Soil standard					
	Tested TC (%) average	0.721		Reported TC (%)	0.717
	Standard deviation	0.015		+/-	0.027
No.	**Testing date**	**TC (%)**	**error (%)**	**TOC (%)**	**TIC (%)**
45	2022/01/07	0.737	0.010	0.726	0.042
46	2022/01/07	0.701	0.009	0.691	0.042
47	2022/01/07	0.704	0.009	0.695	0.042
48	2022/01/07	0.739	0.009	0.730	0.042
49	2022/01/07	0.735	0.010	0.725	0.043
50	2022/01/07	0.734	0.008	0.725	0.043
51	2022/01/07	0.740	0.013	0.727	0.043
52	2022/01/07	0.735	0.012	0.723	0.042
53	2022/01/07	0.749	0.009	0.740	0.043
54	2022/01/07	0.732	0.009	0.723	0.042
55	2022/01/07	0.717	0.010	0.707	0.042
56	2022/01/07	0.717	0.010	0.707	0.042
57	2022/01/21	0.728	0.009	0.719	0.042
58	2022/01/21	0.732	0.010	0.722	0.042
59	2022/01/21	0.710	0.009	0.701	0.043
60	2022/01/21	0.723	0.010	0.713	0.042
61	2022/01/21	0.722	0.010	0.712	0.042

DGS OC #1					
	Tested TC (%) average	0.544		average (%)	
	Standard deviation	0.010		0.516	0.032
No.	**Testing date**	**TC (%)**	**error (%)**	**TOC (%)**	**TIC (%)**
45	2021/12/24	0.536	0.028	0.508	0.043
46	2021/12/24	0.530	0.026	0.504	0.042
47	2021/12/24	0.527	0.026	0.502	0.042
48	2021/12/24	0.537	0.026	0.511	0.043
49	2021/12/24	0.532	0.027	0.505	0.042
50	2021/12/24	0.531	0.026	0.505	0.042
51	2021/12/24	0.535	0.028	0.507	0.042
52	2021/12/24	0.531	0.027	0.503	0.042
53	2021/12/24	0.528	0.027	0.501	0.042
54	2021/12/24	0.528	0.027	0.501	0.042
55	2021/12/24	0.544	0.027	0.518	0.042
56	2021/12/24	0.532	0.027	0.505	0.042
57	2021/12/24	0.535	0.026	0.509	0.043
58	2021/12/24	0.536	0.027	0.509	0.043

doi:10.6342/NTU202301546

Leco Soil standard					
	Tested TC (%) average	0.721		Reported TC (%)	0.717
	Standard deviation	0.015		+/-	0.027
No.	**Testing date**	**TC (%)**	**error (%)**	**TOC (%)**	**TIC (%)**
62	2022/01/21	0.722	0.012	0.710	0.043
63	2022/01/21	0.718	0.010	0.707	0.042
64	2022/01/21	0.724	0.009	0.715	0.043
65	2022/01/21	0.708	0.010	0.698	0.043
66	2022/01/21	0.706	0.010	0.696	0.043
67	2022/01/21	0.733	0.010	0.723	0.042
68	2022/01/21	0.742	0.012	0.730	0.043
69	2022/01/21	0.710	0.011	0.699	0.043
70	2022/01/21	0.728	0.012	0.716	0.043
71	2022/01/21	0.715	0.010	0.704	0.042
72	2022/01/21	0.718	0.009	0.709	0.043
73	2022/01/21	0.724	0.010	0.714	0.042
74	2022/01/21	0.710	0.011	0.700	0.042
75	2022/01/21	0.700	0.011	0.690	0.042

DGS OC #1					
	Tested TC (%) average	0.544		average (%)	
	Standard deviation	0.010		0.516	0.032
No.	**Testing date**	**TC (%)**	**error (%)**	**TOC (%)**	**TIC (%)**

doi:10.6342/NTU202301546

Table 7. Testing EA data of DGS TC #1.

DGS TC #1					
Tested TC (%) average		0.758		average (%)	
Standard deviation		0.015		0.578	0.180
No.	**Testing date**	**TC (%)**	**error (%)**	**TOC (%)**	**TIC (%)**
1	2021/11/29	0.740	0.012	0.568	0.173
2	2021/11/29	0.754	0.012	0.581	0.173
3	2021/11/29	0.730	0.012	0.564	0.167
4	2021/11/29	0.749	0.012	0.566	0.183
5	2021/11/29	0.743	0.013	0.571	0.172
6	2021/11/29	0.755	0.012	0.578	0.177
7	2021/11/29	0.741	0.013	0.563	0.178
8	2021/11/29	0.738	0.012	0.555	0.183
9	2021/11/29	0.739	0.012	0.555	0.184
10	2021/11/29	0.725	0.013	0.568	0.158
11	2021/11/29	0.736	0.013	0.552	0.184
12	2021/11/29	0.747	0.012	0.562	0.185
13	2021/11/29	0.740	0.012	0.547	0.193
14	2021/11/29	0.749	0.012	0.558	0.191
15	2021/11/29	0.762	0.012	0.579	0.183
16	2021/11/29	0.747	0.012	0.569	0.178
17	2021/11/29	0.733	0.012	0.571	0.162
18	2021/11/29	0.777	0.012	0.603	0.174
19	2021/11/29	0.721	0.013	0.569	0.152
20	2021/11/29	0.746	0.013	0.596	0.151
21	2021/11/29	0.745	0.012	0.583	0.162
22	2021/11/29	0.753	0.012	0.584	0.168
23	2021/11/29	0.744	0.013	0.572	0.172
24	2021/11/29	0.748	0.012	0.570	0.179
25	2021/12/24	0.780	0.043	0.590	0.190
26	2021/12/24	0.780	0.043	0.591	0.189
27	2021/12/24	0.784	0.043	0.602	0.182
28	2021/12/24	0.777	0.042	0.597	0.181
29	2021/12/24	0.776	0.042	0.590	0.186
30	2021/12/24	0.779	0.042	0.586	0.193
31	2021/12/24	0.790	0.043	0.614	0.177
32	2021/12/24	0.779	0.042	0.589	0.190
33	2021/12/24	0.765	0.043	0.573	0.192

doi:10.6342/NTU202301546

DGS TC #1					
Tested TC (%) average		0.758		average (%)	
Standard deviation		0.015		0.578	0.180
No.	**Testing date**	**TC (%)**	**error (%)**	**TOC (%)**	**TIC (%)**
34	2021/12/24	0.771	0.042	0.580	0.190
35	2021/12/24	0.772	0.042	0.583	0.189
36	2021/12/24	0.765	0.043	0.579	0.186
37	2021/12/24	0.774	0.042	0.587	0.187
38	2021/12/24	0.756	0.043	0.587	0.169
39	2021/12/24	0.765	0.042	0.584	0.181
40	2021/12/24	0.762	0.042	0.595	0.167
41	2021/12/24	0.770	0.043	0.598	0.172
42	2021/12/24	0.755	0.043	0.578	0.176
43	2021/12/24	0.758	0.042	0.581	0.177
44	2021/12/24	0.749	0.042	0.576	0.173
45	2022/01/21	0.759	0.042	0.568	0.191
46	2022/01/21	0.753	0.042	0.574	0.179
47	2022/01/21	0.757	0.042	0.583	0.174
48	2022/01/21	0.763	0.042	0.566	0.197
49	2022/01/21	0.768	0.042	0.569	0.199
50	2022/01/21	0.756	0.042	0.564	0.191
51	2022/01/21	0.753	0.042	0.589	0.164
52	2022/01/21	0.766	0.042	0.578	0.187
53	2022/01/21	0.762	0.042	0.575	0.188
54	2022/01/21	0.767	0.043	0.582	0.185
55	2022/01/21	0.755	0.043	0.582	0.173
56	2022/01/21	0.771	0.042	0.575	0.196
57	2022/01/21	0.767	0.042	0.578	0.189
58	2022/01/21	0.765	0.042	0.578	0.187
59	2022/01/21	0.760	0.042	0.577	0.184
60	2022/01/21	0.766	0.042	0.584	0.182
61	2022/01/21	0.763	0.042	0.585	0.178
62	2022/01/21	0.757	0.042	0.577	0.181
63	2022/01/21	0.765	0.043	0.585	0.180
64	2022/01/21	0.777	0.042	0.582	0.195

doi:10.6342/NTU202301546

Table 8. Chemicals for opal analysis.

Chemicals	Concentration	CAS No.	Serial No.	Manufacturer
Sodium hydroxide	≥99%	1310-73-2	CANL-1064981000	EMSURE (MERCK)
Hydrogen peroxide	30.0%~35.5%	7722-84-1	CAJO-18084-00	KANTO
Hydrochloric acid	≥37%	7647-01-0	30721-2.5L-GL	HONEYWELL
Ammonium molybdate (VI) tetrahydrate	≥99%	12054-85-2	AR-42331-100G	ACROS
Sulfuric acid	95-97%	7664-93-9	1.00731.2500	EMSURE (MERCK)

Table 9. Standards for opal analysis.

Standards	Concentration	Serial No.	Lot No.	Manufacturer
Silicon Standard for ICP	1000 mg/L	15747-100ML	BCBW7205	SIGMA

doi:10.6342/NTU202301546

Table 10. Site U1541 data.

Hole, core, section	Top offset (cm)	Bottom offset (cm)	Top depth CCSF-A (m)	Bottom depth CCSF-A (m)	Age (Ma)	LSR (cm/kyr)	Bulk density (g/cm^3)	TC (%)	error (%)	TOC (%)	$CaCO_3$ (%)	opal (%)	TOC MAR (g cm^{-2} kyr^{-1})	$CaCO_3$ MAR (g cm^{-2} kyr^{-1})	opal MAR (g cm^{-2} kyr^{-1})
C-12H-2	109	110	106.03	106.04	5.57	0.57	1.35	4.651	0.047	1.663	24.899	19.243	0.013	0.191	0.147
C-12H-2	118	119	106.12	106.13	5.58	0.57	1.36	4.804	0.048	1.875	24.404	18.431	0.014	0.188	0.142
C-12H-2	129	130	106.23	106.24	5.60	0.57	1.38	5.319	0.046	1.743	29.796	20.808	0.014	0.232	0.162
C-12H-2	138	139	106.33	106.34	5.62	0.57	1.38	5.381	0.048	1.688	30.771	19.365	0.013	0.241	0.152
C-12H-3	0	1	106.45	106.46	5.64	0.57	1.42	7.154	0.051	1.504	47.077	12.024	0.012	0.379	0.097
C-12H-3	10	11	106.55	106.56	5.66	0.57	1.50	8.369	0.055	1.204	59.703	9.764	0.010	0.508	0.083
C-12H-3	20	21	106.65	106.66	5.68	0.57	1.43	6.585	0.051	1.403	43.179	13.069	0.011	0.350	0.106
C-12H-3	30	31	106.75	106.76	5.69	0.57	1.39	5.073	0.048	0.913	34.670	17.899	0.007	0.273	0.141
C-12H-3	40	41	106.85	106.86	5.71	0.57	1.44	7.767	0.053	1.166	55.009	10.520	0.010	0.449	0.086
C-12H-3	50	51	106.95	106.96	5.73	0.57	1.47	8.180	0.054	1.143	58.636	8.346	0.010	0.490	0.070
C-12H-3	60	61	107.05	107.06	5.75	0.57	1.47	8.035	0.053	1.171	57.198	9.438	0.010	0.477	0.079
C-12H-3	70	71	107.15	107.16	5.76	0.57	1.45	7.169	0.050	1.351	48.483	12.476	0.011	0.398	0.103
C-12H-3	80	81	107.25	107.26	5.78	0.57	1.42	6.038	0.049	1.538	37.503	14.803	0.012	0.302	0.119
C-12H-3	90	91	107.35	107.36	5.80	0.57	1.41	6.093	0.050	1.574	37.658	14.294	0.013	0.301	0.114
C-12H-3	100	101	107.45	107.46	5.82	0.57	1.49	8.213	0.053	1.130	59.028	10.282	0.010	0.498	0.087
C-12H-3	110	111	107.55	107.56	5.83	0.57	1.46	9.236	0.053	0.946	69.087	6.889	0.008	0.571	0.057
C-12H-3	120	121	107.65	107.66	5.85	0.57	1.50	9.209	0.056	0.917	69.092	7.393	0.008	0.586	0.063
C-12H-3	130	131	107.75	107.76	5.87	0.57	1.52	8.875	0.054	0.970	65.875	8.885	0.008	0.567	0.076
C-12H-3	140	141	107.85	107.86	5.89	0.57	1.42	7.214	0.049	1.354	48.840	12.338	0.011	0.393	0.099

Hole, core, section	Top offset (cm)	Bottom offset (cm)	Top depth CCSF-A (m)	Bottom depth CCSF-A (m)	Age (Ma)	LSR (cm/kyr)	Bulk density (g/cm^3)	TC (%)	error (%)	TOC (%)	$CaCO_3$ (%)	opal (%)	TOC MAR ($g\ cm^{-2}\ kyr^{-1}$)	$CaCO_3$ MAR ($g\ cm^{-2}\ kyr^{-1}$)	opal MAR ($g\ cm^{-2}\ kyr^{-1}$)
C-12H-4	0	1	107.96	107.97	5.91	0.57	1.44	6.797	0.050	1.453	44.528	12.596	0.012	0.362	0.102
C-12H-4	10	11	108.06	108.07	5.92	0.57	1.44	6.652	0.048	1.389	43.855	13.807	0.011	0.357	0.113
C-12H-4	20	21	108.16	108.17	5.94	0.57	1.36	4.832	0.046	1.629	26.696	18.680	0.013	0.206	0.144
C-12H-4	30	31	108.26	108.27	5.96	0.57	1.40	4.993	0.048	1.639	27.948	19.724	0.013	0.221	0.156
C-12H-4	40	41	108.36	108.37	5.98	0.57	1.39	5.250	0.044	1.659	29.928	18.963	0.013	0.235	0.149
C-12H-4	50	51	108.46	108.47	6.00	0.57	1.34	3.848	0.043	1.828	16.831	22.188	0.014	0.128	0.169
C-12H-4	60	61	108.56	108.57	6.01	0.57	1.34	3.556	0.044	1.930	13.552	24.136	0.015	0.103	0.184
C-12H-4	70	71	108.66	108.67	6.03	1.37	1.38	5.197	0.046	1.791	28.386	19.971	0.034	0.534	0.376
C-12H-4	80	81	108.76	108.77	6.04	1.73	1.41	6.411	0.050	1.537	40.619	15.754	0.038	0.995	0.386
C-12H-4	90	91	108.86	108.87	6.04	1.73	1.41	5.741	0.048	1.585	34.631	17.943	0.039	0.843	0.437
C-12H-4	100	101	108.96	108.97	6.05	1.73	1.38	4.604	0.046	1.660	24.530	21.545	0.040	0.585	0.514
C-12H-4	110	111	109.06	109.07	6.06	1.73	1.35	3.510	0.044	1.887	13.525	24.381	0.044	0.316	0.569
C-12H-4	120	121	109.16	109.17	6.06	1.73	1.34	3.832	0.044	1.963	15.572	24.968	0.046	0.362	0.580
C-12H-4	130	131	109.26	109.27	6.07	1.73	1.36	4.316	0.046	1.882	20.281	23.135	0.045	0.480	0.547
C-12H-4	140	141	109.36	109.37	6.07	1.73	1.37	5.023	0.046	1.852	26.430	23.098	0.044	0.628	0.549
C-12H-5	0	1	109.47	109.48	6.08	1.73	1.48	8.225	0.052	1.228	58.306	11.746	0.031	1.493	0.301
C-12H-5	10	11	109.57	109.58	6.08	1.73	1.50	8.932	0.056	0.961	66.427	9.682	0.025	1.723	0.251
C-12H-5	20	21	109.67	109.68	6.09	1.73	1.49	8.645	0.049	1.095	62.914	10.096	0.028	1.625	0.261
C-12H-5	30	31	109.77	109.78	6.10	1.73	1.41	6.759	0.050	1.308	45.425	16.231	0.032	1.110	0.396
C-12H-5	40	41	109.87	109.88	6.10	1.73	1.42	6.004	0.047	1.341	38.853	17.619	0.033	0.956	0.433

doi:10.6342/NTU202301546

Hole, core, section	Top offset (cm)	Bottom offset (cm)	Top depth CCSF-A (m)	Bottom depth CCSF-A (m)	Age (Ma)	LSR (cm/kyr)	Bulk density (g/cm^3)	TC (%)	error (%)	TOC (%)	$CaCO_3$ (%)	opal (%)	TOC MAR (g cm^{-2} kyr^{-1})	$CaCO_3$ MAR (g cm^{-2} kyr^{-1})	opal MAR (g cm^{-2} kyr^{-1})
C-12H-5	50	51	109.97	109.98	6.11	1.73	1.38	4.980	0.044	1.606	28.117	21.174	0.038	0.673	0.507
C-12H-5	60	61	110.07	110.08	6.11	1.73	1.38	5.246	0.044	1.777	28.908	18.399	0.043	0.693	0.441
C-12H-5	70	71	110.17	110.18	6.12	1.73	1.44	6.691	0.046	1.506	43.208	14.214	0.038	1.077	0.354
C-12H-5	80	81	110.27	110.28	6.13	1.73	1.43	7.499	0.052	1.273	51.885	12.568	0.031	1.283	0.311
C-12H-5	90	91	110.37	110.38	6.13	1.73	1.45	7.555	0.048	1.205	52.918	11.787	0.030	1.330	0.296
C-12H-5	100	101	110.47	110.48	6.14	1.73	1.44	6.970	0.049	1.419	46.258	13.165	0.035	1.152	0.328
C-12H-5	110	111	110.57	110.58	6.14	1.73	1.49	7.940	0.052	1.192	56.233	9.784	0.031	1.455	0.253
C-12H-5	120	121	110.67	110.68	6.15	1.73	1.57	9.753	0.055	0.819	74.450	4.742	0.022	2.026	0.129
C-12H-5	130	131	110.77	110.78	6.15	1.73	1.55	9.608	0.054	0.830	73.152	5.322	0.022	1.971	0.143
C-12H-5	140	141	110.87	110.88	6.16	1.73	1.51	8.715	0.051	1.044	63.918	7.361	0.027	1.671	0.192
C-12H-6	0	1	110.98	110.99	6.17	1.73	1.51	8.592	0.055	1.224	61.394	11.951	0.032	1.604	0.312
C-12H-6	10	11	111.08	111.09	6.17	1.73	1.55	9.225	0.052	1.026	68.331	6.690	0.028	1.834	0.180
C-12H-6	20	21	111.18	111.19	6.18	1.73	1.57	9.706	0.055	0.891	73.463	4.316	0.024	1.999	0.117
C-12H-6	30	31	111.28	111.29	6.18	1.73	1.56	9.779	0.056	0.876	74.188	5.400	0.024	2.004	0.146
C-12H-6	40	41	111.38	111.39	6.19	1.73	1.57	10.275	0.056	0.719	79.630	5.723	0.020	2.168	0.156
C-12H-6	50	51	111.48	111.49	6.19	1.73	1.63	10.696	0.054	0.586	84.245	3.860	0.017	2.385	0.109
C-12H-6	60	61	111.58	111.59	6.20	1.73	1.61	10.092	0.056	0.704	78.225	4.282	0.020	2.186	0.120
C-12H-3	40	41	111.77	111.78	6.21	1.73	1.47	7.738	0.048	1.121	55.139	9.905	0.029	1.406	0.253
C-12H-3	50	51	111.87	111.88	6.22	1.73	1.49	7.359	0.051	0.553	56.717	8.676	0.014	1.460	0.223
C-12H-3	60	61	111.97	111.98	6.22	1.73	1.52	8.823	0.054	1.021	65.013	6.565	0.027	1.715	0.173

doi:10.6342/NTU202301546

Hole, core, section	Top offset (cm)	Bottom offset (cm)	Top depth CCSF-A (m)	Bottom depth CCSF-A (m)	Age (Ma)	LSR (cm/kyr)	Bulk density (g/cm^3)	TC (%)	error (%)	TOC (%)	$CaCO_3$ (%)	opal (%)	TOC MAR ($g\ cm^{-2}\ kyr^{-1}$)	$CaCO_3$ MAR ($g\ cm^{-2}\ kyr^{-1}$)	opal MAR ($g\ cm^{-2}\ kyr^{-1}$)
B-12H-3	70	71	112.07	112.08	6.23	1.73	1.57	9.937	0.052	0.801	76.135	4.447	0.022	2.066	0.121
B-12H-3	80	81	112.17	112.18	6.23	1.73	1.56	9.818	0.056	0.828	74.916	6.183	0.022	2.030	0.168
B-12H-3	90	91	112.27	112.28	6.24	1.73	1.53	9.526	0.057	0.897	71.911	6.027	0.024	1.908	0.160
B-12H-3	100	101	112.37	112.38	6.25	1.73	1.53	9.343	0.049	0.903	70.335	6.260	0.024	1.865	0.166
B-12H-3	110	111	112.47	112.48	6.25	1.28	1.50	8.456	0.052	1.165	60.760	8.045	0.022	1.166	0.154
B-12H-3	120	121	112.57	112.58	6.26	1.27	1.49	7.871	0.053	1.309	54.678	10.186	0.025	1.033	0.192
B-12H-3	130	131	112.67	112.68	6.27	1.27	1.53	9.297	0.055	0.929	69.737	5.830	0.018	1.353	0.113
B-12H-3	140	141	112.77	112.78	6.28	1.27	1.58	9.913	0.054	0.834	75.653	4.637	0.017	1.514	0.093
B-12H-4	0	1	112.88	112.89	6.28	1.27	1.60	10.292	0.057	0.669	80.192	3.770	0.014	1.625	0.076
B-12H-4	10	11	112.98	112.99	6.29	1.27	1.55	9.306	0.055	0.878	70.229	6.376	0.017	1.385	0.126
B-12H-4	20	21	113.08	113.09	6.30	1.27	1.49	8.708	0.054	1.010	64.149	8.120	0.019	1.210	0.153
B-12H-4	30	31	113.18	113.19	6.31	1.27	1.45	7.223	0.048	1.401	48.514	11.316	0.026	0.890	0.208
B-12H-4	40	41	113.28	113.29	6.32	1.27	1.46	7.900	0.052	1.209	55.761	10.457	0.022	1.034	0.194
B-12H-4	50	51	113.38	113.39	6.32	1.27	1.50	8.194	0.054	1.138	58.798	9.312	0.022	1.118	0.177
B-12H-4	60	61	113.48	113.49	6.33	1.27	1.47	7.726	0.053	1.298	53.564	10.787	0.024	0.998	0.201
B-12H-4	70	71	113.58	113.59	6.34	1.27	1.49	7.765	0.053	1.256	54.243	12.198	0.024	1.025	0.230
B-12H-4	80	81	113.68	113.69	6.35	1.27	1.53	8.903	0.056	1.049	65.447	8.424	0.020	1.273	0.164
B-13H-1	0	1	113.75	113.76	6.35	1.27	1.39	8.904	0.054	1.061	65.357	5.811	0.019	1.156	0.103
B-12H-4	90	91	113.78	113.79	6.35	1.27	1.57	9.680	0.046	0.779	74.170	5.784	0.016	1.479	0.115
B-13H-1	10	11	113.85	113.86	6.36	1.27	1.50	9.555	0.051	0.861	72.448	5.425	0.016	1.381	0.103

Hole, core, section	Top offset (cm)	Bottom offset (cm)	Top depth CCSF-A (m)	Bottom depth CCSF-A (m)	Age (Ma)	LSR (cm/kyr)	Bulk density (g/cm^3)	TC (%)	error (%)	TOC (%)	$CaCO_3$ (%)	opal (%)	TOC MAR (g cm^{-2} kyr^{-1})	$CaCO_3$ MAR (g cm^{-2} kyr^{-1})	opal MAR (g cm^{-2} kyr^{-1})
B-12H-4	100	101	113.88	113.89	6.36	1.27	1.54	9.279	0.050	0.854	70.210	6.647	0.017	1.368	0.130
C-13H-1	20	21	113.95	113.96	6.37	1.27	1.53	9.378	0.052	0.916	70.520	4.703	0.018	1.365	0.091
B-12H-4	110	111	113.98	113.99	6.37	1.27	1.48	9.419	0.055	0.864	71.290	7.053	0.016	1.340	0.133
C-13H-1	30	31	114.05	114.06	6.38	1.27	1.50	9.042	0.049	1.016	66.876	6.339	0.019	1.274	0.121
B-12H-4	120	121	114.08	114.09	6.38	1.27	1.43	9.083	0.054	0.863	68.493	6.329	0.016	1.239	0.115
B-12H-4	130	131	114.18	114.19	6.39	1.27	1.37	8.364	0.053	1.149	60.121	8.989	0.020	1.046	0.156
B-12H-4	140	141	114.28	114.29	6.39	1.27	1.31	6.445	0.049	1.401	42.034	14.599	0.023	0.700	0.243
B-12H-5	0	1	114.38	114.39	6.40	1.27	1.25	7.743	0.048	1.360	53.194	11.168	0.022	0.843	0.177
B-12H-5	10	11	114.48	114.49	6.41	1.27	1.53	8.743	0.054	1.022	64.336	8.510	0.020	1.250	0.165
B-12H-5	20	21	114.58	114.59	6.42	1.27	1.56	9.319	0.049	0.912	70.057	7.278	0.018	1.384	0.144
B-12H-5	30	31	114.68	114.69	6.43	1.27	1.50	8.005	0.053	1.116	57.404	10.070	0.021	1.094	0.192
B-12H-5	40	41	114.78	114.79	6.43	0.92	1.50	8.151	0.053	1.243	57.560	10.053	0.017	0.794	0.139
C-13H-2	0	1	115.25	115.26	6.49	0.91	1.45	5.827	0.046	1.601	35.211	11.279	0.021	0.461	0.148
C-13H-2	10	11	115.35	115.36	6.50	0.91	1.41	6.541	0.049	1.479	42.185	9.594	0.019	0.540	0.123
C-13H-2	20	21	115.45	115.46	6.51	0.91	1.41	5.887	0.045	1.584	35.856	13.709	0.020	0.459	0.176
C-13H-2	30	31	115.55	115.56	6.52	0.91	1.43	6.034	0.047	1.677	36.302	13.190	0.022	0.469	0.170
C-13H-2	40	41	115.65	115.66	6.53	0.91	1.48	7.192	0.050	1.311	49.014	7.869	0.018	0.657	0.105
C-13H-2	50	51	115.75	115.76	6.54	0.91	1.45	7.362	0.050	1.411	49.589	8.664	0.019	0.652	0.114
C-13H-2	60	61	115.85	115.86	6.55	0.91	1.45	6.740	0.047	1.418	44.347	9.245	0.019	0.581	0.121
C-13H-2	70	71	115.95	115.96	6.56	0.91	1.42	6.266	0.048	1.450	40.132	11.169	0.019	0.515	0.143

Hole, core, section	Top offset (cm)	Bottom offset (cm)	Top depth CCSF-A (m)	Bottom depth CCSF-A (m)	Age (Ma)	LSR (cm/kyr)	Bulk density (g/cm^3)	TC (%)	error (%)	TOC (%)	$CaCO_3$ (%)	opal (%)	TOC MAR (g cm^{-2} kyr^{-1})	$CaCO_3$ MAR (g cm^{-2} kyr^{-1})	opal MAR (g cm^{-2} kyr^{-1})
C-13H-2	80	81	116.05	116.06	6.57	0.91	1.39	5.340	0.043	1.775	29.713	12.769	0.022	0.374	0.161
C-13H-2	90	91	116.15	116.16	6.58	0.91	1.42	6.415	0.048	1.406	41.737	10.823	0.018	0.538	0.140
C-13H-2	100	101	116.25	116.26	6.60	0.91	1.47	7.044	0.048	1.431	46.770	10.808	0.019	0.621	0.143
C-13H-2	110	111	116.35	116.36	6.61	0.91	1.43	6.320	0.047	1.451	40.582	10.815	0.019	0.526	0.140
C-13H-2	120	121	116.45	116.46	6.62	0.91	1.38	5.471	0.046	1.660	31.764	13.508	0.021	0.396	0.168
C-13H-2	130	131	116.55	116.56	6.63	0.91	1.35	4.968	0.046	1.724	27.028	14.115	0.021	0.331	0.173
C-13H-2	140	141	116.65	116.66	6.64	0.91	1.36	5.228	0.044	1.576	30.433	13.425	0.019	0.376	0.166
C-13H-3	0	1	116.77	116.78	6.65	0.91	1.42	5.804	0.046	1.708	34.134	11.896	0.022	0.438	0.153
C-13H-3	10	11	116.87	116.88	6.66	0.91	1.41	6.212	0.047	1.598	38.445	11.853	0.020	0.490	0.151
C-13H-3	20	21	116.97	116.98	6.68	0.91	1.48	8.186	0.050	1.259	57.728	8.150	0.017	0.773	0.109
C-13H-3	30	31	117.07	117.08	6.69	0.91	1.58	10.114	0.054	0.767	77.888	4.928	0.011	1.117	0.071
C-13H-3	40	41	117.17	117.18	6.70	0.91	1.62	10.433	0.052	0.600	81.940	4.672	0.009	1.206	0.069
C-13H-3	50	51	117.27	117.28	6.71	0.91	1.62	10.362	0.053	0.613	81.239	5.093	0.009	1.193	0.075
C-13H-3	60	61	117.37	117.38	6.72	0.91	1.64	10.548	0.059	0.550	83.308	3.930	0.008	1.240	0.059
C-13H-3	70	71	117.47	117.48	6.73	1.34	1.66	10.717	0.057	0.478	85.318	3.448	0.011	1.899	0.077
C-13H-3	80	81	117.57	117.58	6.74	1.55	1.68	10.869	0.055	0.433	86.965	3.118	0.011	2.256	0.081
C-13H-3	90	91	117.67	117.68	6.74	1.55	1.67	11.221	0.058	0.440	89.841	2.377	0.011	2.327	0.062
C-13H-3	100	101	117.77	117.78	6.75	1.55	1.67	10.787	0.060	0.495	85.767	4.042	0.013	2.213	0.104
C-13H-3	110	111	117.87	117.88	6.76	1.55	1.63	10.357	0.059	0.666	80.757	4.804	0.017	2.044	0.122
C-13H-3	120	121	117.97	117.98	6.76	1.55	1.56	9.117	0.055	0.996	67.672	7.221	0.024	1.635	0.174

doi:10.6342/NTU202301546

Hole, core, section	Top offset (cm)	Bottom offset (cm)	Top depth CCSF-A (m)	Bottom depth CCSF-A (m)	Age (Ma)	LSR (cm/kyr)	Bulk density (g/cm^3)	TC (%)	error (%)	TOC (%)	$CaCO_3$ (%)	opal (%)	TOC MAR (g cm^{-2} kyr^{-1})	$CaCO_3$ MAR (g cm^{-2} kyr^{-1})	opal MAR (g cm^{-2} kyr^{-1})
C-13H-3	130	131	118.07	118.08	6.77	1.55	1.57	9.206	0.055	0.974	68.601	7.163	0.024	1.663	0.174
C-13H-3	140	141	118.17	118.18	6.78	1.55	1.59	9.509	0.055	0.804	72.534	7.006	0.020	1.783	0.172
C-13H-4	0	1	118.29	118.30	6.78	1.55	1.51	8.367	0.054	1.204	59.684	9.387	0.028	1.392	0.219
C-13H-4	10	11	118.39	118.40	6.79	1.55	1.46	5.517	0.048	1.876	30.345	16.245	0.042	0.684	0.366
C-13H-4	20	21	118.49	118.50	6.80	1.55	1.47	7.529	0.051	1.492	50.312	10.797	0.034	1.144	0.246
C-13H-4	30	31	118.59	118.60	6.80	1.55	1.49	8.108	0.050	1.275	56.941	8.981	0.029	1.316	0.208
C-13H-4	40	41	118.69	118.70	6.81	1.55	1.45	7.055	0.049	1.372	47.356	8.645	0.031	1.062	0.194
C-13H-4	50	51	118.79	118.80	6.82	1.55	1.44	6.643	0.046	1.535	42.572	14.585	0.034	0.946	0.324
C-13H-4	60	61	118.89	118.90	6.82	1.55	1.47	7.280	0.050	1.410	48.917	11.640	0.032	1.115	0.265
C-13H-4	70	71	118.99	119.00	6.83	1.55	1.43	6.767	0.049	1.406	44.674	11.263	0.031	0.986	0.249
C-13H-4	80	81	119.09	119.10	6.84	1.55	1.36	4.191	0.044	1.769	20.182	19.567	0.037	0.425	0.412
C-13H-4	90	91	119.19	119.20	6.84	1.55	1.37	4.849	0.046	1.819	25.255	15.012	0.038	0.534	0.317
C-13H-4	100	101	119.29	119.30	6.85	1.55	1.36	5.048	0.045	1.978	25.587	16.082	0.042	0.538	0.338
C-13H-4	110	111	119.39	119.40	6.86	1.55	1.34	4.282	0.045	2.042	18.665	16.938	0.042	0.387	0.351
C-13H-4	120	121	119.49	119.50	6.86	1.55	1.35	3.726	0.045	1.970	14.632	18.050	0.041	0.306	0.378
C-13H-4	130	131	119.59	119.60	6.87	1.55	1.35	4.539	0.045	1.791	22.894	17.959	0.038	0.480	0.377
C-13H-4	140	141	119.69	119.70	6.87	1.55	1.40	5.540	0.046	1.727	31.781	15.684	0.037	0.687	0.339
C-13H-5	0	1	119.82	119.83	6.88	1.55	1.57	8.872	0.053	1.085	64.884	8.502	0.026	1.580	0.207
C-13H-5	10	11	119.92	119.93	6.89	1.55	1.55	8.961	0.052	1.005	66.293	7.781	0.024	1.592	0.187
C-13H-5	20	21	120.02	120.03	6.90	1.55	1.50	8.337	0.052	1.203	59.446	10.285	0.028	1.383	0.239

doi:10.6342/NTU202301546

Hole, core, section	Top offset (cm)	Bottom offset (cm)	Top depth CCSF-A (m)	Bottom depth CCSF-A (m)	Age (Ma)	LSR (cm/kyr)	Bulk density (g/cm^3)	TC (%)	error (%)	TOC (%)	$CaCO_3$ (%)	opal (%)	TOC MAR (g cm^{-2} kyr^{-1})	$CaCO_3$ MAR (g cm^{-2} kyr^{-1})	opal MAR (g cm^{-2} kyr^{-1})
C-13H-5	30	31	120.12	120.13	6.90	1.55	1.51	8.140	0.053	1.296	57.034	10.422	0.030	1.334	0.244
C-13H-5	40	41	120.22	120.23	6.91	1.55	1.61	10.390	0.055	0.667	81.023	5.338	0.017	2.023	0.133
C-13H-5	50	51	120.32	120.33	6.92	1.55	1.58	10.104	0.057	0.817	77.382	6.157	0.020	1.897	0.151
C-13H-5	60	61	120.42	120.43	6.92	1.55	1.58	9.386	0.051	0.913	70.601	5.988	0.022	1.727	0.146
C-13H-5	70	71	120.52	120.53	6.93	1.55	1.49	8.493	0.052	1.203	60.744	10.125	0.028	1.405	0.234
C-13H-5	80	81	120.62	120.63	6.94	1.55	1.48	7.227	0.046	1.364	48.853	12.169	0.031	1.122	0.279
C-13H-5	90	91	120.72	120.73	6.94	1.55	1.50	8.005	0.051	1.286	55.995	8.395	0.030	1.299	0.195
C-13H-5	100	101	120.82	120.83	6.95	1.55	1.53	9.101	0.056	1.063	66.982	8.463	0.025	1.585	0.200
C-13H-5	110	111	120.92	120.93	6.95	1.55	1.46	9.364	0.054	1.063	69.177	8.819	0.024	1.562	0.199
C-13H-5	120	121	121.02	121.03	6.96	1.55	1.39	8.818	0.054	1.180	63.648	7.487	0.025	1.368	0.161
C-13H-5	130	131	121.12	121.13	6.97	1.55	1.32	7.932	0.050	1.240	55.764	9.925	0.025	1.138	0.203
C-13H-5	140	141	121.22	121.23	6.97	1.55	1.25	8.163	0.050	1.212	57.924	10.772	0.023	1.119	0.208
C-13H-6	0	1	121.33	121.34	6.98	1.55	1.52	8.143	0.052	1.372	56.424	6.111	0.032	1.324	0.143
C-13H-6	10	11	121.43	121.44	6.99	1.55	1.52	8.744	0.049	1.143	63.343	5.595	0.027	1.487	0.131
C-13H-6	20	21	121.53	121.54	6.99	1.55	1.51	8.485	0.051	1.158	61.057	6.577	0.027	1.429	0.154
C-13H-6	30	31	121.63	121.64	7.00	1.55	1.53	8.520	0.050	1.161	61.319	6.657	0.028	1.454	0.158
C-13H-6	40	41	121.73	121.74	7.01	1.55	1.60	9.206	0.051	0.969	68.640	5.391	0.024	1.696	0.133
C-13H-6	50	51	121.83	121.84	7.01	1.55	1.63	9.985	0.056	0.788	76.641	3.675	0.020	1.929	0.092
C-13H-6	60	61	121.93	121.94	7.02	1.55	1.62	9.875	0.057	0.749	76.051	4.729	0.019	1.909	0.119
C-13H-3	50	51	122.07	122.08	7.03	1.55	1.57	8.961	0.054	0.963	66.651	1.294	0.023	1.620	0.031

Hole, core, section	Top offset (cm)	Bottom offset (cm)	Top depth CCSF-A (m)	Bottom depth CCSF-A (m)	Age (Ma)	LSR (cm/kyr)	Bulk density (g/cm^3)	TC (%)	error (%)	TOC (%)	$CaCO_3$ (%)	opal (%)	TOC MAR (g cm^{-2} kyr^{-1})	$CaCO_3$ MAR (g cm^{-2} kyr^{-1})	opal MAR (g cm^{-2} kyr^{-1})
B-13H-3	60	61	122.17	122.18	7.04	1.55	1.46	7.232	0.048	1.278	49.618	13.849	0.029	1.125	0.314
B-13H-3	70	71	122.27	122.28	7.04	1.55	1.39	5.751	0.047	1.684	33.894	17.364	0.036	0.727	0.373
B-13H-3	80	81	122.37	122.38	7.05	1.55	1.40	5.960	0.049	1.613	36.218	21.507	0.035	0.787	0.467
B-13H-3	90	91	122.47	122.48	7.05	1.55	1.43	6.502	0.050	1.538	41.364	15.880	0.034	0.917	0.352
B-13H-3	100	101	122.57	122.58	7.06	1.55	1.46	7.217	0.050	1.383	48.621	15.007	0.031	1.102	0.340
B-13H-3	110	111	122.67	122.68	7.07	1.55	1.46	7.551	0.048	1.390	51.344	16.937	0.031	1.162	0.383
B-13H-3	120	121	122.77	122.78	7.07	1.55	1.41	6.012	0.049	1.650	36.350	17.261	0.036	0.792	0.376
B-13H-3	130	131	122.87	122.88	7.08	1.55	1.38	4.592	0.045	1.828	23.037	21.486	0.039	0.490	0.457
B-13H-3	140	141	122.97	122.98	7.09	1.55	1.36	4.841	0.045	1.884	24.642	20.923	0.040	0.518	0.440
B-13H-4	0	1	123.04	123.05	7.09	1.55	1.38	4.848	0.047	1.938	24.253	28.703	0.041	0.519	0.614
B-13H-4	10	11	123.14	123.15	7.10	1.55	1.39	4.920	0.045	1.888	25.268	19.330	0.041	0.544	0.416
B-13H-4	20	21	123.24	123.25	7.10	1.55	1.37	5.073	0.045	1.933	26.164	19.921	0.041	0.554	0.422
B-13H-4	30	31	123.34	123.35	7.11	1.55	1.39	5.169	0.048	1.764	28.378	21.188	0.038	0.611	0.456
B-13H-4	40	41	123.44	123.45	7.12	1.55	1.41	5.590	0.042	1.730	32.162	17.335	0.038	0.701	0.378
B-13H-4	50	51	123.54	123.55	7.12	1.55	1.42	5.515	0.047	1.776	31.162	18.842	0.039	0.685	0.414
B-13H-4	60	61	123.64	123.65	7.13	1.55	1.43	5.781	0.048	1.628	34.611	20.077	0.036	0.764	0.443
B-13H-4	70	71	123.74	123.75	7.14	1.34	1.43	5.894	0.048	1.648	35.381	18.376	0.032	0.678	0.352
B-13H-4	80	81	123.84	123.85	7.14	1.17	1.49	7.032	0.051	1.380	47.099	15.148	0.024	0.823	0.265
B-13H-4	90	91	123.94	123.95	7.15	1.17	1.46	7.182	0.050	1.306	48.969	15.087	0.022	0.838	0.258
B-13H-4	100	101	124.04	124.05	7.16	1.17	1.42	5.608	0.046	1.596	33.428	19.631	0.027	0.556	0.327

doi:10.6342/NTU202301546

Hole, core, section	Top offset (cm)	Bottom offset (cm)	Top depth CCSF-A (m)	Bottom depth CCSF-A (m)	Age (Ma)	LSR (cm/kyr)	Bulk density (g/cm^3)	TC (%)	error (%)	TOC (%)	$CaCO_3$ (%)	opal (%)	TOC MAR (g cm^{-2} kyr^{-1})	$CaCO_3$ MAR (g cm^{-2} kyr^{-1})	opal MAR (g cm^{-2} kyr^{-1})
B-13H-4	110	111	124.14	124.15	7.17	1.17	1.46	7.032	0.051	1.462	46.411	15.219	0.025	0.795	0.261
B-13H-4	120	121	124.24	124.25	7.18	1.17	1.46	7.038	0.050	1.294	47.866	14.516	0.022	0.821	0.249
B-13H-4	130	131	124.34	124.35	7.19	1.17	1.50	7.712	0.053	1.186	54.377	12.913	0.021	0.953	0.226
B-13H-4	140	141	124.44	124.45	7.20	1.17	1.51	8.586	0.050	1.070	62.638	11.164	0.019	1.106	0.197
B-13H-5	0	1	124.54	124.55	7.20	1.17	1.28	8.350	0.053	1.150	59.998	11.499	0.017	0.903	0.173
B-13H-5	10	11	124.64	124.65	7.21	1.17	1.51	8.234	0.053	1.192	58.683	12.088	0.021	1.035	0.213
B-13H-5	20	21	124.74	124.75	7.22	1.17	1.53	8.791	0.055	0.968	65.189	9.396	0.017	1.170	0.169
B-13H-5	30	31	124.84	124.85	7.23	1.17	1.51	8.339	0.054	1.157	59.844	11.562	0.020	1.055	0.204
B-13H-5	40	41	124.94	124.95	7.24	1.17	1.49	7.854	0.047	1.294	54.663	12.071	0.023	0.953	0.210
B-13H-5	50	51	125.04	125.05	7.25	1.17	1.53	8.524	0.052	1.135	61.574	10.207	0.020	1.105	0.183
B-13H-5	60	61	125.14	125.15	7.26	1.17	1.56	9.340	0.054	0.935	70.036	8.494	0.017	1.281	0.155
B-13H-5	70	71	125.24	125.25	7.26	1.33	1.58	9.061	0.056	0.922	67.825	9.934	0.019	1.422	0.208
B-13H-5	80	81	125.34	125.35	7.27	1.54	1.54	8.706	0.050	1.064	63.685	12.867	0.025	1.512	0.305
B-13H-5	90	91	125.44	125.45	7.28	1.54	1.53	8.271	0.050	1.232	58.653	12.786	0.029	1.376	0.300
B-13H-5	100	101	125.54	125.55	7.28	1.54	1.55	8.860	0.053	1.031	65.244	12.035	0.025	1.553	0.286
B-13H-5	110	111	125.64	125.65	7.29	1.54	1.54	8.596	0.054	1.045	62.918	12.542	0.025	1.492	0.297
B-13H-5	120	121	125.74	125.75	7.30	1.54	1.53	8.640	0.051	1.069	63.090	12.550	0.025	1.482	0.295
B-13H-5	130	131	125.84	125.85	7.30	1.54	1.53	8.794	0.050	0.999	64.956	10.847	0.024	1.529	0.255
B-13H-5	140	141	125.94	125.95	7.31	1.54	1.55	9.146	0.052	0.904	68.683	9.800	0.022	1.639	0.234
B-13H-6	0	1	126.05	126.06	7.32	1.54	1.55	8.943	0.053	1.021	66.018	12.069	0.024	1.578	0.289

Hole, core, section	Top offset (cm)	Bottom offset (cm)	Top depth CCSF-A (m)	Bottom depth CCSF-A (m)	Age (Ma)	LSR (cm/kyr)	Bulk density (g/cm^3)	TC (%)	error (%)	TOC (%)	$CaCO_3$ (%)	opal (%)	TOC MAR (g cm^{-2} kyr^{-1})	$CaCO_3$ MAR (g cm^{-2} kyr^{-1})	opal MAR (g cm^{-2} kyr^{-1})
B-13H-6	10	11	126.15	126.16	7.32	1.54	1.52	8.773	0.047	1.022	64.591	10.822	0.024	1.508	0.253
B-13H-6	20	21	126.25	126.26	7.33	1.54	1.53	8.987	0.050	0.935	67.100	10.110	0.022	1.577	0.238
B-13H-6	30	31	126.35	126.36	7.34	1.54	1.52	8.890	0.049	0.911	66.492	9.980	0.021	1.550	0.233
B-13H-6	40	41	126.45	126.46	7.34	1.54	1.52	9.227	0.056	0.904	69.360	10.587	0.021	1.620	0.247
B-13H-6	50	51	126.55	126.56	7.35	1.54	1.56	9.399	0.052	0.809	71.576	9.186	0.019	1.716	0.220
B-13H-6	60	61	126.65	126.66	7.36	1.54	1.56	9.413	0.052	0.790	71.861	9.106	0.019	1.720	0.218
B-13H-6	70	71	126.75	126.76	7.36	1.54	1.55	9.694	0.051	0.703	74.918	9.688	0.017	1.789	0.231
B-13H-6	80	81	126.85	126.86	7.37	1.54	1.58	10.184	0.055	0.624	79.666	6.862	0.015	1.935	0.167
B-13H-6	90	91	126.95	126.96	7.38	1.54	1.59	10.190	0.057	0.563	80.222	6.633	0.014	1.967	0.163
B-13H-6	100	101	127.05	127.06	7.38	1.54	1.57	10.058	0.051	0.659	78.320	6.723	0.016	1.897	0.163
B-13H-6	110	111	127.15	127.16	7.39	1.54	1.53	9.427	0.056	0.799	71.900	8.918	0.019	1.696	0.210
B-14H-1	0	1.5	128.55	128.56	7.48	1.54	1.54	10.433	0.059	0.646	81.556	5.345	0.015	1.938	0.127
B-14H-1	10	11	128.65	128.66	7.49	1.54	1.53	10.445	0.057	0.588	82.133	5.152	0.014	1.936	0.121
B-14H-1	20	21	128.75	128.76	7.49	1.54	1.65	10.707	0.057	0.485	85.182	3.994	0.012	2.166	0.102
B-14H-1	30	31	128.85	128.86	7.50	1.54	1.64	10.493	0.051	0.530	83.019	4.722	0.013	2.097	0.119
B-14H-1	40	41	128.95	128.96	7.51	1.54	1.65	10.385	0.058	0.544	82.005	5.044	0.014	2.087	0.128
B-14H-1	50	51	129.05	129.06	7.51	1.54	1.64	10.400	0.059	0.556	82.032	4.770	0.014	2.075	0.121
B-14H-1	60	61	129.15	129.16	7.52	1.54	1.63	10.174	0.053	0.592	79.846	5.732	0.015	2.001	0.144
B-14H-1	70	71	129.25	129.26	7.53	1.37	1.62	10.007	0.055	0.638	78.070	7.625	0.014	1.730	0.169
B-14H-1	80	81	129.35	129.36	7.53	1.27	1.62	10.169	0.058	0.662	79.228	8.209	0.014	1.634	0.169

doi:10.6342/NTU202301546

Hole, core, section	Top offset (cm)	Bottom offset (cm)	Top depth CCSF-A (m)	Bottom depth CCSF-A (m)	Age (Ma)	LSR (cm/kyr)	Bulk density (g/cm^3)	TC (%)	error (%)	TOC (%)	$CaCO_3$ (%)	opal (%)	TOC MAR (g cm^{-2} kyr^{-1})	$CaCO_3$ MAR (g cm^{-2} kyr^{-1})	opal MAR (g cm^{-2} kyr^{-1})
B-14H-1	90	91	129.45	129.46	7.54	1.27	1.61	10.106	0.058	0.617	79.079	8.465	0.013	1.623	0.174
B-14H-1	100	101	129.55	129.56	7.55	1.27	1.61	10.030	0.058	0.598	78.602	7.770	0.012	1.605	0.159
B-14H-1	110	111	129.65	129.66	7.56	1.27	1.62	10.139	0.046	0.612	79.392	7.809	0.013	1.634	0.161
B-14H-1	120	121	129.75	129.76	7.56	1.27	1.66	10.298	0.058	0.546	81.261	7.627	0.012	1.714	0.161
B-14H-1	130	131	129.85	129.86	7.57	1.27	1.66	10.442	0.052	0.497	82.880	7.502	0.010	1.748	0.158
B-14H-1	140	141	129.95	129.96	7.58	1.27	1.69	10.661	0.055	0.476	84.872	5.914	0.010	1.823	0.127
B-14H-2	0	1	130.02	130.03	7.59	1.27	1.69	10.724	0.052	0.451	85.607	7.038	0.010	1.835	0.151
B-14H-2	10	11	130.12	130.13	7.59	1.27	1.69	10.697	0.057	0.451	85.379	5.311	0.010	1.832	0.114
B-14H-2	20	21	130.22	130.23	7.60	1.27	1.64	10.337	0.052	0.528	81.736	6.507	0.011	1.704	0.136
B-14H-2	30	31	130.32	130.33	7.61	1.27	1.64	10.234	0.056	0.556	80.651	3.634	0.012	1.679	0.076
B-14H-2	40	41	130.42	130.43	7.62	1.27	1.67	10.527	0.054	0.511	83.464	3.847	0.011	1.771	0.082
B-14H-2	50	51	130.52	130.53	7.62	1.27	1.65	10.393	0.057	0.498	82.453	3.226	0.010	1.726	0.068
B-14H-2	60	61	130.62	130.63	7.63	1.27	1.63	10.477	0.055	0.521	82.964	2.729	0.011	1.720	0.057
B-14H-2	70	71	130.72	130.73	7.64	2.25	1.66	10.498	0.057	0.467	83.596	2.676	0.017	3.133	0.100
B-14H-2	80	81	130.82	130.83	7.64	2.83	1.72	10.865	0.055	0.379	87.374	3.723	0.018	4.252	0.181
B-14H-2	90	91	130.92	130.93	7.65	2.83	1.73	11.023	0.058	0.366	88.807	2.420	0.018	4.348	0.118
B-14H-2	100	101	131.02	131.03	7.65	2.83	1.70	11.036	0.061	0.477	87.989	2.190	0.023	4.241	0.106
B-14H-2	110	111	131.12	131.13	7.66	2.83	1.71	10.942	0.060	0.447	87.462	1.282	0.022	4.234	0.062
B-14H-2	120	121	131.22	131.23	7.66	2.83	1.71	10.861	0.056	0.391	87.248	2.210	0.019	4.217	0.107
B-14H-2	130	131	131.32	131.33	7.66	2.83	1.73	11.081	0.057	0.368	89.275	1.825	0.018	4.370	0.089

Hole, core, section	Top offset (cm)	Bottom offset (cm)	Top depth CCSF-A (m)	Bottom depth CCSF-A (m)	Age (Ma)	LSR (cm/kyr)	Bulk density (g/cm^3)	TC (%)	error (%)	TOC (%)	$CaCO_3$ (%)	opal (%)	TOC MAR ($g\ cm^{-2}\ kyr^{-1}$)	$CaCO_3$ MAR ($g\ cm^{-2}\ kyr^{-1}$)	opal MAR ($g\ cm^{-2}\ kyr^{-1}$)
B-14H-2	140	141	131.42	131.43	7.67	2.83	1.72	11.127	0.057	0.361	89.720	1.816	0.018	4.380	0.089
B-14H-3	0	1	131.50	131.51	7.67	2.83	1.72	11.033	0.056	0.386	88.725	2.273	0.019	4.315	0.111
B-14H-3	10	11	131.60	131.61	7.67	2.83	1.71	10.897	0.060	0.395	87.519	1.393	0.019	4.228	0.067
B-14H-3	20	21	131.70	131.71	7.68	2.83	1.73	10.994	0.055	0.403	88.257	2.086	0.020	4.317	0.102
B-14H-3	30	31	131.80	131.81	7.68	2.83	1.75	11.105	0.056	0.368	89.471	1.220	0.018	4.440	0.061
B-14H-3	40	41	131.90	131.91	7.68	2.83	1.76	11.132	0.057	0.382	89.581	1.864	0.019	4.463	0.093
B-14H-3	50	51	132.00	132.01	7.69	2.83	1.75	11.052	0.058	0.442	88.412	1.735	0.022	4.385	0.086
B-14H-3	60	61	132.10	132.11	7.69	2.83	1.77	11.017	0.056	0.358	88.823	2.801	0.018	4.441	0.140
B-14H-3	70	71	132.20	132.21	7.69	2.33	1.81	11.042	0.058	0.363	88.985	2.617	0.015	3.743	0.110
B-14H-3	80	81	132.30	132.31	7.70	2.07	1.80	11.090	0.061	0.363	89.388	2.320	0.014	3.336	0.087
B-14H-3	90	91	132.40	132.41	7.70	2.07	1.80	11.217	0.056	0.333	90.705	3.130	0.012	3.387	0.117
B-14H-3	100	101	132.50	132.51	7.71	2.07	1.80	11.280	0.055	0.322	91.316	2.287	0.012	3.411	0.085
B-14H-3	110	111	132.60	132.61	7.71	2.07	1.85	11.323	0.049	0.319	91.700	2.117	0.012	3.508	0.081
B-14H-3	120	121	132.70	132.71	7.72	2.07	1.82	11.299	0.055	0.276	91.862	2.043	0.010	3.467	0.077
B-14H-3	130	131	132.80	132.81	7.72	2.07	1.84	11.483	0.052	0.273	93.408	2.295	0.010	3.562	0.088
B-14H-3	140	141	132.90	132.91	7.73	2.07	1.85	11.480	0.061	0.243	93.634	1.852	0.009	3.584	0.071
B-14H-4	0	1	132.98	132.99	7.73	2.07	1.84	11.453	0.055	0.265	93.229	2.089	0.010	3.558	0.080
B-14H-4	10	11	133.08	133.09	7.74	2.07	1.83	11.567	0.060	0.251	94.297	1.179	0.010	3.576	0.045
B-14H-4	20	21	133.18	133.19	7.74	2.07	1.80	11.502	0.060	0.234	93.898	1.622	0.009	3.508	0.061
B-14H-4	30	31	133.28	133.29	7.75	2.07	1.79	11.501	0.059	0.249	93.765	2.032	0.009	3.474	0.075

doi:10.6342/NTU202301546

Hole, core, section	Top offset (cm)	Bottom offset (cm)	Top depth CCSF-A (m)	Bottom depth CCSF-A (m)	Age (Ma)	LSR (cm/kyr)	Bulk density (g/cm^3)	TC (%)	error (%)	TOC (%)	$CaCO_3$ (%)	opal (%)	TOC MAR (g cm^{-2} kyr^{-1})	$CaCO_3$ MAR (g cm^{-2} kyr^{-1})	opal MAR (g cm^{-2} kyr^{-1})
B-14H-4	40	41	133.38	133.39	7.75	2.07	1.80	11.453	0.054	0.249	93.368	2.202	0.009	3.485	0.082
B-14H-4	50	51	133.48	133.49	7.75	2.07	1.79	11.300	0.051	0.308	91.599	2.299	0.011	3.395	0.085
B-14H-4	60	61	133.58	133.59	7.76	2.07	1.80	11.261	0.057	0.303	91.318	1.948	0.011	3.393	0.072
B-14H-4	70	71	133.68	133.69	7.76	2.07	1.77	11.134	0.057	0.305	90.243	3.312	0.011	3.309	0.121
B-14H-4	80	81	133.78	133.79	7.77	2.07	1.75	11.081	0.055	0.329	89.600	2.486	0.012	3.241	0.090
B-14H-4	90	91	133.88	133.89	7.77	2.07	1.74	10.990	0.053	0.333	88.806	1.795	0.012	3.192	0.065
B-14H-4	100	101	133.98	133.99	7.78	2.07	1.75	11.086	0.055	0.320	89.710	2.398	0.012	3.242	0.087
B-14H-4	110	111	134.08	134.09	7.78	2.07	1.75	11.229	0.062	0.292	91.139	2.118	0.011	3.303	0.077
B-14H-4	120	121	134.18	134.19	7.79	2.07	1.71	10.731	0.059	0.383	86.231	2.301	0.014	3.058	0.082
B-14H-4	130	131	134.28	134.29	7.79	2.07	1.70	10.222	0.057	0.483	81.162	3.142	0.017	2.852	0.110
B-14H-4	140	141	134.38	134.39	7.80	2.07	1.71	10.289	0.059	0.459	81.913	3.674	0.016	2.893	0.130
B-14H-5	0	1	134.46	134.47	7.80	2.07	1.72	10.527	0.058	0.543	83.192	2.823	0.019	2.960	0.100
B-14H-5	10	11	134.56	134.57	7.81	2.07	1.69	10.315	0.055	0.550	81.380	2.962	0.019	2.845	0.104
B-14H-5	20	21	134.66	134.67	7.81	2.07	1.68	10.262	0.059	0.521	81.172	3.082	0.018	2.825	0.107
B-14H-5	30	31	134.76	134.77	7.82	2.07	1.68	10.183	0.052	0.485	80.818	2.631	0.017	2.809	0.091
B-14H-5	40	41	134.86	134.87	7.82	2.07	1.68	10.091	0.059	0.487	80.029	3.318	0.017	2.778	0.115
B-14H-5	50	51	134.96	134.97	7.83	2.07	1.68	10.324	0.057	0.439	82.375	2.464	0.015	2.866	0.086
B-14H-5	60	61	135.06	135.07	7.83	2.07	1.66	10.205	0.058	0.427	81.485	4.161	0.015	2.795	0.143
B-14H-5	70	71	135.16	135.17	7.84	2.07	1.69	10.390	0.054	0.435	82.949	4.955	0.015	2.899	0.173
B-14H-5	80	81	135.26	135.27	7.84	2.07	1.70	10.516	0.058	0.399	84.307	2.763	0.014	2.962	0.097

doi:10.6342/NTU202301546

Hole, core, section	Top offset (cm)	Bottom offset (cm)	Top depth CCSF-A (m)	Bottom depth CCSF-A (m)	Age (Ma)	LSR (cm/kyr)	Bulk density (g/cm^3)	TC (%)	error (%)	TOC (%)	$CaCO_3$ (%)	opal (%)	TOC MAR ($g\ cm^{-2}\ kyr^{-1}$)	$CaCO_3$ MAR ($g\ cm^{-2}\ kyr^{-1}$)	opal MAR ($g\ cm^{-2}\ kyr^{-1}$)
B-14H-5	90	91	135.36	135.37	7.85	2.07	1.69	10.484	0.055	0.466	83.478	3.196	0.016	2.929	0.112
B-14H-5	100	101	135.46	135.47	7.85	2.07	1.70	10.347	0.050	0.459	82.403	4.052	0.016	2.903	0.143
B-14H-5	110	111	135.56	135.57	7.86	2.07	1.64	9.822	0.054	0.539	77.360	4.392	0.018	2.625	0.149
B-14H-5	120	121	135.66	135.67	7.86	2.07	1.66	9.879	0.058	0.415	78.865	5.153	0.014	2.715	0.177
B-14H-5	130	131	135.76	135.77	7.86	2.07	1.69	10.552	0.053	0.350	85.020	3.285	0.012	2.977	0.115
B-14H-5	140	141	135.86	135.87	7.87	2.07	1.63	10.172	0.056	0.355	81.801	4.776	0.012	2.759	0.161
B-14H-6	0	1	135.96	135.97	7.87	2.07	1.55	10.425	0.059	0.370	83.786	4.302	0.012	2.686	0.138
B-14H-6	10	11	136.06	136.07	7.88	2.07	1.64	10.237	0.055	0.387	82.085	3.901	0.013	2.794	0.133
B-14H-6	20	21	136.16	136.17	7.88	2.07	1.62	9.756	0.057	0.506	77.080	4.181	0.017	2.590	0.140
B-14H-6	30	31	136.26	136.27	7.89	2.07	1.59	9.736	0.056	0.563	76.440	5.697	0.019	2.522	0.188
B-14H-6	40	41	136.36	136.37	7.89	2.07	1.61	9.475	0.056	0.500	74.795	6.150	0.017	2.490	0.205
B-14H-6	50	51	136.46	136.47	7.90	2.07	1.64	9.839	0.058	0.526	77.607	5.054	0.018	2.636	0.172
B-14H-6	60	61	136.56	136.57	7.90	2.07	1.61	9.761	0.056	0.452	77.568	3.788	0.015	2.589	0.126
B-14H-6	70	71	136.66	136.67	7.91	2.07	1.61	9.557	0.054	0.451	75.881	4.274	0.015	2.524	0.142
B-14H-6	80	81	136.76	136.77	7.91	2.07	1.67	9.802	0.054	0.382	78.505	5.930	0.013	2.709	0.205
B-14H-6	90	91	136.86	136.87	7.92	2.07	1.67	10.006	0.052	0.339	80.554	6.676	0.012	2.779	0.230
B-14H-6	100	101	136.96	136.97	7.92	2.07	1.70	10.345	0.057	0.314	83.588	4.982	0.011	2.945	0.176
B-14H-6	110	111	137.06	137.07	7.93	2.07	1.70	10.419	0.055	0.518	82.508	3.121	0.018	2.899	0.110
B-14H-6	120	121	137.16	137.17	7.93	2.07	1.66	10.247	0.056	0.573	80.612	3.057	0.020	2.774	0.105
B-15H-1	0	1	138.55	138.56	8.00	2.07	1.63	11.095	0.054	0.467	88.563	1.868	0.016	2.994	0.063

Hole, core, section	Top offset (cm)	Bottom offset (cm)	Top depth CCSF-A (m)	Bottom depth CCSF-A (m)	Age (Ma)	LSR (cm/kyr)	Bulk density (g/cm^3)	TC (%)	error (%)	TOC (%)	$CaCO_3$ (%)	opal (%)	TOC MAR (g cm^{-2} kyr^{-1})	$CaCO_3$ MAR (g cm^{-2} kyr^{-1})	opal MAR (g cm^{-2} kyr^{-1})
B-15H-1	10	11	138.65	138.66	8.00	2.07	1.67	11.254	0.059	0.348	90.887	0.921	0.012	3.148	0.032
B-15H-1	20	21	138.75	138.76	8.01	2.07	1.64	11.273	0.057	0.377	90.803	1.309	0.013	3.087	0.044
B-15H-1	30	31	138.85	138.86	8.01	2.07	1.65	11.590	0.058	0.287	94.185	0.945	0.010	3.221	0.032
B-15H-1	40	41	138.95	138.96	8.02	2.07	1.68	11.747	0.060	0.233	95.949	1.049	0.008	3.333	0.036
B-15H-1	50	51	139.05	139.06	8.02	2.07	1.69	11.702	0.063	0.261	95.338	1.316	0.009	3.333	0.046
B-15H-1	60	61	139.15	139.16	8.03	2.07	1.65	11.455	0.058	0.311	92.869	1.013	0.011	3.175	0.035
B-15H-1	70	71	139.25	139.26	8.03	2.07	1.62	11.092	0.055	0.425	88.887	1.216	0.014	2.983	0.041
B-15H-1	80	81	139.35	139.36	8.04	2.07	1.63	11.155	0.059	0.410	89.541	0.746	0.014	3.024	0.025
B-15H-1	90	91	139.45	139.46	8.04	2.07	1.68	11.420	0.062	0.364	92.133	0.715	0.013	3.202	0.025
B-15H-1	100	101	139.55	139.56	8.05	2.07	1.67	11.459	0.062	0.338	92.671	1.494	0.012	3.200	0.052
B-15H-1	110	111	139.65	139.66	8.05	2.07	1.66	11.385	0.057	0.383	91.677	1.386	0.013	3.146	0.048
B-15H-1	120	121	139.75	139.76	8.06	2.07	1.66	11.157	0.057	0.482	88.961	0.101	0.017	3.056	0.003
B-15H-1	130	131	139.85	139.86	8.06	2.07	1.60	10.131	0.059	0.820	77.591	0.698	0.027	2.568	0.023
B-15H-1	140	141	139.95	139.96	8.07	2.07	1.65	11.018	0.055	0.470	87.897	0.706	0.016	3.000	0.024
B-15H-2	0	1	140.05	140.06	8.07	2.07	1.64	10.629	0.057	0.580	83.740	1.730	0.020	2.842	0.059
B-15H-2	10	11	140.15	140.16	8.08	2.07	1.60	10.339	0.054	0.694	80.375	0.793	0.023	2.664	0.026
B-15H-2	20	21	140.25	140.26	8.08	2.07	1.63	10.354	0.053	0.644	80.918	1.832	0.022	2.737	0.062
B-15H-2	30	31	140.35	140.36	8.09	2.07	1.62	10.795	0.058	0.536	85.486	0.933	0.018	2.865	0.031
B-15H-2	40	41	140.45	140.46	8.09	2.07	1.63	10.799	0.056	0.514	85.702	1.084	0.017	2.888	0.037
B-15H-2	50	51	140.55	140.56	8.10	2.07	1.61	10.974	0.057	0.495	87.320	0.521	0.016	2.904	0.017

Hole, core, section	Top offset (cm)	Bottom offset (cm)	Top depth CCSF-A (m)	Bottom depth CCSF-A (m)	Age (Ma)	LSR (cm/kyr)	Bulk density (g/cm^3)	TC (%)	error (%)	TOC (%)	$CaCO_3$ (%)	opal (%)	TOC MAR (g cm^{-2} kyr^{-1})	$CaCO_3$ MAR (g cm^{-2} kyr^{-1})	opal MAR (g cm^{-2} kyr^{-1})
B-15H-2	60	61	140.65	140.66	8.10	2.07	1.62	10.891	0.060	0.515	86.467	0.394	0.017	2.895	0.013
B-15H-2	70	71	140.75	140.76	8.11	2.06	1.62	10.943	0.060	0.491	87.100	0.546	0.016	2.916	0.018
B-15H-2	80	81	140.85	140.86	8.11	2.05	1.63	10.978	0.054	0.452	87.720	0.765	0.015	2.942	0.026
B-15H-2	90	91	140.95	140.96	8.12	2.05	1.63	10.877	0.061	0.464	86.773	0.557	0.016	2.904	0.019
B-15H-2	100	101	141.05	141.06	8.12	2.05	1.54	10.809	0.055	0.503	85.886	0.771	0.016	2.716	0.024
B-15H-2	110	111	141.15	141.16	8.13	2.05	1.61	10.539	0.059	0.569	83.078	0.267	0.019	2.745	0.009
B-15H-2	120	121	141.25	141.26	8.13	2.05	1.62	10.797	0.055	0.492	85.878	1.569	0.016	2.853	0.052
B-15H-2	130	131	141.35	141.36	8.14	2.05	1.63	11.068	0.055	0.477	88.251	0.916	0.016	2.963	0.031
B-15H-2	140	141	141.45	141.46	8.14	2.05	1.64	10.979	0.061	0.442	87.805	0.528	0.015	2.954	0.018
B-15H-3	0	1	141.55	141.56	8.14	2.05	1.63	10.805	0.055	0.498	85.890	0.434	0.017	2.883	0.015
B-15H-3	10	11	141.65	141.66	8.15	2.05	1.63	10.568	0.057	0.556	83.429	0.946	0.019	2.799	0.032
B-15H-3	20	21	141.75	141.76	8.15	2.05	1.64	10.740	0.056	0.571	84.740	0.317	0.019	2.858	0.011
B-15H-3	30	31	141.85	141.86	8.16	2.05	1.68	10.482	0.059	0.595	82.390	0.320	0.021	2.839	0.011
B-15H-3	40	41	141.95	141.96	8.16	2.05	1.68	10.495	0.054	0.583	82.602	0.282	0.020	2.843	0.010
B-15H-3	50	51	142.05	142.06	8.17	2.05	1.69	10.950	0.059	0.456	87.444	0.366	0.016	3.039	0.013
B-15H-3	60	61	142.15	142.16	8.17	2.05	1.69	11.291	0.054	0.387	90.869	0.302	0.013	3.164	0.011
B-15H-3	70	71	142.25	142.26	8.18	2.05	1.68	11.347	0.060	0.363	91.535	0.202	0.013	3.164	0.007
B-15H-3	80	81	142.35	142.36	8.18	2.05	1.67	11.168	0.054	0.402	89.719	1.194	0.014	3.078	0.041
B-15H-3	90	91	142.45	142.46	8.19	2.05	1.68	11.129	0.058	0.421	89.237	1.106	0.014	3.072	0.038
B-15H-3	100	101	142.55	142.56	8.19	2.05	1.69	10.860	0.059	0.460	86.665	0.152	0.016	3.003	0.005

doi:10.6342/NTU202301546

Hole, core, section	Top offset (cm)	Bottom offset (cm)	Top depth CCSF-A (m)	Bottom depth CCSF-A (m)	Age (Ma)	LSR (cm/kyr)	Bulk density (g/cm^3)	TC (%)	error (%)	TOC (%)	$CaCO_3$ (%)	opal (%)	TOC MAR (g cm^{-2} kyr^{-1})	$CaCO_3$ MAR (g cm^{-2} kyr^{-1})	opal MAR (g cm^{-2} kyr^{-1})
B-15H-3	110	111	142.65	142.66	8.20	2.05	1.69	10.767	0.058	0.505	85.517	0.861	0.018	2.971	0.030
B-15H-3	120	121	142.75	142.76	8.20	2.05	1.70	10.614	0.056	0.576	83.645	1.084	0.020	2.926	0.038
B-15H-3	130	131	142.85	142.86	8.21	2.05	1.69	10.652	0.057	0.555	84.141	1.162	0.019	2.927	0.040
B-15H-3	140	141	142.95	142.96	8.21	2.05	1.71	11.196	0.060	0.410	89.879	0.289	0.014	3.166	0.010
B-15H-4	0	1	143.05	143.06	8.22	2.05	1.72	11.131	0.055	0.136	91.624	0.633	0.005	3.235	0.022
B-15H-4	10	11	143.15	143.16	8.22	2.05	1.74	11.563	0.059	0.315	93.734	0.676	0.011	3.346	0.024
B-15H-4	20	21	143.25	143.26	8.23	2.05	1.74	11.612	0.057	0.267	94.536	0.683	0.010	3.389	0.024
B-15H-4	30	31	143.35	143.36	8.23	2.05	1.75	11.592	0.061	0.281	94.257	0.538	0.010	3.398	0.019
B-15H-4	40	41	143.45	143.46	8.24	2.05	1.73	11.458	0.059	0.332	92.716	0.392	0.012	3.300	0.014
B-15H-4	50	51	143.55	143.56	8.24	2.05	1.67	10.147	0.053	0.665	79.017	0.980	0.023	2.707	0.034
B-15H-4	60	61	143.65	143.66	8.25	2.05	1.68	9.501	0.056	0.811	72.420	0.560	0.028	2.501	0.019
B-15H-4	70	71	143.75	143.76	8.25	2.05	1.70	9.024	0.048	0.882	67.848	0.640	0.031	2.370	0.022
B-15H-4	80	81	143.85	143.86	8.26	2.05	1.71	10.627	0.051	0.547	83.994	0.039	0.019	2.944	0.001
B-15H-4	90	91	143.95	143.96	8.26	2.05	1.68	10.540	0.054	0.621	82.650	0.294	0.021	2.859	0.010
B-15H-4	100	101	144.05	144.06	8.27	2.05	1.70	10.214	0.054	0.728	79.050	0.686	0.025	2.763	0.024
B-15H-4	110	111	144.15	144.16	8.27	2.05	1.73	10.429	0.059	0.597	81.926	1.040	0.021	2.919	0.037
B-15H-4	120	121	144.25	144.26	8.28	2.05	1.72	10.442	0.053	0.492	82.909	0.765	0.017	2.929	0.027
B-15H-4	130	131	144.35	144.36	8.28	2.05	1.72	10.680	0.056	0.483	84.974	0.839	0.017	2.997	0.030
B-15H-4	140	141	144.45	144.46	8.29	2.05	1.71	10.801	0.060	0.436	86.369	0.045	0.015	3.035	0.002
B-15H-5	0	1	144.55	144.56	8.29	2.05	1.49	10.495	0.053	0.505	83.251	0.278	0.015	2.543	0.009

Hole, core, section	Top offset (cm)	Bottom offset (cm)	Top depth CCSF-A (m)	Bottom depth CCSF-A (m)	Age (Ma)	LSR (cm/kyr)	Bulk density (g/cm^3)	TC (%)	error (%)	TOC (%)	$CaCO_3$ (%)	opal (%)	TOC MAR ($g\ cm^{-2}\ kyr^{-1}$)	$CaCO_3$ MAR ($g\ cm^{-2}\ kyr^{-1}$)	opal MAR ($g\ cm^{-2}\ kyr^{-1}$)
B-15H-5	10	11	144.65	144.66	8.30	2.05	1.70	10.184	0.055	0.488	80.795	0.424	0.017	2.816	0.015
B-15H-5	20	21	144.75	144.76	8.30	2.05	1.70	10.434	0.058	0.496	82.815	0.199	0.017	2.901	0.007
B-15H-5	30	31	144.85	144.86	8.31	2.05	1.69	10.695	0.055	0.467	85.231	0.080	0.016	2.956	0.003
B-15H-5	40	41	144.95	144.96	8.31	2.05	1.73	10.540	0.056	0.425	84.292	0.759	0.015	2.998	0.027
B-15H-5	50	51	145.05	145.06	8.32	2.05	1.74	8.931	0.051	0.511	70.165	3.080	0.018	2.504	0.110
B-15H-5	60	61	145.15	145.16	8.32	2.05	1.65	10.829	0.059	0.457	86.429	0.231	0.015	2.928	0.008
B-15H-5	70	71	145.25	145.26	8.33	2.05	1.56	10.792	0.056	0.424	86.393	0.121	0.014	2.777	0.004
B-15H-5	80	81	145.35	145.36	8.33	2.05	1.62	10.840	0.056	0.427	86.776	0.503	0.014	2.897	0.017
B-15H-5	90	91	145.45	145.46	8.33	2.05	1.64	10.825	0.059	0.450	86.453	0.408	0.015	2.908	0.014
B-15H-5	100	101	145.55	145.56	8.34	2.05	1.59	10.853	0.052	0.429	86.865	0.414	0.014	2.836	0.014
B-15H-5	110	111	145.65	145.66	8.34	2.05	1.59	10.913	0.055	0.427	87.382	0.321	0.014	2.858	0.010
B-15H-5	120	121	145.75	145.76	8.35	2.05	1.58	10.799	0.056	0.431	86.393	0.239	0.014	2.810	0.008
B-15H-5	130	131	145.85	145.86	8.35	1.75	1.37	10.743	0.058	0.421	86.020	0.576	0.010	2.055	0.014

doi:10.6342/NTU202301546

Table 11. Site U1543 data.

Hole, core, section	Top offset (cm)	Bottom offset (cm)	Top depth CCSF-A (m)	Bottom depth CCSF-A (m)	Age (Ma)	LSR (cm/kyr)	Bulk density (g/cm^3)	TC (%)	error (%)	TOC (%)	$CaCO_3$ (%)	opal (%)	TOC MAR (g cm^{-2} kyr^{-1})	$CaCO_3$ MAR (g cm^{-2} kyr^{-1})	opal MAR (g cm^{-2} kyr^{-1})
B-30H-3	50	54	278.15	278.19	5.19	3.33	1.62	0.293	0.042	0.273	0.165	8.008	0.015	0.009	0.432
B-30H-3	125	129	278.90	278.94	5.21	3.33	1.56	0.404	0.042	0.387	0.145	12.664	0.020	0.008	0.656
B-30H-4	57	61	279.65	279.69	5.23	4.02	1.58	0.307	0.042	0.290	0.143	10.112	0.019	0.009	0.645
B-30H-4	132	136	280.40	280.44	5.25	4.21	1.48	0.260	0.042	0.243	0.142	15.985	0.015	0.009	0.996
B-30H-5	64	68	281.15	281.19	5.27	4.21	1.58	0.303	0.043	0.284	0.162	12.691	0.019	0.011	0.842
B-30H-5	139	143	281.90	281.94	5.29	4.21	1.46	0.211	0.038	0.194	0.138	17.448	0.012	0.008	1.073
B-30H-6	71	75	282.65	282.69	5.30	4.21	1.52	0.230	0.043	0.214	0.137	12.978	0.014	0.009	0.830
B-30H-7	4	8	283.40	283.44	5.32	4.21	1.57	0.211	0.042	0.193	0.154	8.210	0.013	0.010	0.542
A-28H-4	65	69	284.15	284.19	5.34	4.21	1.50	0.242	0.041	0.226	0.135	10.437	0.014	0.008	0.657
A-28H-4	140	144	284.90	284.94	5.36	4.21	1.64	0.186	0.038	0.166	0.164	6.333	0.012	0.011	0.438
A-28H-5	67	71	285.65	285.69	5.37	4.21	1.62	0.266	0.039	0.248	0.147	8.292	0.017	0.010	0.565
A-28H-5	140	144	286.40	286.44	5.39	4.21	1.38	0.162	0.041	0.143	0.160	13.116	0.008	0.009	0.763
A-28H-6	67	71	287.15	287.19	5.41	4.21	1.57	0.188	0.041	0.166	0.177	9.220	0.011	0.012	0.611
A-28H-6	142	146	287.90	287.94	5.43	4.21	1.46	0.237	0.039	0.223	0.111	18.437	0.014	0.007	1.137
B-31H-3	104	108	288.65	288.69	5.45	4.21	1.47	0.206	0.040	0.190	0.133	14.283	0.012	0.008	0.882
B-31H-4	38	42	289.40	289.44	5.46	4.21	1.46	0.214	0.040	0.199	0.126	21.334	0.012	0.008	1.311
B-31H-4	113	117	290.15	290.19	5.48	4.21	1.45	0.289	0.040	0.277	0.103	23.809	0.017	0.006	1.453
B-31H-5	46	50	290.90	290.94	5.50	4.21	1.48	0.375	0.041	0.365	0.079	22.407	0.023	0.005	1.400
A-29H-1	67	71	292.40	292.44	5.53	4.21	1.68	0.202	0.039	0.185	0.143	3.373	0.013	0.010	0.239

doi:10.6342/NTU202301546

Hole, core, section	Top offset (cm)	Bottom offset (cm)	Top depth CCSF-A (m)	Bottom depth CCSF-A (m)	Age (Ma)	LSR (cm/kyr)	Bulk density (g/cm^3)	TC (%)	error (%)	TOC (%)	$CaCO_3$ (%)	opal (%)	TOC MAR ($g\ cm^{-2}\ kyr^{-1}$)	$CaCO_3$ MAR ($g\ cm^{-2}\ kyr^{-1}$)	opal MAR ($g\ cm^{-2}\ kyr^{-1}$)
A-29H-1	142	146	293.15	293.19	5.55	4.21	1.62	0.160	0.042	0.141	0.164	5.668	0.010	0.011	0.387
A-29H-2	67	71	293.90	293.94	5.57	4.21	1.68	0.265	0.035	0.246	0.158	6.434	0.017	0.011	0.455
A-29H-2	142	146	294.65	294.69	5.59	4.21	1.66	0.290	0.040	0.270	0.164	8.494	0.019	0.012	0.594
A-29H-3	67	71	295.40	295.44	5.61	4.21	1.65	0.308	0.042	0.288	0.165	8.424	0.020	0.011	0.585
A-29H-3	142	146	296.15	296.19	5.62	4.21	1.70	0.261	0.040	0.242	0.159	8.003	0.017	0.011	0.573
A-29H-4	67	71	296.90	296.94	5.64	4.21	1.62	0.211	0.035	0.194	0.145	9.164	0.013	0.010	0.626
A-29H-4	142	146	297.65	297.69	5.66	4.21	1.65	0.251	0.040	0.232	0.158	7.188	0.016	0.011	0.498
A-29H-5	68	72	298.40	298.44	5.68	4.21	1.65	0.212	0.038	0.195	0.139	9.293	0.014	0.010	0.646
B-32H-1	124	128	299.14	299.18	5.69	4.21	1.60	0.249	0.038	0.233	0.132	10.103	0.016	0.009	0.681
B-32H-2	58	62	299.89	299.93	5.71	4.21	1.58	0.242	0.038	0.224	0.154	6.884	0.015	0.010	0.459
B-32H-2	133	137	300.64	300.68	5.73	4.21	1.38	0.229	0.041	0.214	0.126	14.157	0.012	0.007	0.821
B-32H-3	66	70	301.39	301.43	5.75	4.21	1.73	0.228	0.042	0.207	0.171	7.294	0.015	0.012	0.530
B-32H-4	73	77	302.89	302.93	5.78	4.21	1.64	0.199	0.040	0.183	0.140	7.090	0.013	0.010	0.488
B-32H-5	6	10	303.64	303.68	5.80	4.21	1.81	0.306	0.041	0.285	0.178	4.562	0.022	0.014	0.349
B-32H-5	81	85	304.39	304.43	5.82	4.21	1.61	0.249	0.040	0.228	0.175	4.613	0.015	0.012	0.313
B-32H-6	14	18	305.14	305.18	5.84	4.21	1.59	0.239	0.037	0.217	0.181	5.068	0.015	0.012	0.339
B-32H-6	89	93	305.89	305.93	5.86	4.21	1.68	0.238	0.036	0.221	0.146	5.935	0.016	0.010	0.420
B-32H-7	22	26	306.64	306.68	5.87	4.21	1.59	0.176	0.042	0.158	0.146	5.500	0.011	0.010	0.369
B-32H-7	97	101	307.39	307.43	5.89	4.21	1.67	0.198	0.042	0.176	0.179	4.272	0.012	0.013	0.300
[illegible]-30H-5	29	33	308.15	308.19	5.91	4.21	1.53	0.225	0.042	0.206	0.153	7.419	0.013	0.010	0.479

Hole, core, section	Top offset (cm)	Bottom offset (cm)	Top depth CCSF-A (m)	Bottom depth CCSF-A (m)	Age (Ma)	LSR (cm/kyr)	Bulk density (g/cm^3)	TC (%)	error (%)	TOC (%)	$CaCO_3$ (%)	opal (%)	TOC MAR ($g\ cm^{-2}\ kyr^{-1}$)	$CaCO_3$ MAR ($g\ cm^{-2}\ kyr^{-1}$)	opal MAR ($g\ cm^{-2}\ kyr^{-1}$)
A-30H-5	104	108	308.90	308.94	5.93	4.21	1.65	0.234	0.039	0.213	0.175	5.768	0.015	0.012	0.401
A-30H-6	26	28	309.65	309.69	5.94	4.21	1.68	0.256	0.033	0.239	0.143	4.498	0.017	0.010	0.318
B-33H-1	98	102	310.40	310.44	5.96	4.21	1.58	0.351	0.043	0.337	0.122	6.840	0.022	0.008	0.455
B-33H-2	26	30	311.15	311.19	5.98	4.21	1.65	0.264	0.041	0.246	0.143	5.787	0.017	0.010	0.401
B-33H-2	101	105	311.90	311.94	6.00	4.21	1.68	0.267	0.042	0.251	0.134	6.153	0.018	0.009	0.435
B-33H-3	29	33	312.65	312.69	6.02	4.22	1.55	0.219	0.040	0.203	0.136	6.285	0.013	0.009	0.411
B-33H-3	104	108	313.40	313.44	6.03	4.66	1.69	0.550	0.043	0.538	0.099	5.380	0.042	0.008	0.424
B-33H-4	32	36	314.15	314.19	6.05	4.66	1.60	0.274	0.041	0.255	0.161	8.335	0.019	0.012	0.623
B-33H-4	107	111	314.90	314.94	6.07	4.66	1.66	0.270	0.038	0.254	0.129	7.393	0.020	0.010	0.571
B-33H-5	35	39	315.65	315.69	6.08	4.66	1.73	0.295	0.042	0.278	0.146	5.697	0.022	0.012	0.461
B-33H-5	110	114	316.40	316.44	6.10	4.66	1.76	0.281	0.039	0.262	0.159	4.995	0.022	0.013	0.410
B-33H-6	38	42	317.15	317.19	6.11	4.66	1.61	0.220	0.041	0.201	0.153	6.675	0.015	0.011	0.501
A-31H-2	108	110	317.89	317.93	6.13	4.66	1.71	0.294	0.041	0.273	0.170	3.912	0.022	0.014	0.312
A-31H-3	32	34	318.64	318.68	6.15	4.66	1.55	0.270	0.041	0.253	0.144	8.153	0.018	0.010	0.588
A-31H-3	107	109	319.39	319.43	6.16	4.66	1.66	0.250	0.042	0.232	0.148	3.823	0.018	0.011	0.295
A-31H-4	31	33	320.14	320.18	6.18	4.66	1.55	0.162	0.042	0.142	0.167	6.415	0.010	0.012	0.464
A-31H-4	106	108	320.89	320.93	6.19	4.66	1.61	0.395	0.036	0.380	0.119	5.600	0.029	0.009	0.420
A-31H-5	30	32	321.64	321.68	6.21	4.66	1.71	0.204	0.038	0.184	0.163	4.090	0.015	0.013	0.327
A-31H-5	105	107	322.39	322.43	6.23	4.66	1.63	0.354	0.039	0.338	0.135	6.077	0.026	0.010	0.461
A-31H-6	30	32	323.14	323.18	6.24	3.10	1.56	0.151	0.040	0.133	0.149	6.572	0.006	0.007	0.318

Hole, core, section	Top offset (cm)	Bottom offset (cm)	Top depth CCSF-A (m)	Bottom depth CCSF-A (m)	Age (Ma)	LSR (cm/kyr)	Bulk density (g/cm^3)	TC (%)	error (%)	TOC (%)	$CaCO_3$ (%)	opal (%)	TOC MAR (g cm^{-2} kyr^{-1})	$CaCO_3$ MAR (g cm^{-2} kyr^{-1})	opal MAR (g cm^{-2} kyr^{-1})
A-31H-6	105	107	323.89	323.93	6.27	2.08	1.47	0.187	0.040	0.171	0.131	8.961	0.005	0.004	0.275
A-31H-7	29	31	324.64	324.68	6.30	5.15	1.48	0.194	0.043	0.179	0.123	8.356	0.014	0.009	0.636
A-32H-1	70	72	325.87	325.91	6.36	2.08	1.57	0.178	0.042	0.161	0.145	11.667	0.005	0.005	0.382
A-32H-1	145	147	326.62	326.66	6.40	2.08	1.61	0.185	0.040	0.167	0.152	11.137	0.006	0.005	0.373
A-32H-2	69	71	327.37	327.41	6.43	2.34	1.55	0.169	0.042	0.153	0.133	15.424	0.006	0.005	0.561
A-32H-2	144	145	328.12	328.16	6.47	2.37	1.60	0.130	0.041	0.115	0.125	11.823	0.004	0.005	0.447
A-32H-3	68	71	328.87	328.91	6.50	2.37	1.65	0.229	0.043	0.208	0.179	10.260	0.008	0.007	0.400
A-32H-3	143	145	329.62	329.66	6.53	2.37	1.63	0.237	0.041	0.217	0.163	10.892	0.008	0.006	0.420
A-32H-4	57	60	330.37	330.41	6.56	2.37	1.67	0.175	0.043	0.158	0.139	9.832	0.006	0.005	0.388
A-32H-4	142	144	331.12	331.16	6.59	2.37	1.67	0.198	0.041	0.181	0.144	9.267	0.007	0.006	0.367
A-32H-5	66	68	331.87	331.91	6.62	2.37	1.57	0.138	0.041	0.123	0.123	12.563	0.005	0.005	0.468
A-32H-5	141	143	332.62	332.66	6.66	2.37	1.63	0.130	0.039	0.112	0.149	8.767	0.004	0.006	0.338
A-32H-6	64	68	333.37	333.41	6.69	2.37	1.63	0.132	0.042	0.114	0.154	9.170	0.004	0.006	0.354
A-32H-6	139	143	334.12	334.16	6.72	2.70	1.63	0.123	0.037	0.101	0.187	8.284	0.004	0.008	0.365
A-33H-1	69	73	336.37	336.41	6.80	2.77	1.56	0.125	0.037	0.108	0.142	11.961	0.005	0.006	0.516
A-33H-1	144	148	337.12	337.16	6.83	2.77	1.58	0.129	0.039	0.111	0.148	10.344	0.005	0.007	0.454
A-33H-2	64	68	337.87	337.91	6.86	2.77	1.62	0.116	0.037	0.101	0.129	8.763	0.005	0.006	0.393
A-33H-2	140	144	338.62	338.66	6.88	2.77	1.67	0.120	0.039	0.103	0.139	10.319	0.005	0.006	0.478
A-33H-3	63	65	339.37	339.41	6.91	2.77	1.62	0.189	0.039	0.172	0.138	8.194	0.008	0.006	0.366
A-33H-3	140	142	340.12	340.16	6.94	2.77	1.65	0.177	0.040	0.159	0.155	8.505	0.007	0.007	0.387

doi:10.6342/NTU202301546

Hole, core, section	Top offset (cm)	Bottom offset (cm)	Top depth CCSF-A (m)	Bottom depth CCSF-A (m)	Age (Ma)	LSR (cm/kyr)	Bulk density (g/cm^3)	TC (%)	error (%)	TOC (%)	$CaCO_3$ (%)	opal (%)	TOC MAR (g cm^{-2} kyr^{-1})	$CaCO_3$ MAR (g cm^{-2} kyr^{-1})	opal MAR (g cm^{-2} kyr^{-1})
A-33H-4	65	67	340.87	340.91	6.96	2.77	1.58	0.193	0.040	0.176	0.143	11.087	0.008	0.006	0.486
A-33H-4	140	142	341.62	341.66	6.99	2.77	1.61	0.119	0.041	0.097	0.184	10.354	0.004	0.008	0.460
A-33H-5	62	66	342.37	342.41	7.02	2.77	1.57	0.128	0.040	0.111	0.149	13.269	0.005	0.006	0.578
A-33H-5	137	141	343.12	343.16	7.05	2.77	1.35	0.180	0.042	0.164	0.137	13.798	0.006	0.005	0.515
A-33H-6	57	61	343.87	343.91	7.07	2.77	1.38	0.175	0.040	0.159	0.130	14.538	0.006	0.005	0.553
A-33H-6	132	136	344.62	344.66	7.10	2.77	1.52	0.165	0.043	0.150	0.125	15.411	0.006	0.005	0.649
A-33H-7	57	61	345.37	345.41	7.13	4.09	1.50	0.166	0.041	0.153	0.111	12.911	0.009	0.007	0.791
A-34H-1	69	73	346.87	346.91	7.16	4.79	1.45	0.134	0.042	0.121	0.113	17.959	0.008	0.008	1.249
A-34H-1	144	148	347.62	347.66	7.18	4.79	1.43	0.126	0.039	0.113	0.109	25.884	0.008	0.008	1.777
A-34H-2	69	73	348.37	348.41	7.20	4.79	1.45	0.212	0.039	0.200	0.105	22.690	0.014	0.007	1.573
A-34H-2	144	148	349.12	349.16	7.21	3.92	1.46	0.154	0.040	0.140	0.118	22.715	0.008	0.007	1.305
A-34H-3	68	72	349.87	349.91	7.23	3.87	1.45	0.144	0.043	0.128	0.130	23.756	0.007	0.007	1.336
A-34H-3	143	147	350.62	350.66	7.25	4.38	1.47	0.373	0.042	0.357	0.134	21.930	0.023	0.009	1.409
A-34H-4	67	71	351.37	351.41	7.27	4.43	1.46	0.645	0.039	0.627	0.146	28.921	0.041	0.009	1.870
A-34H-4	142	146	352.12	352.16	7.28	4.43	1.48	0.191	0.041	0.176	0.124	18.304	0.012	0.008	1.203
A-34H-5	68	70	352.87	352.91	7.30	4.43	1.43	0.242	0.043	0.228	0.114	28.513	0.014	0.007	1.810
A-34H-5	140	142	353.62	353.66	7.32	4.43	1.44	0.241	0.041	0.226	0.129	28.085	0.014	0.008	1.786
A-34H-6	68	70	354.37	354.41	7.33	4.43	1.48	0.184	0.041	0.168	0.135	20.360	0.011	0.009	1.337

Table 12. Lithology description of site U1541 and U1543 (core used in this study). (Lamy et al., 2021, https://doi.org/10.14379/iodp.proc.383.105.2021)

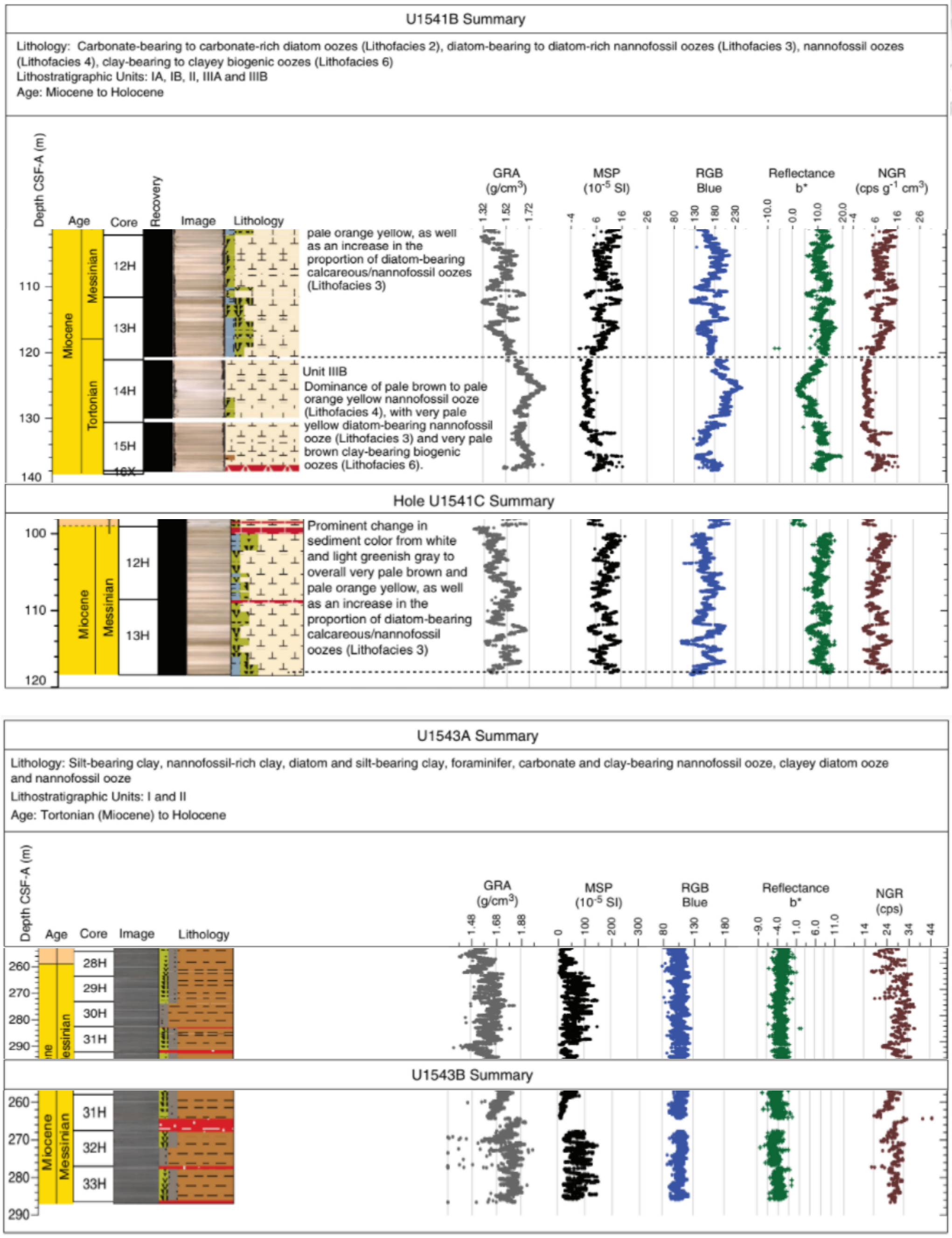

doi:10.6342/NTU202301546